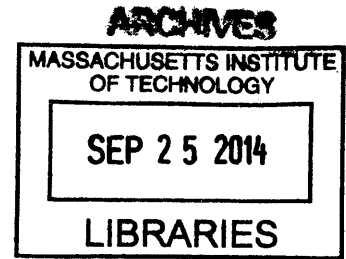# Optical Properties of Two-Dimensional Transition Metal Dichalcogenides

by

Yuxuan Lin

B. A., Microelectronics, 2012
Tsinghua University, Beijing, China

SUBMITTED TO THE DEPARTMENT OF ELECTRICAL ENGINEERING AND
COMPUTER SCUENCE IN PARTIAL FULFILLMENT OF THE REQUIREMENTS
FOR THE DEGREE OF
MASTER OF SCIENCE IN ELECTRICAL ENGINEERING
AT THE
MASSACHUSETTS INSTITUTE OF TECHNOLOGY

SEPTEMBER 2014

Signature redacted

Signature of Author:_____

Department of Electrical Engineering and Computer Science
August 29, 2014

Signature redacted

Certified by: _____

Mildred S. Dresselhaus
Professor of Physics and Electrical Engineering
Thesis Co-Supervisor

Signature redacted

Certified by: _____

Tomás Palacios
Associate Professor of Electrical Engineering
Thesis Co-Supervisor

Signature redacted

Accepted by:_____

Leslie A. Kolodziejski
Professor of Electrical Engineering
Chairman, Department Committee on Graduate Students

Optical Properties of Two-Dimensional Transition Metal Dichalcogenides

By

Yuxuan Lin

Submitted to the Department of Electrical Engineering and Computer Science

on August 29, 2014 in Partial Fulfillment of the Requirements for the Degree of

Master of Science in Electrical Engineering

ABSTRACT

The re-discovery of the atomically thin transition metal dichalcogenides (TMDs), which are mostly semiconductors with a wide range of band gaps, has diversified the family of two-dimensional materials and boosted the research on their potential applications in the fields of logic nanoelectronics and high-performance nanophotonics. Many body effects are of great significance in 2-dimensional TMDs, especially when thinned down to a monolayer. As a result, the exciton-related phenomena are prominent in TMD monolayers, which distinguish the monolayers significantly from their bulk counterparts. This thesis systematically studies the optical properties in semiconducting, monolayer TMDs, including Raman spectroscopy, photoluminescence (PL), and optical absorption. In order to further understand the excitononic properties in 2-dimensional TMDs, we took monolayer MoS_2 as an example, and studied its exciton behaviors with different carrier densities and dielectric environments through PL measurements with the help of electrochemical gating and non-ionic solvent immersion. Our findings are helpful to understand better the tightly bound excitons in low-dimensional systems and to provide a simple approach to controlling the generation of excitons and trions (charged excitons) selectively and separately.

Thesis co-supervisors:

Mildred S. Dresselhaus

Title: Professor of Physics and Electrical Engineering

Tomás Palacios

Title: Associate Professor of Electrical Engineering

3

Table of Contents

List of Figures

List of Tables

Chapter 1. Introduction

1.1 Historical Perspective of 2-Dimensional Material Research

For years, researchers have had disputes about the actual stability and existence in the natural environment of truly two-dimensional (2D) materials [1-4] until the year of 2004, when graphene, a one-atom thick carbon-based material, was obtained by the Scotch-tape method [5-8]. Later reports showed that this simple but fantastic material has various unique physical properties: the linear dispersion relation in graphene that makes the electrons behave like massless Dirac Fermions [7-9]; half-integer and anomalous quantum Hall effect [8-11]; ballistic transport with ultrahigh mobility [6-9,12-19]; broadband high transparency defined by the fine structure constant [8,9,20-22]; superior mechanical strength [23-25]; etc. All these observations have attracted extensive attention throughout the Academia, and great efforts have been made to push graphene into real applications in the fields of radio-frequency integrated circuits [26-39], optical detections and communications [39-49], terahertz plasmonics [40,44,50-56], energy conversion and storage [57-66], nano-electro-mechanical systems (NEMSes) [67-71], advanced chemical and/or biological sensing [72-80], etc.

In spite of the extremely high mobility of graphene [12-19, 26], with negligible high electric-field degradation [26], the lack of an energy band gap makes it difficult to use graphene in logic electronics, especially in low-power applications. To overcome this, both theoretical and experimental studies were made on bilayer graphene [81-84] and graphene nanoribbons [85-87], from which a small band gap can be opened to accomplish an acceptably high on-off current ratio of graphene transistors. Nevertheless, neither method is sufficient to provide high on-off current ratio while retaining the advantage of the ultrahigh mobility. More recently, the family of semiconducting transition metal dichalcogenides (TMDs) was re-visited and found to be stable in monolayer or few-layer forms [88-91]; These monolayer TMD materials are direct band gap semiconductors with the band gap in the near infrared and visible range, and these TMD materials are better candidates in both logic electronic [90-109] and optoelectronic applications [88,89,110-131] than graphene.

During the past decade, especially within the past 3 years, the studies of 2D TMDs have been growing rapidly. After successfully obtaining MoS_2 thin flakes from the Scotch tape method in 2005 [5,6], people started to synthesize large-area continuous TMDs through physical vapor deposition (PVD) [132] and chemical vapor deposition (CVD) [133-142]. The precursors of the CVD synthesis of TMDs are, unlike graphene, in the solid phase with relative narrow windows of sublimation and chemical reactions, which makes the flow field and the temperature field much more difficult to control. In spite of this, several groups have successfully synthesized large-area monolayer MoS_2 and WS_2, with a quality that is even better than the exfoliated flakes [106,107,137].

The unique physical properties of 2D TMDs have also been deeply explored. In 2010, K. F. Mak et al. [88] reported the indirect-to-direct transition of the band gap as MoS_2 evolves from bulk to the monolayer form; and C. Lee et al. [143] reported the anomalous behaviors of the Raman spectroscopy of mono-, bi- and few-layer MoS_2. Various theoretical studies [144-152] showed that many-body effects, including the electron-electron interaction and the electron-hole interaction, are of great importance in 2D TMDs; that is, both the electron self-energies and the exciton binding energies should be considered in describing the electronic band structure of 2D TMDs correctly. The existence of tightly bound excitons [88,89] and multi-excitons [153-157] with relatively large binding energies in 2D TMDs was then discovered, making the optical world of 2D materials closely coupled with the "exciton" concept, which is rarely mentioned in 3D optoelectronics. Later on, Four research groups reported at the same time that the two electron valleys with different spins in TMD materials can be selectively activated by their excitation using the circularly polarized light [158-161]; based on this, they proposed the novel type of electronics – called valleytronics – which can be potentially used in high-performance digital signal processing and even quantum computing. More recently, K. F. Mak et al. observed the valley Hall Effect [162] in monolayer MoS_2, which is the first non-magnetic-field-involved quantum Hall Effect discovered so far.

With such outstanding properties, 2D TMDs have been quite attractive to electrical engineers as well. The first transport measurement on atomic thin TMDs was done by the A. Geim's group in 2005 and published in PNAS [5], in which MoS_2 and $NbSe_2$ monolayers were probed at room temperature with tunable conductivity measurements

14

using an external electric field. In the year of 2010, A. Kis' group from EPFL at Switzerland and S. Salahuddin's group from U. C. Berkeley in the US published their pioneer works on the experimental demonstration [90] and theoretical prediction [91], respectively, of monolayer MoS_2 field effect transistors (FETs). Soon after that, more groups joined this rapidly growing field of 2D semiconductors, and more potential applications with 2D TMDs were proposed, including logic integrated circuits [90-109], photodetectors [110-119], light-emitting devices [120-122,124,126-129], multi-purpose chemical sensing and bio-detection [163-167].

Up to now, the family of 2D materials has been continuously growing. The candidates for new 2D materials vary from graphene composites, like functionalized graphene, reduced graphene oxide etc. [168]; graphene analogues, like silicene, germanene and boronene [169-175]; to any materials with layered lattice structure, like metal chalcogenides, metal halides, transition metal oxides and trioxides, oxychalcogenides, III-V layered semiconductors, etc [176]. Quite a few of the upcoming 2D materials have been either experimentally demonstrated or theoretically examined. Among the various recently hot 2D materials, the discussion on atomicly thin black phosphorus, or "phosphorene", has been heating up gradually [177-182], because of the narrow direct band gap and anisotropic structure and properties of this novel star material. Furthermore, people have integrated different kinds of 2D materials and made them into van de Waals heterostructures [94,105,109,117,118,122-125,183-188]. Pioneering research attempts on the hybrid integrations of 2D materials include graphene/boron nitride high-mobility transistors [185], MoS_2/graphene ultrasensitive photodetectors [117,118], MoS_2/graphene Ohmic contacts for integrated circuits [105,183,184], all-2D-material flexible electronics [94,109], MoS_2/WSe_2 heterojunction light harvesting and light generations [122-125], etc. New concepts or new materials in 2D materials research keep refreshing the scope of what people can imagine, and the diversity of 2D materials now under serious investigation has given more possibilities for realizing real products with promising applications.

1.2 Significance of This Work

The aim of this thesis is to systematically study the optical properties of semiconducting 2D TMDs and to understand the many-body effects and the environmental effects in low-dimensional quantum-confined systems. The significance of this thesis is three folds. First, we will systematically study various optical characterizations of 2D TMDs and try to come up with a criterion to identify the type of the material and its specifications, like number of layers, quality, doping level, etc. Secondly, the interaction between 2D TMDs and their environments will be studied through optical measurements. As the 2D TMDs are atomically thin, the surface-to-volume ratio is extremely high. This means the interface can play an important role. In addition, these materials have to be placed on specific supporting materials to carry out most of the experiments. The environments may give rise to the effects of doping, strain, interference, dielectric screening etc., which are difficult to understand unless the multiple effects can be investigated separately. This thesis provides a good approach to study the electrical doping and dielectric screening effects individually. Thirdly, the many-body effects are prominent in low-dimensional materials. In particular, the picture of the exciton and the trion should be used to understand the optical phenomena in 2D TMDs. In this thesis, we will study various many-body effects that can be observed from optical measurements, including electron-electron interaction (band gap renormalization), electron-hole interaction (exciton), three-particle interaction (trion), electron-phonon interaction (Raman spectroscopy), etc.

1.3 Thesis Outline

The thesis is organized as follows:

In chapter 2, the basic knowledge of transition metal dichacogenides is introduced, including the chemical composition, lattice structure, electronic and optical properties, synthesis methods and potential applications.

In chapter 3, several optical characterization methods, such as Raman spectroscopy, photoluminescence and absorption measurement are introduced and used on both exfoliated and CVD-prepared TMDs, such as MoS_2, WS_2, $MoSe_2$ and WSe_2. A detailed

summary of the lattice symmetry, the vibrational modes and Raman peaks with different excitation lasers of bulk and monolayer MoS_2 is also given. The physical pictures of excitons and trions are also introduced, which can explain the PL and absorption results very well.

In chapter 4, the influence of the carrier density on the optical properties of monolayer MoS_2 is studied. Both the polymer electrolyte gating and conventional back gating technique are used to tune the Fermi level, and consequently the carrier density, within MoS_2. Transport, Raman spectroscopy, and PL measurements performed on monolayer MoS_2 with different carrier densities based the polymer electrolyte gating technique are described.

In chapter 5, the influence of the dielectric environments on the optical properties of monolayer MoS_2 is studied. MoS_2 films on SiO_2/Si substrates were immersed into a series of non-ionic organic solvents in order to obtain different external dielectric constants. Raman spectroscopy and PL measurements were taken on this system. The change of the PL signals can be explained by the dielectric screening effect on the excitonic quarsiparticles in monolayer MoS_2. A scaling relationship is also introduced to explain the experimental observations.

In chapter 6, a summary is presented, with a discussion of the future work for further study of the unique excitonic phenomenon in 2D TMDs and to attempt to utilize this material in novel optoelectronic devices.

Chapter 2. Basics of Transition Metal Dichalcogenides

2.1 Atomic Structure

The family of TMDs is composed of nearly 40 different compounds [189]. As shown in the periodic table in Figure 2-1, the highlighted transition metal and chalcogen chemical elements are the elements that are predominately crystalized into layered structures. The half colored elements can form layered dichalcogenides as well, but the same constituents can also form other crystal structures as that interesting phase transitions can occur. For example, NiS_2 is found to have a pyrite structure but $NiTe_2$ is a layered compound.

Figure 2-1 Chemical composition of layered transition metal dichalcogenides (LTMDs) [189]. The general chemical formula for LTMDs is given by MX_2, where M and X denote the transition metal and chalcogen elements, respectively. The S, Se, Te elements that are highlighted with orange are the choices for chalcogen elements, and the highlighted IVB, VB, VIB, VIIB, IXB and XB elements are common choices for the transition metal elements. Only part of the dichalcogenides formed by the half-colored IXB and XB elements exist stably in layered structures.

The unit cell of LTMDs consists of 1 transition metal atom and 2 chalcogen atoms. Accordingly, the general chemical formula is denoted by MX_2, in which M and X stand for the transition metal and the chalcogen element, respectively. Each layer of MX_2 is three-atoms thick, with 1 transition metal layer sandwiched between 2 chalcogen layers. The monolayer atomic structure can be either trigonal prismatic (e.g. MoS_2, NbS_2,) or octahedral (e.g. HfS_2, PtS_2), as shown in Figure 2-2.
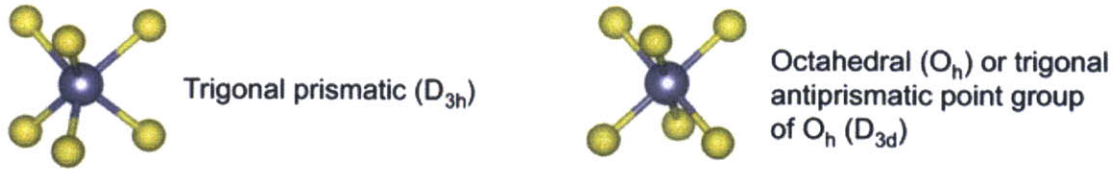
Figure 2-2 Trigonal prismatic (left) and octahedral (right) structure with the symmetry point groups indicated [189].

2.2 Electronic Properties

Depending on the configuration of the IVB-VIIIB transition metal and chalcogen elements, the physical properties of LTMDs vary significantly. Table 2-1 summarizes the basic electronic properties of the TMD family. The dichalcogenides are wide bandgap semiconductors when the metal elements are from Group IVB and VIB, and narrow bandgap semiconductors when the metal elements are from Group VIIB and VIII, whereas the Group VB dichalcogenides are metallic materials, and some of them are superconducting at low temperature. The electronic and optical properties depend strongly on the thickness of the TMDs, especially when they are less than 5 nm thick. If we take MoS_2 as an example, the optical bandgap can be varied from 1.2 eV to 1.9 eV when going from the bulk to the monolayer. MoS_2 with a thickness of more than 2 layers is an indirect band gap semiconductor, whereas it becomes a direct band gap semiconductor when thinned down to a monolayer. Other unique properties of monolayer or few-layer MoS_2 include a large excitonic binding energy, abundance of multi-excitons, strong electron-exciton interactions, dielectric-screened charge impurity scatterings, etc. All these phenomena in thin MoS_2 and other TMDs can be attributed to the quantum confinement effect, which is discussed later.

Table 2-1 Summary of the electronic properties of layered transition metal dichalcogenides [189-191]

Group	M	-X$_2$		
		-S$_2$	-Se$_2$	-Te$_2$
IVB	Ti	Semiconducting	Semiconducting	Semiconducting
	Hf	Semiconducting Bulk: 1.95 eV	Semiconducting Bulk: 1.15 eV	Semiconducting
	Zr	Semiconducting Bulk: 1.75 eV	Semiconducting	Semiconducting
VB	V	Metallic	Metallic	Metallic
	Nb	Metallic Superconducting	Metallic Superconducting	Metallic
	Ta	Metallic Superconducting	Metallic Superconducting	Metallic
VIB	Mo	Semiconducting 1L: 1.8 eV Bulk: 1.2 eV	Semiconducting 1L: 1.5 eV Bulk: 1.1 eV	Semiconducting 1L: 1.1 eV Bulk: 1.0 eV
	W	Semiconducting 1L: 2.1 eV Bulk: 1.4 eV	Semiconducting 1L: 1.7 eV Bulk: 1.2 eV	Semiconducting 1L: 1.1 eV
VIIB	Tc			
	Re	Semiconducting	Semiconducting	
VIII	Pd	Semiconducting	Semiconducting	Metallic Superconducting
	Pt	Semiconducting Bulk: 0.7 eV	Semiconducting Bulk: 0.1 eV	Metallic

The calculated dispersion relations of mono-, bi-layer and bulk MoS$_2$ are shown in Figure 2-3 [147]. Both the conduction band minimum (CBM) and the valence band maximum (VBM) are seen to be located at the K point in the Brillioun zone in monolayer MoS$_2$, which makes it a direct band gap semiconductor. In the case of bi-layer and bulk MoS$_2$, however, the VBM moves to the Gamma point. Near the K point, there are two sub-bands near the VBM with a splitting of around 200 meV [144-149]. These two sub-bands belong to the K and K' valley in the Brillioun zone, respectively, with opposite electron spins at K and K' [147]. Due to the prominent many-body effect in quantum-confined low-dimension systems, the band structure obtained from single-particle density functional theory (DFT) would no longer be valid: An electron self-energy renormalization term has to be considered in the DFT calculation [144-152]. One of the

revised models including the above-mentioned many body effect is called the self-consistent quasiparticle GW method [144-149,151,152]. This model gives an anticipation of the band gap with the value of 2.4-2.8 eV, which is much higher than the optical band gap observed from absorption or photoluminescence measurements [88,89]. The discrepancy can be resolved by the introduction of the electron-hole interactions, another form of the many-body effect, which is discussed in the next section. The BSE method [145,151,152] and Mott-Wannier model [145,147] consider the electron-hole interactions and provide a good estimation of the optical band gap for the TMDs. Table 2-2 summarizes the theoretical values of the band gap of monolayer MoS_2. Researchers have successfully measured the electronic quasiparticle band gaps of several TMD monolayers, such as $MoSe_2$ and MoS_2, by either angle-resolved photoemission spectroscopy (ARPES) [192,193] or scanning tunneling microscopy (STM) [194-196], with the values of the band gaps roughly in accordance with the theoretical calculations as shown in Table 2-2.
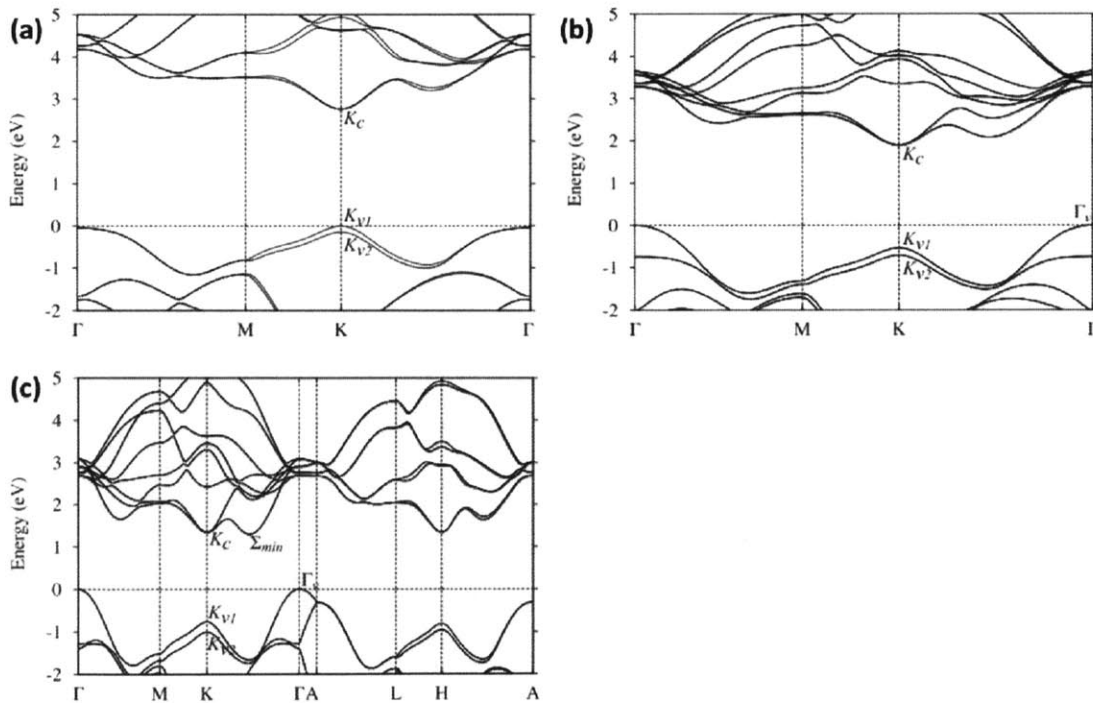
Figure 2-3 Electronic band structure of (a) monolayer, (b) bilayer and (c) bulk MoS_2. The band structures were obtained by the GW method, and adopted here from [147].

22

Table 2-2 Literature theoretical values of band gaps of monolayer MoS_2 from literature

Method	Value (eV)	Ref.	Notes
Theory (DFT)	1.6	[145]	No many-body effects considered
	2.05	[145]	
	1.74	[148]	
	1.69	[149]	
	1.7	[152]	
Theory (GW)	2.84	[144]	Considering the electron-electron self-energy renormalization; a good estimation of the electronic quasiparticle band gap
	2.82	[145]	
	2.77	[146]	
	2.759	[147]	
	2.78	[148]	
	2.41	[149]	
	2.97	[151]	
	2.4	[152]	
Theory (BSE)	1.78	[145]	Considering both the electron-electron interaction and the electron-hole interactions; a good estimation of the optical band gap
	1.8	[151]	
	2.0	[152]	
Theory (Mott-Wannier)	1.97	[145]	Considering the existence of the exciton binding energy; a good estimation of the optical band gap
	1.862	[147]	

2.3 Optical Transitions, Excitons and Trions

In direct band gap semiconductors, electrons in the valence bands can be easily excited to the conduction bands by incident photons, and the excess carriers can also recombine, passing the excess energies to photons, as shown in Figure 2-4(a). The former process can be probed by light absorption measurements, and the latter process can be probed by photoluminescence (PL) measurements. If lattice vibrations or phonons are involved in the optical transitions, the generated photon can have a lower energy than the incident photon, and the energy difference is related to a specific phonon modes. This inelastic light scattering is called Raman scattering (see Figure 2-4(b)).

(a) CBM

$\hbar\omega_0$

$\hbar\omega$

VBM

Absorption & PL

(b) $\hbar\omega_q$

$\hbar\omega_0$ $\hbar\omega_0-\hbar\omega_q$

$E_0+\hbar\omega_q$

E_0
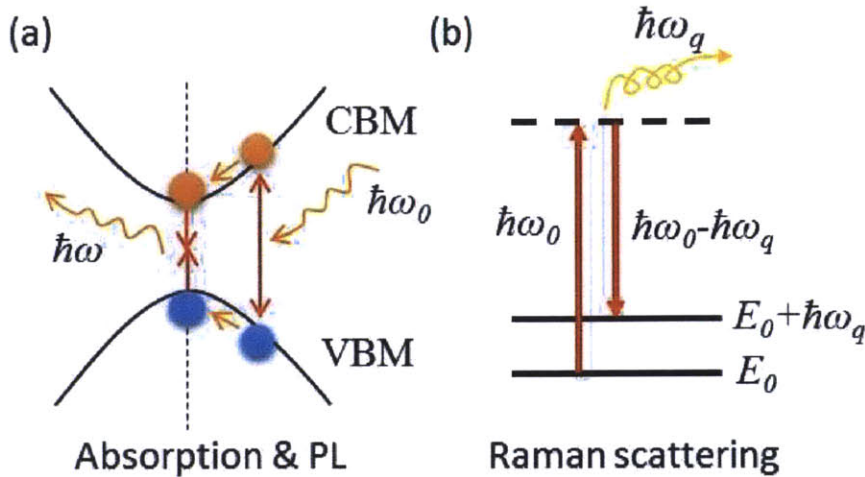
Raman scattering

Figure 2-4 Schematics of (a) the light absorption ($\hbar\omega_0$) and the photoluminescence (PL, $\hbar\omega$) process and (b) the Raman scattering process. Here $\hbar\omega_0$ is the energy of the incident light, $\hbar\omega$ is the energy of the emitted light in the PL process, and $\hbar\omega_q$ is the energy of the emitted phonon in the Raman scattering process. VBM is short for valence band maximum, and CBM is short for conduction band minimum. E_0 is the ground energy state.

In 2D semiconducting TMDs, light-generated electrons and holes tend to attract each other due to the strong Coulomb interactions between them. This can be modeled by the concept of the exciton, which is the combination quasiparticle state of an electron and an hole. In addition, multi-excitons, such as trions and bi-excitons, are observable in 2D TMDs even at room temperature [153-157]. Figure 2-5 shows the PL spectra of monolayer $MoSe_2$ in the energy range from 1.52 to 1.68 eV for temperatures between 15 K and 295 K (room temperature). From these results we can clearly see the evolution of the exciton and trion peaks as a function of temperature, and how the peaks are separated at low temperature and are merged into a single peak with some asymmetry at room temperature.
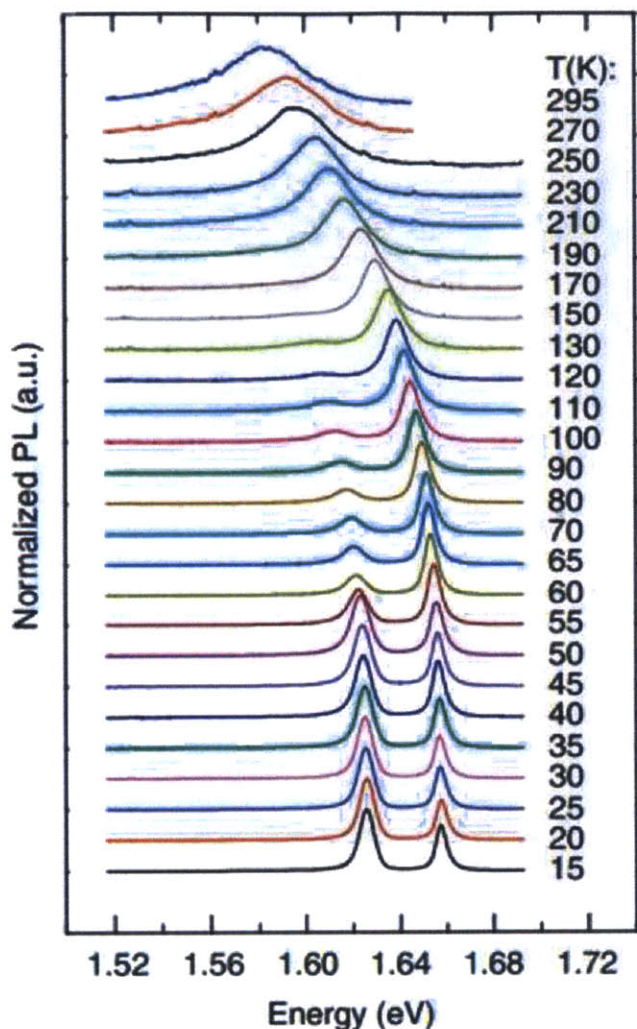
Figure 2-5 The PL spectra of monolayer MoSe$_2$ in the photon energy range 1.52-1.68 eV for temperature between 15 and 295 K [154]. The peaks at around 1.62 eV and at 1.65 eV correspond to the trion and exciton transitions, respectively.

2.4 Synthesis Methods and Applications

Similar to graphene, the monolayer TMDs were first obtained by mechanical exfoliation, using the Scotch tape method [88]. More recently, various semiconducting LTMDs, such as MoS$_2$, MoSe$_2$, WS$_2$ and WSe$_2$, have been synthesized through chemical vapor deposition (CVD) [133-142] or physical vapor deposition (PVD) [132]. The experimental setup for the CVD synthesis of MoS$_2$ is schematically shown in Figure 2-6. MoO$_3$ and sulfur powder are used as the solid precursors, and placed in separate ceramic boats. The

substrate is treated with specific seeding molecules [133,137]. The growth temperature is 650 °C. At such a high temperature, the precursors are evaporated, led to the substrate surface by the nitrogen gas flow, and the precursors are reacted to form MoS_2. MoS_2 thin films with high crystallinity can be obtained using the seeds as the nucleation centers or as epitaxial templates. Other precursors have also been studied in MoS_2 CVD synthesis, such as $(NH_4)_2MoS_2$, Mo film, and $MoCl_4$ [133-142]. In terms of the PVD method, on the other hand, MoS_2 powders are evaporated at high temperature (900 °C) and re-deposited onto the target substrates [132]. Figure 2-7 shows the optical images of monolayer MoS_2 synthesized by PVD and CVD. Although triangular domains were observed from both CVD and PVD method, the CVD MoS_2 approach turned out to have much better quality with larger domain sizes.
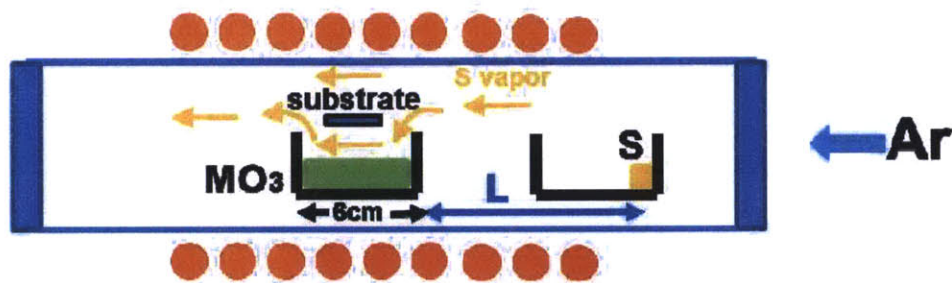
Figure 2-6 Schematic of the experimental setup of MoS_2 synthesis by chemical vapor deposition. [133]
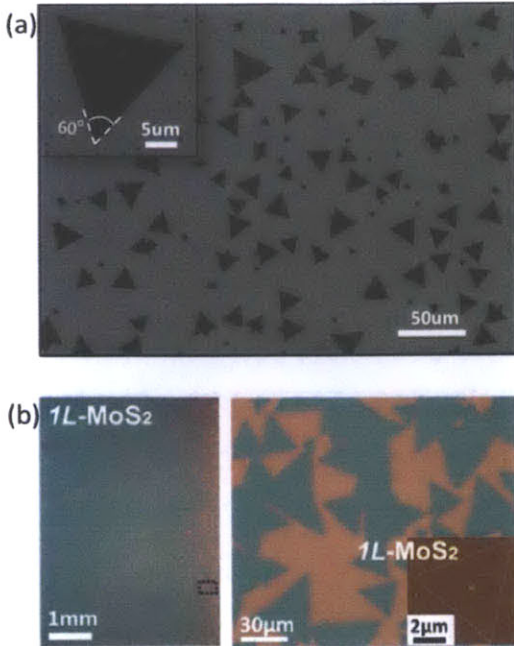
Figure 2-7 Optical image of monolayer MoS$_2$ triangular domains synthesized by (a) physical vapor deposition (PVD) [132] and (b) chemical vapor deposition (CVD) [134].

Because of the existence of a band gap, MoS$_2$ field effect transistors (FETs) were proposed to have a high on/off ratio, which has not been achieved on graphene FETs, so that MoS$_2$ FETs can potentially be used in nanoscale logic electronics [90-109,197-201]. MoS$_2$ can be made into good n-type FETs, with a field-effect mobility of ~190 cm^2/Vs and an on/off ratio of ~10^9 (see Figure 2-8) [197]. Based on such achievements, several typical logic cells were fabricated, such as inverters, NAND gates, random access memories and ring oscillators [104,197]. P-type MoS$_2$ FETs are difficult to realize, because both exfoliated and CVD MoS$_2$ are naturally n-type doped, and the work functions of most of the commonly used contact metals are pinned near the conduction band edge [97], as shown in Figure 2-9. However, if we look into MoSe$_2$ or WSe$_2$ with lower band gaps, it is possible to shift the Fermi level to the p-type side with a gate bias, and thus both n-type and p-type FETs, or even bipolar FETs can be made [198-201].
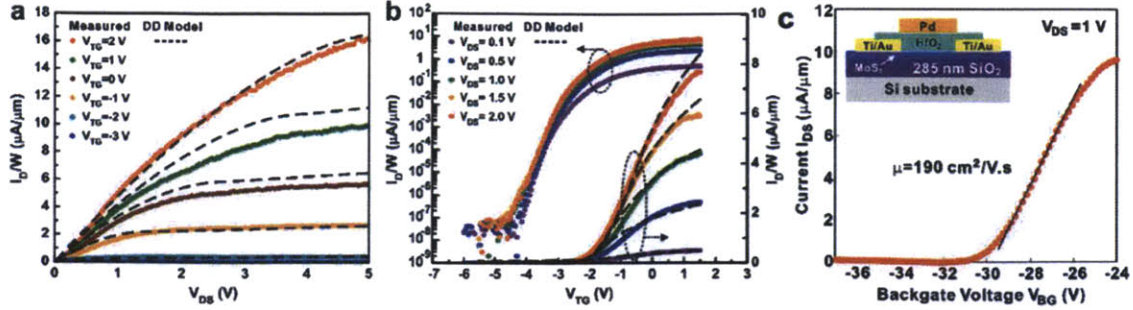
Figure 2-8 Transport measurements of CVD MoS$_2$ top-gate FETs [197]. (a) output characteristics, (b) transfer characteristics and (c) back-gate transfer characteristics for the extraction of the field effect mobility. In (b), the drain current density (I_D/W) is plotted in both log scale (left axis) and linear scale (right axis). The inset in (c) is the schematic of the device structure in the side view.
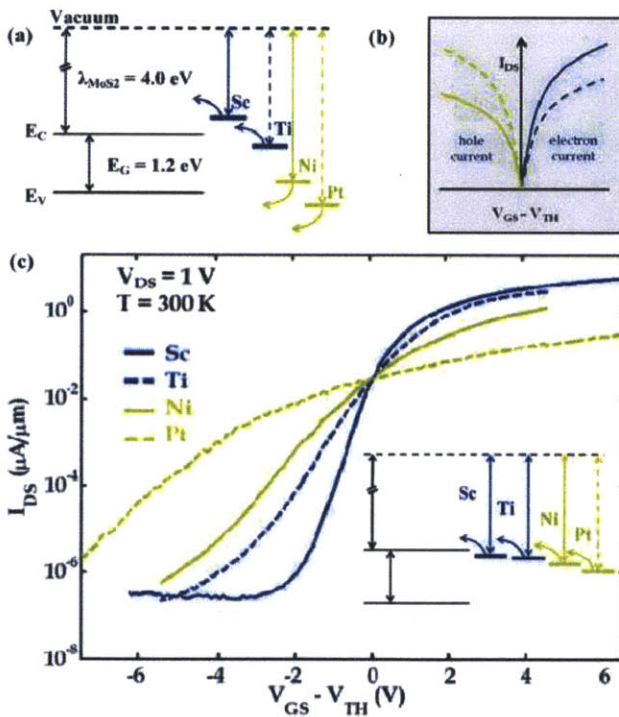
Figure 2-9 (a) Expected line-up of metal Fermi level with the electronic bands of MoS$_2$ flake if only the difference of the electron affinity of MoS$_2$ and the work function of the corresponding metal is considered. (b) The cartoon of expected transfer characteristics based on (a). (c) Transfer characteristics of back-gated 6-nm-thick MoS$_2$ transistor with Sc, Ti, Ni, and Pt metal contacts. The inset shows the actual line-up based on the experimental data. [97]

28

The direct band gap nature makes LTMDs promising to be used in high-performance optoelectronics as well, such as photodetectors, light-emitting diodes (LEDs) and so on [110-131].The structure of a MoS_2 photodetector is quite similar to that of a MoS_2 FET, as shown in Figure 2-10(a). When shining a laser onto the device, more electrons and holes are generated, leading to either a large photocurrent when the source-drain voltage is 0, or a large photoconductivity when the voltage is not 0. Figure 2-10(b) plots the time-domain photocurrent responses with different working biases applied to the MoS_2-based photodetectors. It was reported that the photoresponsivity could be as high as 880 A W^{-1} at an excitation wavelength of 561 nm [113]. According to M. Buscema et al. [115], the photocarriers in MoS_2 are mainly generated around MoS_2/metal interfaces. The consequent photoresponse results from the photo-thermoelectric effect, rather than from the commonly observed photovoltaic effect in bulk semiconductors [115].The effect of persistent photoconductivity (PPC) is also widely reported [116,117], which may originate from the deep trap states in MoS_2. Similar studies on the photoresponse of monolayer WS_2 have been done as well [119]. The mechanism of lighting in LEDs is basically the electroluminescence effect occurring in a MoS_2 diode. Due to its direct band gap nature, excited electrons and holes in semiconductor TMD monolayers can be easily recombined radiatively, and thus emitting light [120]. Earlier research has shown a strong photoluminescence in monolayer MoS_2; the observation of electroluminescence was first reported for MoS_2/metal and MoS_2/p-Si heterojunctions [120,124]. Figure 2-11 shows the electroluminescence observed near the MoS_2/Au Schottky junction as well as the photoluminescence and absorption spectra. The wavelength of the emitted light is at around 680 nm [120]. More recently, three research groups [126-128] reported gate-tunable WSe2 p-n diodes, which give better performance in both light emitting and photodetecting. Heterojunctions of different TMDs have also been studied [121-124], with better rectifying behavior and improved efficiency of the photon-to-electron or the electron-to-photon transitions. Researchers believe that the TMD family would eventually provide a feasible solution for high performance optoelectronics either integrated with silicon integrated circuits or fabricated on flexible substrates.
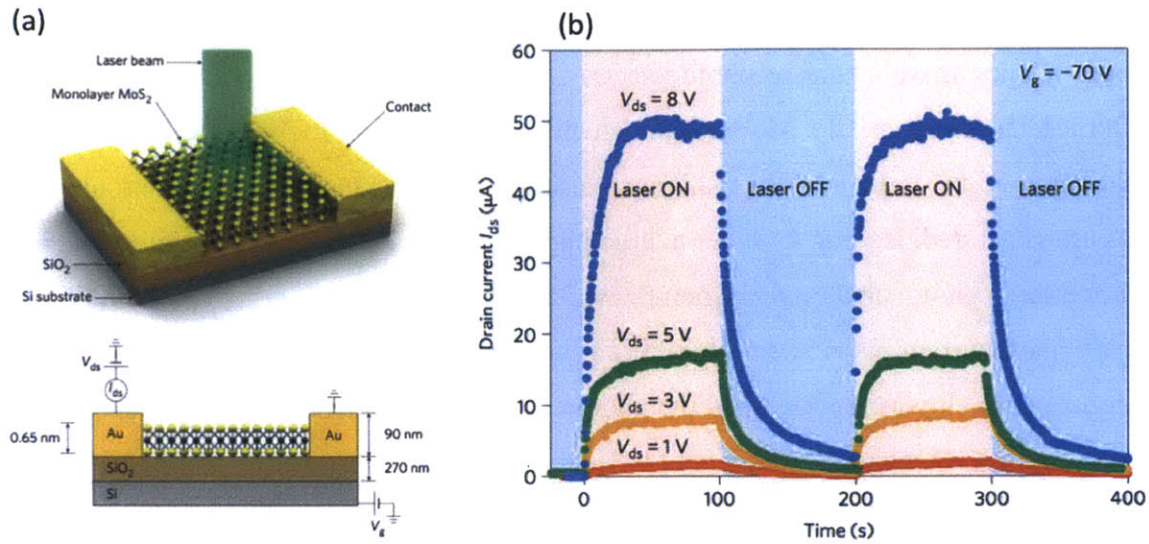
Figure 2-10 MoS$_2$ photodetector. (a) device schematics. (b) time domain photoresponse of the photodetector. [113]
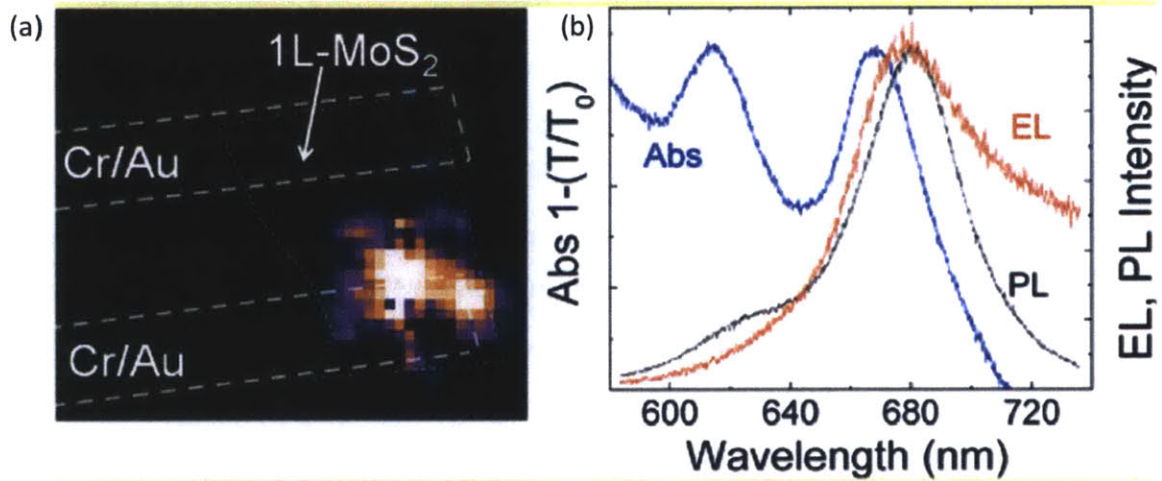
Figure 2-11 (a) Electroluminescence mapping and (a) absorption, electroluminescence and photoluminescence spectra of monolayer MoS$_2$ with Cr/Au metal contacts [120].

Chapter 3. Raman Spectroscopy, Photoluminescence and Absorption of Monolayer TMDs

In this chapter, several basic optical characterizations, including Raman spectroscopy, photoluminescence (PL) and ultraviolet-visible light (UV-Vis) absorption, on TMDs prepared by both the exfoliation method and the CVD method are introduced and discussed. Raman spectroscopy results provide information on lattice vibrational modes and the phonon-electron interactions, whereas PL and UV-Vis absorption provide information on the electronic energy band gap and the radiative transitions of the TMDs.

3.1 Raman Spectroscopy

3.1.1 Lattice Structure and Vibrational Modes [202,203]

TMDs are composed of stacked layers of chalcogen-metal-chalcogen sandwiches which are hexagonal structures, 3 atomic layers in thickness and with weak van der Waals interactions between the layers. Figure 3-1 shows the schematic lattice structure of MX_2 (M=Mo or W, X=S or Se) as an example. The bulk TMDs belong to the space group D_{6h} (P6$_3$/mmc). There are 6 atoms – 2 M atoms and 4 X atoms within two adjacent layers – in the primitive unit cell. Each atom in the primitive unit cell has 3 freedom of movement, so there are 18 vibrational modes in bulk TMDs, including 3 acoustic modes, 7 Raman modes, 3 infrared (IR) modes, and 5 inactive modes. The irreducible representations of the lattice vibrational modes are given by

$$\Gamma = A_{1g} \oplus 2A_{2u} \oplus B_{1u} \oplus 2B_{2g} \oplus E_{1g} \oplus 2E_{1u} \oplus E_{2u} \oplus 2E_{2g} \qquad (3\text{-}1)$$

Figure 3-2(a) summarizes the vibrational modes of the atoms within the primitive cell of bulk TMD materials. Among the vibrational modes, one of the $2A_{2u}$ and one of the $2E_{1u}$ are acoustical modes; the other A_{2u} and the other E_{1u} are infrared (IR) active modes; the $2E_{2g}$, E_{1g} and A_{1g} are Raman active modes; the others are optical inactive modes. The A and B modes are out-of-plane or breathing modes, whereas the E modes are in-plane or

shear modes. Each in-plane mode (E mode) has two-fold degeneracy (only the vibrations in x axis are shown in the Figure).
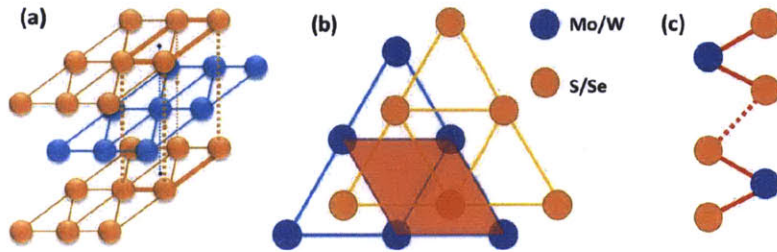
Figure 3-1 Lattice structures of MX$_2$. M or blue circle stands for Mo or W atom, and X or orange circle stands for S or Se atom. (a) 3-dimensional lattice of 3-atom-thick monolayer MX$_2$. (b) The projection of the lattice of monolayer MX$_2$ in the x-y plane. The red shaded region is the primitive unit cell in the x-y plane, containing two S/Se atoms (on the top and bottom layers of the 3-atom-layer structure, respectively, with the same x and y coordinates) and one Mo/W atom. (c) Representative lattice of bulk MX$_2$ in the z-direction.

For monolayer MX$_2$, however, the primitive unit cell becomes only half of its bulk form, that is, one layer containing 1 M atom and 2 X atoms. The monolayer MX$_2$ belongs to the space group D$_{3h}$ ($P\bar{6}m2$). There are 9 vibrational modes in total, including 3 acoustic modes, 5 Raman modes and 3 IR modes. The irreducible representations of the lattice vibrational modes are given by

$$\Gamma = A_1' \oplus E'' \oplus 2A_2'' \oplus 2E' \tag{3-2}$$

Figure 3-2(b) shows the vibrational modes of the monolayer MX$_2$. Each column of the vibrational modes in Figure 3-2(a) corresponds to a single vibrational mode as the material evolves from bulk to monolayer form. The symmetries of n-layer TMDs are more complicated, and some interlayer modes become Raman active, which cannot be observed in the monolayer or bulk case. This is beyond the scope of this thesis, and can be found in the reports from other groups [203,204].

(a)

E$_{1u}$ (Acoustic) A$_{2u}$ (Acoustic) E$_{1g}$ (Raman) A$_{1g}$ (Raman) E$_{2g}$ (Raman) A$_{2u}$ (IR)

E$_{2g}$ (Raman) B$_{2g}$ (Inactive) E$_{2u}$ (Inactive) B$_{1u}$ (Inactive) E$_{1u}$ (IR) B$_{2g}$ (Inactive)

(b)

E' (Acoustic) A''$_2$ (Acoustic) E'' (Raman) A'$_1$ (Raman) E' (IR+Raman) A''$_2$ (IR)
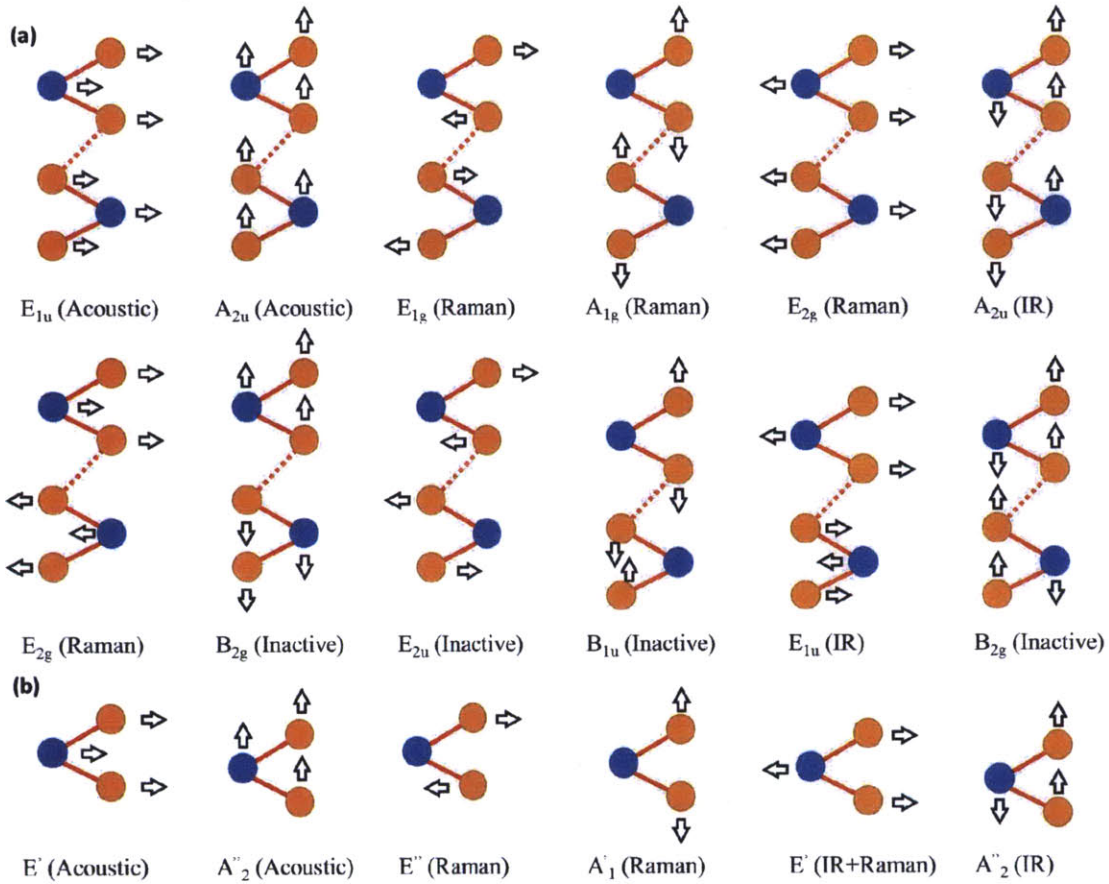
Figure 3-2 Lattice vibrational modes of (a) bulk and (b) monolayer MX$_2$. M or blue circle stands for Mo or W atom, and X or orange circle stands for S or Se atom. The arrows represent the directions and positive signs of the atom vibrations.

Figure 3-3 shows the calculated phonon dispersion relations $\omega(q)$ of monolayer and bulk MoS$_2$ [205]. The branches around the Γ point in the Brillioun zone are assigned to the acoustic modes and Raman-active vibrational modes as well, as noted in the figures.

33
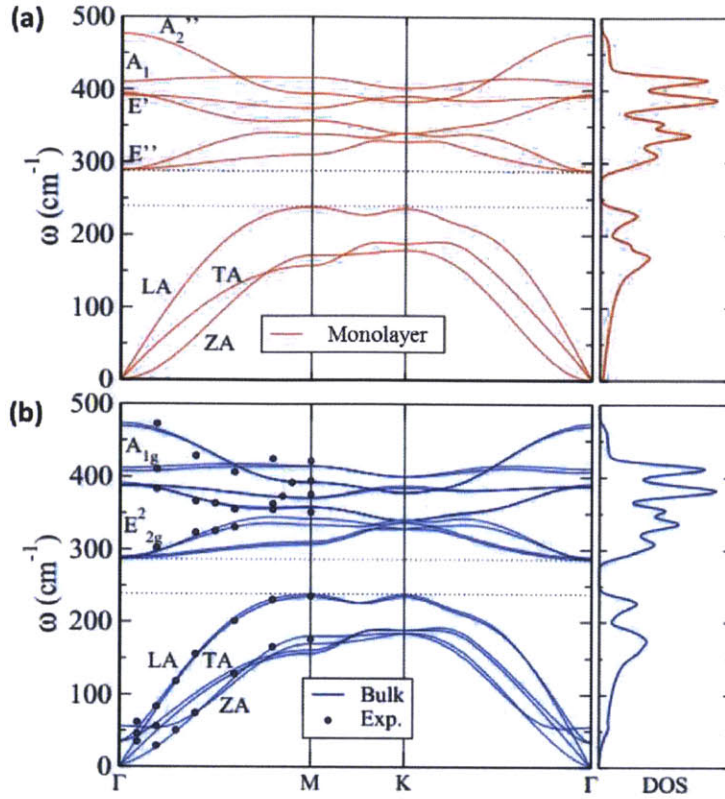
Figure 3-3 Phonon dispersion relations $\omega(q)$ of (a) monolayer and (b) bulk MoS$_2$. The results are based on theoretical calculations and adapted from [205].

3.1.2 Raman Spectra

The seven Raman active vibrational modes in bulk form of TMDs include E_{1g}, E_{2g}^1, E_{2g}^2 and A_{1g} (Figure 3-2). The E_{2g}^2 mode is located in the low frequency range (<100 cm^{-1}), which cannot be detected by a standard Raman system because of the issues of the laser linewidth and the cutoff edge of the filter. However, the other two modes, with symmetries E_{2g}^1 and A_{1g}, located at 384 cm^{-1} and 405 cm^{-1} respectively, can be easily observed. The E_{1g} mode should be around 280 cm^{-1}, but neither our group nor other researchers have observed it. Figure 3-4 shows the Raman spectra of the E_{2g}^1 and A_{1g} modes of MoS$_2$ samples with different layer numbers prepared by the mechanical exfoliation method under the 532 nm excitation laser. The E_{2g}^1 mode stiffens from 383 cm^{-1} to 384 cm^{-1} and the A_{1g} mode softens from 408 cm^{-1} to 403 cm^{-1} when MoS$_2$ is thinned down from bulk to monolayer, similar to the reports from other groups [206,207].

The Raman shifts as a function of the layer number of MoS_2 are plotted in Figure 3-5(a). We can use the difference in Raman shift between these two peaks to quickly decide the layer number of MoS_2, as shown in Figure 3-5(b).
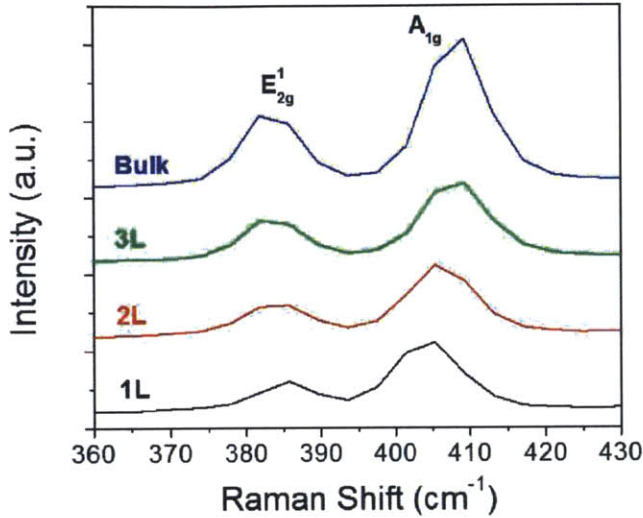
Figure 3-4 Raman spectra of exfoliated MoS_2 with different numbers of layers.
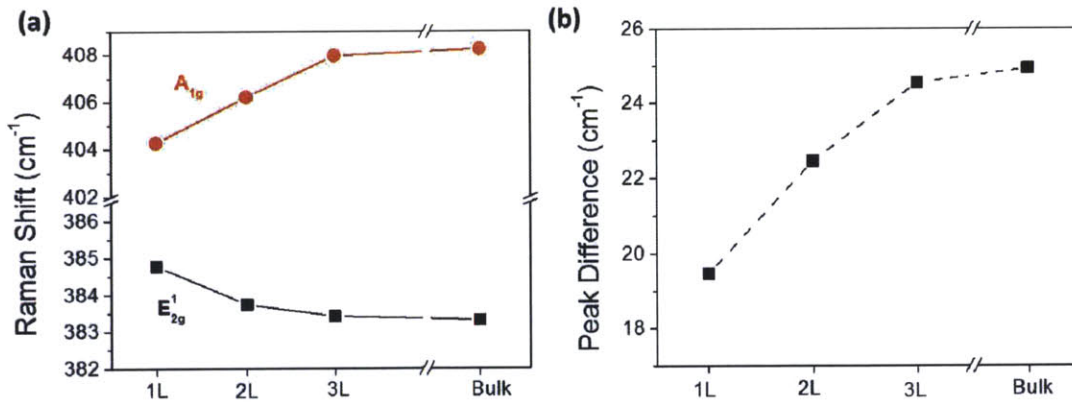
Figure 3-5 (a) Peak positions of the E_{2g}^1 (black) and A_{1g} (red) Raman vibrational modes of exfoliated MoS_2 as a function of the number of layers. (b) Peak position difference between the E_{2g}^1 and A_{1g} Raman vibrational modes as a function of the number of layers in an MoS_2 sample.

Figure 3-6 to 3-9 summarize typical Raman fingerprints of monolayer MoS_2, WS_2, $MoSe_2$ and WSe_2 synthesized by chemical vapor deposition. The spectra of the sulfides were taken under the 532 nm laser, and those of the selenides were taken under the 633 nm laser. The (a) panel of each figure demonstrates the strong peaks that are easily observable, which can be used as the indicators of the materials. Two peaks at 384 cm^{-1} and 405 cm^{-1} were observed on CVD monolayer MoS_2, the same as that observed on exfoliated monolayer MoS_2. There are three major Raman peaks on CVD monolayer WS_2, located at 322 cm^{-1}, 351 cm^{-1} and 420 cm^{-1}, respectively, as shown in Figure 3-7(a). The asymmetric peak at 351 cm^{-1} corresponds to the overtone of the E' (or E_{2g}^1) and the 2LA(M) modes; the 420 cm^{-1} peak is from the A_1' (or A_{1g}) vibrational mode; and the origin of the 322 cm^{-1} mode is attributed to the second-order Raman resonance: the LA(M)+TA(M) mode. The peak at 242 cm^{-1} in Figure 3-8(a) is from the A_1' (or A_{1g}) vibrations, which is the only strong peak observed on monolayer $MoSe_2$. In Figure 3-9(a), the peak for WSe_2 at 250 cm^{-1} is the overtone of the E' (or E_{2g}^1) and A_1' (or A_{1g}) modes. These two modes can be separated if we collect and separate the polarizations of the emitted light [208]. The small peak at 261 cm^{-1} is the second-order 2LA(M) resonance. The (b) panels in Figure 3-6 to 3-9 show the fine spectra of these four TMDs with more high-order resonant peaks. Following the studies of other groups [202-209,211-214], the assignments of the high-order resonant peaks are shown with the spectra as well. Table 3-1 to Table 3-4 summarize the Raman modes of these four TMDs in both monolayer and bulk form observed under different excitation laser wavelengths. Since some of the laser energies are close to the exciton peak energies (Table 3-5), multiple second order or third order Raman resonance modes can be excited and detected. Some of the modes that are supposed to be Raman-inactive have also been reported, probably because of the broken of symmetry due to the effect of the substrates or the symmetry change when the number of layers becomes finite [214]. Additional interlayer shear and breathing modes were found in the low-frequency range for few-layer TMDs, which has been discussed by others [203,204].
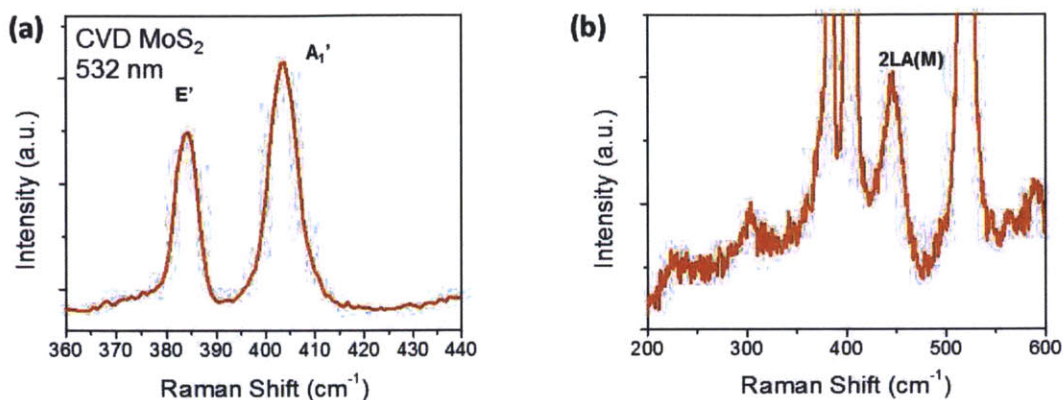
Figure 3-6 Raman spectrum of monolayer MoS_2 synthesized by chemical vapor deposition. (a) and (b) are the same spectra with different scales. The spectra were taken with the excitation wavelength of 532 nm.
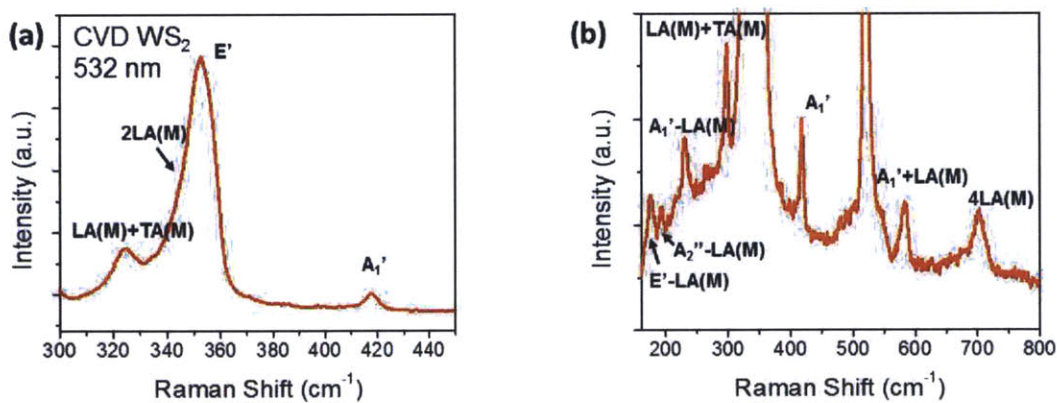
Figure 3-7 Raman spectrum of monolayer WS_2 synthesized by chemical vapor deposition. (a) and (b) are the same spectra with different scales. The spectra were taken with the excitation wavelength of 532 nm.
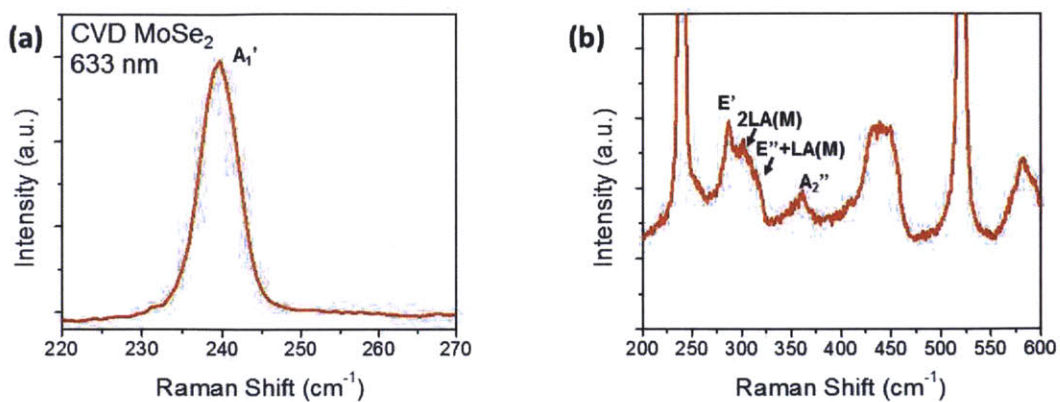
Figure 3-8 Raman spectrum of monolayer MoSe₂ synthesized by chemical vapor deposition. (a) and (b) are the same spectra with different scales. The spectra were taken with the excitation wavelength of 633 nm.
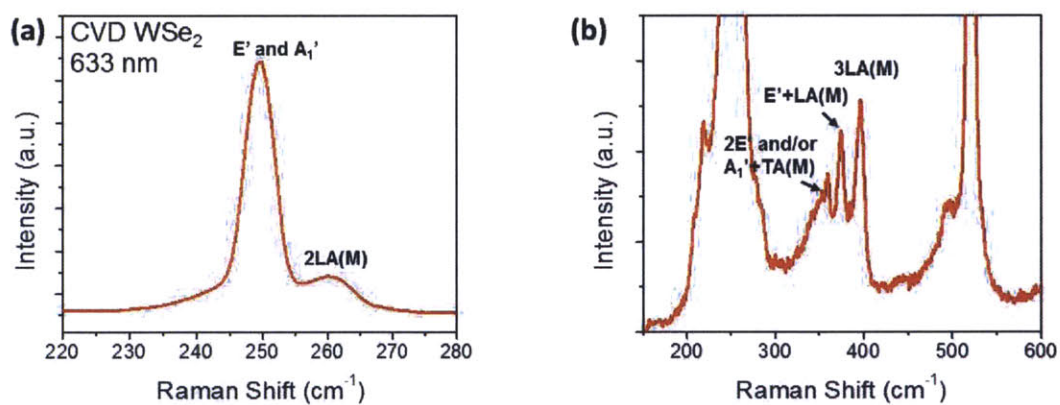
Figure 3-9 Raman spectrum of monolayer WSe₂ synthesized by chemical vapor deposition. (a) and (b) are the same spectra with different scales. The spectra were taken with the excitation wavelength of 633 nm.

Table 3-1 Summary of the Raman peaks of monolayer MoS_2 as determined with different laser excitation wavelengths. The polarization conditions (in Porto notation [210]) and the phonon mode assignments are also indicated after each data entry. The underlined modes are the high-intensity (major) peaks in each measurement. [203,204,206,207,209]

Excitation Wavelength	Peak Position (cm^{-1}), Polarization and Phonon Mode Assignment	
	Monolayer	Bulk
325 nm	<u>384</u> (E'), <u>405</u>(A_1')	<u>383</u> (E_{2g}^{1}), <u>408</u> (A_{1g})
488 nm	<u>385</u> (E'), <u>403</u>(A_1')	<u>383</u> (E_{2g}^{1}), <u>408</u> (A_{1g})
514 nm	<u>385</u> (E'), <u>403</u>(A_1')	<u>382</u> (E_{2g}^{1}), <u>408</u> (A_{1g})
532 nm	<u>384</u> ($\bar{z}(xx)z, \bar{z}(xy)z$; E'), <u>403</u> ($\bar{z}(xx)z$; A_1')	32 ($\bar{z}(xx)z, \bar{z}(xy)z$; E_{2g}^{2}), <u>383</u> ($\bar{z}(xx)z, \bar{z}(xy)z$; E_{2g}^{1}), <u>408</u> ($\bar{z}(xx)z$; A_{1g})
633 nm	38 (CBS*), <u>385</u> (E'), <u>404</u>(A_1'), 414 (B_{1u}), 440 (OS**), <u>450</u> (2LA(M)), 459 (A_{2u})	38 (CBS), 180 (A_{1g}-LA(M)), <u>382</u> (E_{2g}^{1}), <u>407</u> (A_{1g}), 414 (B_{1u}), <u>450</u> (2LA(M)), 459 (A_{2u}) , 634 (A_{1g}+LA(M))

Notes:

*CBS: conduction band splitting

**OS: oxysulfide species

Table 3-2 Summary of the Raman peaks of monolayer WS_2 as determined with different laser excitation wavelengths. [208,211]

Excitation Wavelength	Peak Position (cm^{-1}), Polarization and Phonon Mode Assignment	
	Monolayer	Bulk
473 nm	298 (2ZA(M)), <u>350</u> (2LA(M)), <u>357</u> ($\bar{z}(xx)z, \bar{z}(xy)z$; E'), <u>418</u> ($\bar{z}(xx)z$; A_1'),	298 (2ZA(M)), <u>350</u> (2LA(M)), <u>356</u> ($\bar{z}(xx)z, \bar{z}(xy)z$; E_{2g}^{1}), <u>420</u> ($\bar{z}(xx)z$; A_{1g}),

	522 (E'+LA(M))	522 (E_{2g}^1+LA(M))
488 nm	176 (LA(M)), 351 (2LA(M)), 356 (E'), 418 (A_1'),	351 (2LA(M)), 356 (E_{2g}^1), 420 (A_{1g}),
514 nm	176 (LA(M)), 190, 213, 230(A_1'-LA(M)), 264 ($2LA-3E_{2g}^2$(M))**, 297 ($2LA-3E_{2g}^2$(M))*, 312, 324, 351 (2LA(M)), 355 (E'), 417 (A_1'), 582 (A_1'+LA(M)) 704 (4LA(M))	350 (2LA(M)), 355 (E_{2g}^1), 420 (A_{1g}),
532 nm	173 (E'-LA(M)), 194 (A_2''-LA(M)), 231 (A_1'-LA(M)), 265 (A_1'-ZA(M))**, 298 (2ZA(M))*, 326 (LA+TA(M)), 352 (2LA(M)), ~360 (E'), ~420 (A_1'), 522 (E'+LA(M))	170(E_{2g}^1-LA(M)), 173 (E_{2g}^1-LA(M)), 194 (B_{2g}-LA(M)), 231 (A_{1g}-LA(M)), 265 (A_{1g}-ZA(M)), 298 (2ZA(M)), 311 (unknown), 326 (LA+TA(M)), 351 (2LA(M)), ~360 (E_{2g}^1), ~420 (A_{1g}), 522 (E_{2g}^1+LA(M))
633 nm	173 (E'-LA(M)), 194 (A_2''-LA(M)), 231 (A_1'-LA(M)), 265 (A_1'-ZA(M)), 298 (2ZA(M)), 311 (unknown), 326 (LA+TA(M)), 350 (2LA(M)), ~420 (A_1'), 522 (E'+LA(M))	173 (E_{2g}^1-LA(M)), 194 (B_{2g}-LA(M)), 231 (A_{1g}-LA(M)), 265 (A_{1g}-ZA(M)), 298 (2ZA(M)), 311 (unknown), 326 (LA+TA(M)), 350 (2LA(M)), ~420 (A_{1g}), 522 (E_{2g}^1+LA(M))
647 nm	350 (2LA(M)), 355 (E'), 417 (A_1'),	351 (2LA(M)), 355 (E_{2g}^1), 421 (A_{1g}),

Table 3-3 Summary of the Raman peaks of monolayer $MoSe_2$ as determined with different laser excitation wavelengths. [209,212,213]

Excitation Wavelength	Peak Position (cm^{-1}), Polarization and Phonon Mode Assignment	
	Monolayer	Bulk
442 nm		169 (E_{1g}), <u>242</u> (A_{1g}), 285 (E_{2g}^1), 352 (A_{2u}),
514 nm	~150 (LA(M)), ~165 (E"), <u>243</u> (A_1'), 286 (E'), ~310 (2LA(M)), ~318 (E"+LA(M)), ~408 (E"+ A_1') , ~436 (E'+LA(M)), ~471 (E'+ E")	<u>241</u> (A_{1g}), 287 (E_{2g}^1)
532 nm		169 (E_{1g}), 242 (A_{1g}), 285 (E_{2g}^1), 352 (A_{2u}),

Table 3-4 Summary of the Raman peaks of monolayer WSe_2 as determined with different laser excitation wavelengths. [203,208,209,213,214]

Excitation Wavelength	Peak Position (cm^{-1}), Polarization and Phonon Mode Assignment	
	Monolayer	Bulk
473 nm	<u>249</u> ($\bar{z}(xy)z$; E'), <u>249</u> ($\bar{z}(xx)z$; A_1'), <u>260</u> (2LA(M)), 360 (E" (Γ) or A_1'+TA(M)), 373 (E'+LA(M)), 394 (3LA(M))	<u>248</u> ($\bar{z}(xy)z$; E_{2g}^1), <u>251</u> ($\bar{z}(xx)z$; A_{1g}), <u>260</u> (2LA(M)), 308 (B_{2g}^1), 360 (2E_{1g}(Γ) or A_{1g}+TA(M)), 373 (E_{2g}^1+LA(M)), 394 (3LA(M))
514 nm	~114 (LA(M)), 136 (A_{1g}-LA(M)), <u>249</u> (E' and/or A_1') 360 (2 E" (Γ) or A_{1g}+TA(M)), 373 (E'+LA(M)), 394 (3LA(M) or 2A_1'-LA(M))	<u>248</u> (E_{2g}^1), <u>251</u> (A_{1g})
532 nm		24 ($\bar{z}(xx)z$, $\bar{z}(xy)z$; E_{2g}^2),

	136 (A₁'-LA(M)), $\underline{250}$ ($\bar{z}(xx)z, \bar{z}(xy)z$; E' and/or A₁'), $\underline{262}$ ($\bar{z}(xx)z, \bar{z}(xy)z$; 2LA(M)), 360 (2E" (Γ) or A₁'+TA(M)), 373 (E'+LA(M)), 394 (3LA(M))	136 (A₁g-LA(M)), $\underline{250}$ ($\bar{z}(xx)z, \bar{z}(xy)z$; E₂g¹ and/or A₁g), $\underline{257}$ ($\bar{z}(xx)z, \bar{z}(xy)z$; 2LA(M)), 307 (B₂g¹), 360 (2E₁g(Γ) or A₁g+TA(M)), 373 (E₂g¹+LA(M)), 394 (3LA(M))
633 nm	136 (A₁'-LA(M)), $\underline{250}$ ($\bar{z}(xy)z$; E'), $\underline{250}$ ($\bar{z}(xx)z$; A₁'), $\underline{260}$ (2LA(M)), 360 (2E" (Γ) or A₁'+TA(M)), 373 (E'+LA(M)), 394 (3LA(M))	136 (A₁g-LA(M)), $\underline{248}$ ($\bar{z}(xy)z$; E₂g¹), $\underline{251}$ ($\bar{z}(xx)z, \bar{z}(xy)z$; A₁g), $\underline{260}$ (2LA(M)), 360 (2E₁g(Γ) or A₁g+TA(M)), 373 (E₂g¹+LA(M)), 394 (3LA(M))

3.2 Photoluminescence

Figure 3-10 shows a typical PL spectrum of monolayer MoS_2.The two peaks are located at 1.90 and 2.04 eV, respectively, which originate from the radiative recombination of the A and B excitons. The A and B excitons belong to the excitons in the two valleys of the valence band at the K and K' points, respectively. There is another kind of quasiparticle in 2D semiconductor TMDs, called trion, which is a combination state of either 2 electrons and 1 hole, or 2 holes and 1 electron, and therefore carries charge. The trion is denoted by A⁻ or A⁺, depending on the sign of the net charges on the quasiparticle. The peak with the lowest photon energy at 1.85 eV in Figure 3-10 is the A⁻ trion peak. Figure 3-11 shows schematically the energy band diagram of an exciton A, an exciton B and a trion A⁻. Due to the Coulumb interaction, the total energy one exciton holds is slightly smaller than the direct electronic band gap of the semiconductor (E_g); such an energy difference is identified with the energy binding energy, denoted by ε_A or ε_B. Similarly, the binding energy of a trion, denoted by ε_{A-} (ε_{A+}) is defined as the energy of an exciton and an electron (hole) when they are separated, and the net energy of a trion A⁻ (A⁺). Therefore, the quasiparticle energies E_A, E_B and $E_{A-/+}$ should be expressed as

$$E_A = E_g - \varepsilon_A \tag{3-3}$$

$$E_B = E_g + \Delta - \varepsilon_B \tag{3-4}$$

$$E_{A-/+} = E_g - \varepsilon_A - \varepsilon_{A-/+}$$

<div align="right">(3-5)</div>

where Δ is the valence band splitting.
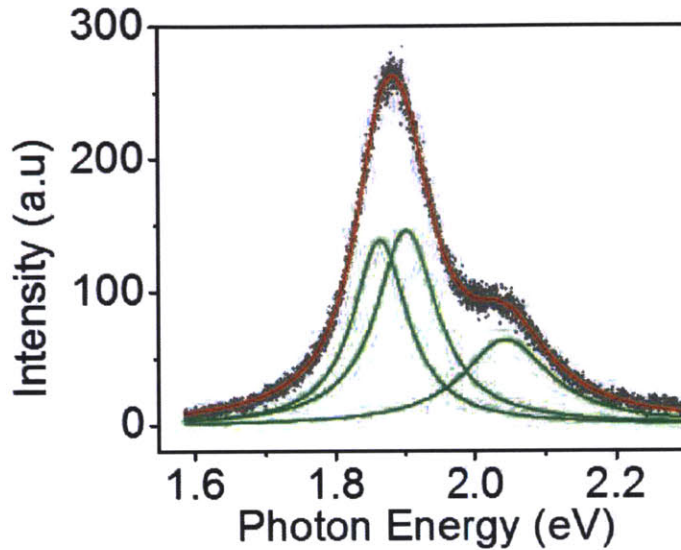
Figure 3-10 A typical PL spectrum of monolayer MoS_2. The grey dots are experimental data points, the green curves are three fitted Lorenzian function profiles and the red curve is the summation of the fitted functions.
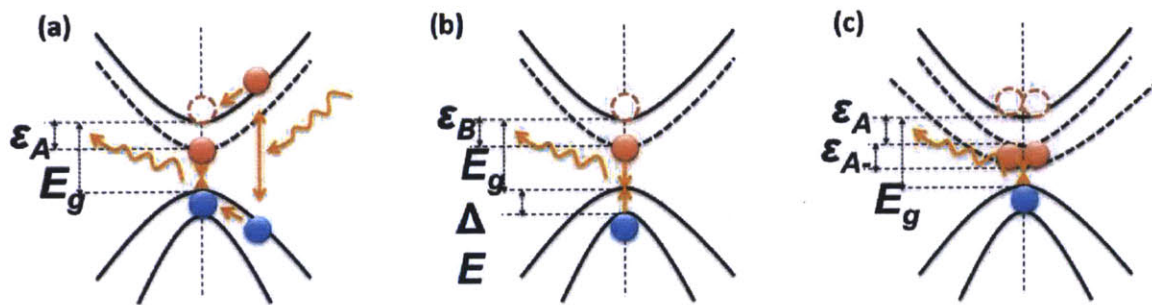
Figure 3-11 Schematics of the exciton-related radiative transitions, including (a) the A exciton, (b) the B exciton and (c) the A⁻ trion, at the K point in the Brillioun zone. Here E_g, Δ, ε_A, ε_B, ε_{A-} denote the band gap, valence band splitting, binding energy of the A, B exciton and A⁻ trion, respectively.

Figure 3-12 shows the typical PL spectra of CVD monolayer MoS_2, WS_2, $MoSe_2$ and WSe_2. The strongest PL peaks for these four materials are located at 670 nm, 633 nm, 808 nm and 760 nm, respectively. Figure 3-13 shows the optical images and corresponding PL mappings of the triangular domains of these four TMD monolayers. There are two optical transitions in these four materials, which are related to the A and B excitons, respectively. Table 3-5 shows the transition energies of the A and B excitons for the four TMDs in monolayer forms, obtained by PL or optical absorption measurements.
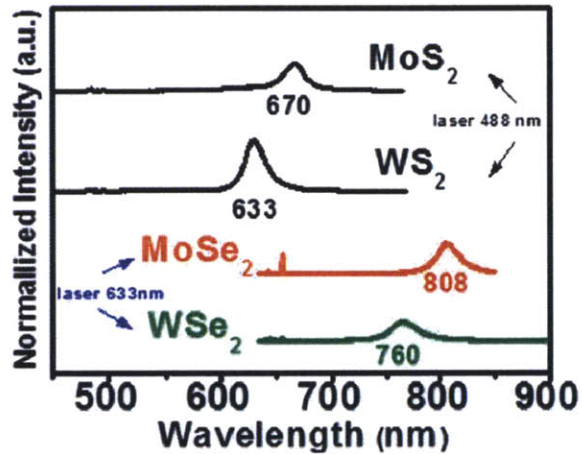
Figure 3-12 Photoluminescence spectra of monolayer MoS_2, WS_2, $MoSe_2$ and WSe_2 samples synthesized by chemical vapor deposition under the indicated laser excitation wavelengths.
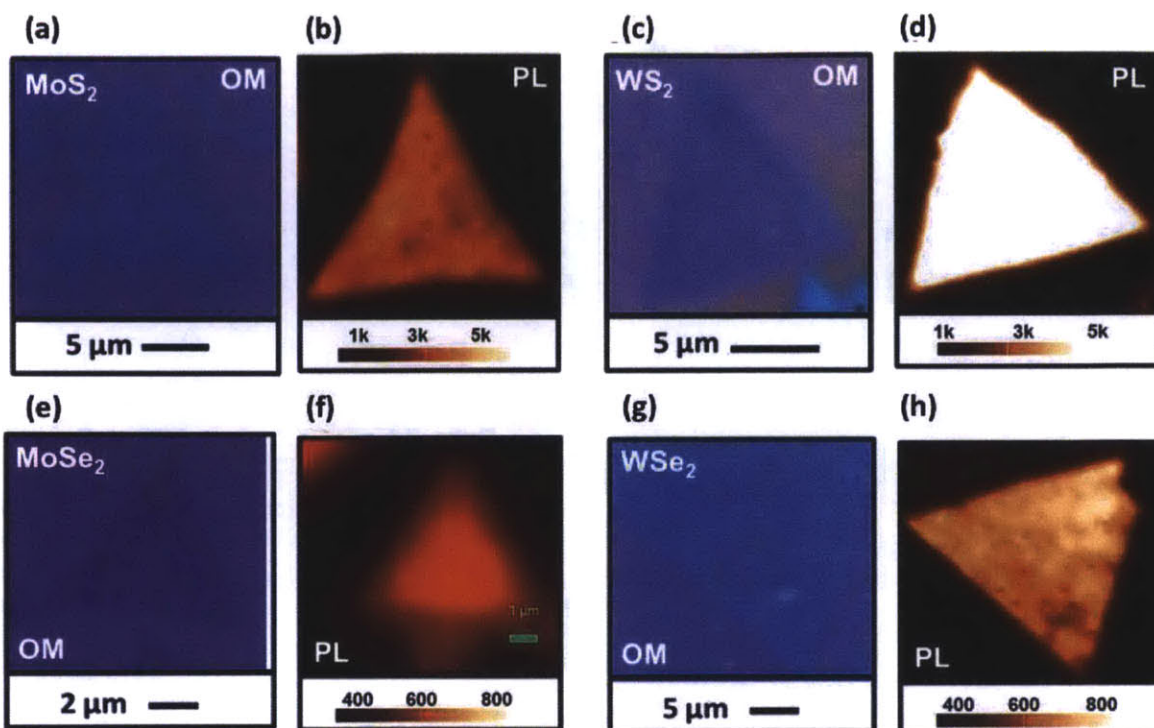
Figure 3-13 Photoluminescence mapping of monolayer (b) MoS$_2$, (d) WS$_2$, (f) MoSe$_2$ and (h) WSe$_2$ triangular domains synthesized by chemical vapor deposition. (a)(c)(e)(g) are optical images of the same domains.

Table 3-5 Optical transition energies of A and B excitons in monolayer MoS$_2$, WS$_2$, MoSe$_2$ and WSe$_2$. [88,89,153-155,156,215,216]

Material	A exciton	B exciton
MoS$_2$	1.88 eV (660 nm)	2.04 eV (608 nm)
WS$_2$	1.98 eV (625 nm)	2.4 eV (520 nm)
MoSe$_2$	1.66 eV (750 nm)	1.85 eV (670 nm)
WSe$_2$	1.65 eV (750 nm)	2.08 eV (600 nm)

3.3 Absorption
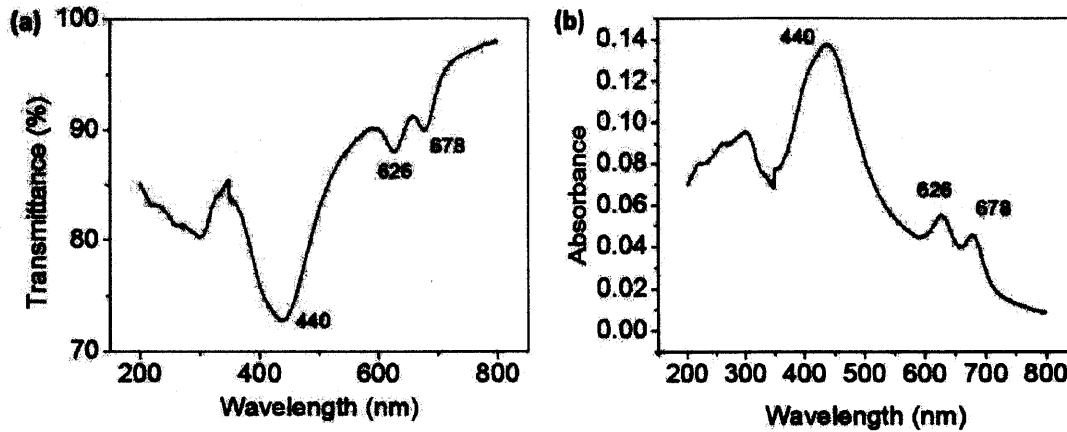
Figure 3-14 (a) Transmittance and (b) absorbance of CVD monolayer MoS₂.

Similar to the PL spectra in Figure 3-12, the exciton peaks of 2D TMDs can be also observed at room temperature from optical absorption spectra. As shown in Figure 3-14, there are three clear absorption peaks in the absorption spectrum of CVD monolayer MoS₂, located at 440 nm, 626 nm and 678 nm, respectively. The peaks at 678 nm and 626 nm are close to the optical band edge of monolayer MoS₂, and these peaks are identified with the radiative recombination of the A and B exciton, respectively. The origin of the peak at 440 nm remains unclear, but some groups believe that this is because of the parallel conduction and valence band around the Γ point in the Brillioun zone which gives rise to a large joint density of states [217].

Chapter 4. Optical Properties of Monolayer MoS$_2$ with Different Carrier Densities

One of the fundamental problems we need to figure out in any studies of 2D TMDs is how the electrical and optical properties change with the Fermi level of the materials. This Chapter is focused on the influence of the Fermi level, or carrier densities, on the optical properties of monolayer MoS$_2$.

The Fermi level of MoS$_2$ can be controlled by electrical gating technique. Electrochemical gating was used in order to tune the Fermi level with higher efficiency, following the work done on graphene [218-223] and organic materials [224]. In the following, the polymer-electrolyte gating technology is introduced after which a comparison is made between the electronic performance of a polymer-electrolyte gate and that of the commonly used 300 nm SiO$_2$ back gate. Raman spectroscopy results show that the A$_{1g}$ vibrational mode is very sensitive to the carrier density, whereas E$_{2g}^1$ mode remains almost the same when the gate bias is changed. The correlation between the photoluminescence of monolayer MoS$_2$ and its carrier density is also observed. Finally, the mechanism behind our observations is studied.

4.1 Electrochemical Gating Technology

If an electric field is applied throughout a metal-oxide-semiconductor (MOS) structure, free or fixed charges will accumulate at the interface between the oxide and the semiconductor; such charges can effectively "dope" the semiconductor in the region near the interface, and thus shifting the Fermi level of the semiconductor. This effect has been commonly used in electronic and optoelectronic devices to tune the conductivity as well as the electrical barrier in the devices. In conventional MOS structures, the capacity of storing charges is mainly determined by the density of the dipoles formed within the oxide. If we replace the dielectrics by electrolytes, the mobile ions with specific electric charges within the electrolytes can migrate along electric field lines and accumulate at the boundaries of the electrolytes. This process is very similar to the polarization of dipoles in dielectrics, but with more freedom. Therefore, the field effect based on the ionization of the electrolyte in metal-electrolyte-semiconductor (MES) structure should be more efficient than that based on the polarization of the dielectric in a MOS structure.

Recently, researchers have used the electrolyte-based gating technique to tune the Fermi level of thin film materials, such as graphene and organic thin films [218-224]. Following their technique, we fabricated polymer electrolyte-gated MoS_2 in order to investigate its optical properties as a function of the carrier density. In this section, a description of the device structure together with the fabrication process will be provided, followed by a brief discussion of the mechanisms associated with the electrochemical gating.

4.1.1 Device Fabrication

The schematics of the device structures are shown in Figure 4-1. There are two kinds of devices in this design: the three terminal devices are for transport measurements with the source and drain electrodes connected to the MoS_2 channels, and the side-gate electrode isolated from MoS_2; and the two-terminal devices for Raman spectroscopy and PL measurements, with only one electrode contacting the channel and the other electrode isolated as the side-gate. We started with a continuous monolayer of MoS_2 synthesized by chemical vapor deposition on 300nm SiO_2/Si substrates. E-beam lithography (EBL) with poly(methyl methacrylate) (PMMA) as the resist, and E-beam evaporation with the lift-off process were used to define the source/drain and gate electrodes. The metal contacts here are 5 nm Ti/50 nm Au. Then another EBL was done to define the isolation patterns of the MoS_2 channels, followed by the reactive-ion etching (RIE) with oxygen plasma to etch away the unwanted MoS_2. Finally, the polymer electrolyte was drop-coated onto the substrates with hot-plate heating (90 °C). The polymer electrolyte is composed of poly(ethylene oxide) (PEO) and caesium perchlorate ($CsClO_4$), which are dissolved in methanol. Their ratio by weight is PEO:$CsClO_4$=8:1. Figure 4-2 shows the optical images of the final devices, and Figure 4-3 summarizes the fabrication process.
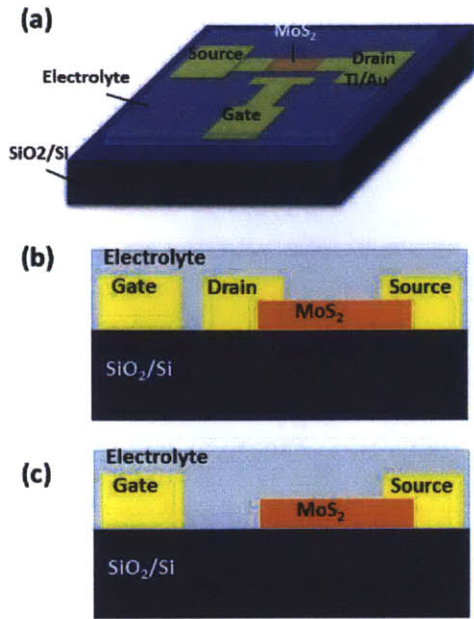
Figure 4-1 (a) Schematic of the device structure and the side views of (b) three-terminal and (c) two-terminal devices.
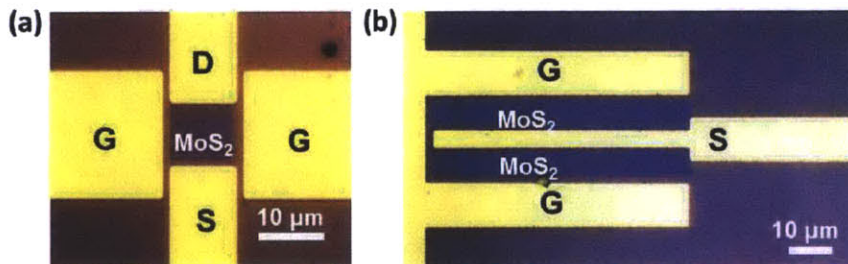
Figure 4-2 Microscopic images of (a) three-terminal and (b) two-terminal devices, corresponding, respectively, to Figure 4-1(b) and (c).
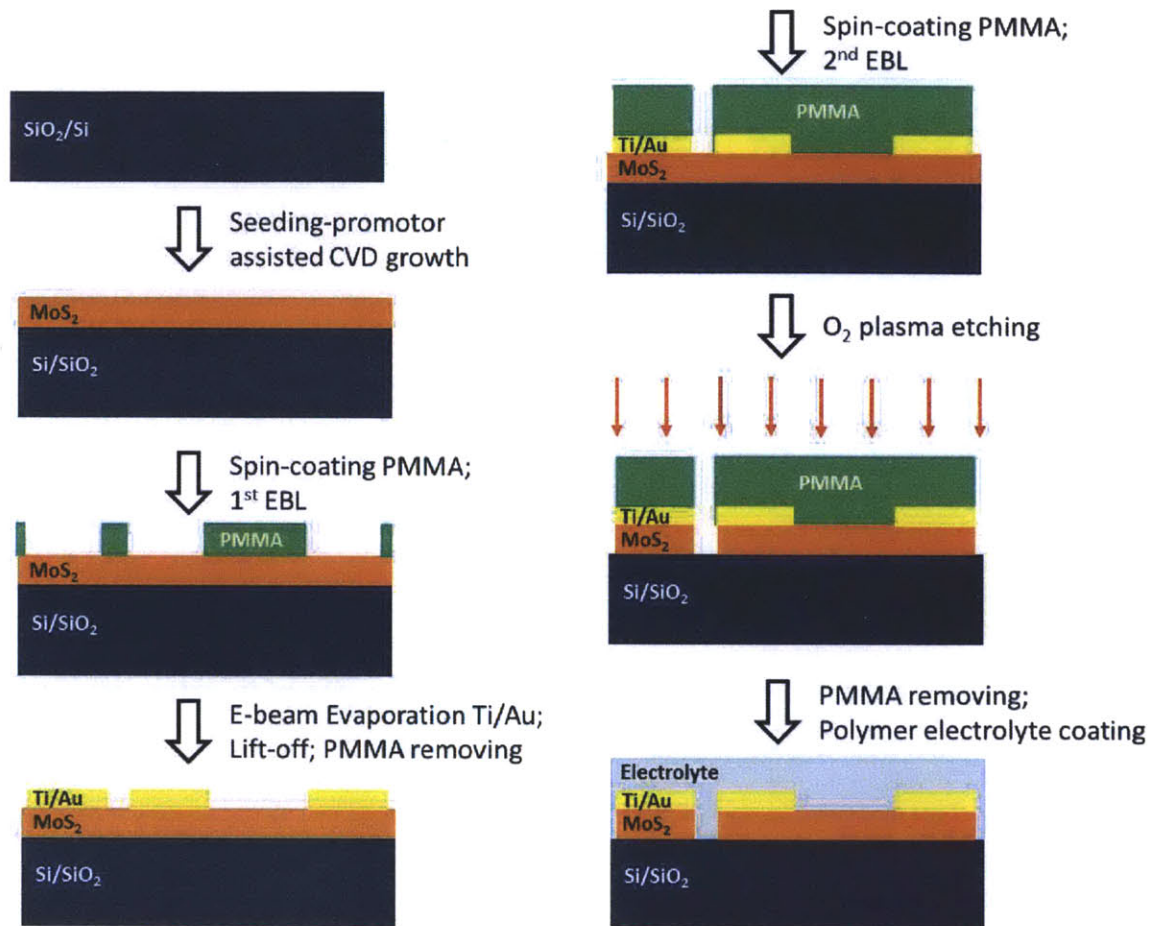
Figure 4-3 Schematic of the fabrication process of polymer-gated MoS$_2$ devices.

4.1.2 Mechanism

Figure 4-4 illustrates the charge migration and distribution of the electrolyte-gated MoS$_2$ with specific electric fields. Driven by an external electric field, the Cs$^+$ and ClO$_4^-$ ions will migrate in the electrolyte, and accumulate at the interfaces either between the electrolyte and the semiconductor, or between the electrolyte and the metal electrode; electrons and holes around the interface within the semiconductor will be accumulated or depleted, accordingly, to neutralize the net charges at the interface; as a result, an electric double layer (EDL) is formed at the electrolyte-semiconductor interface, generating a strong capacitor and a large charge density. The EDL capacitance per unit area can be expressed as

$$C_{EDL} = \frac{\kappa_{EDL}\varepsilon_0}{d_{EDL}} \tag{4-1}$$

where κ_{EDL} and d_{EDL} are the effective relative dielectric constant and effective thickness of the EDL, respectively, and ε_0 is the vacuum permittivity. For the simplest approximation, d_{EDL} is equal to the diameter of the ions accumulated at the surface of the channels; therefore, d_{EDL} can be as small as ~1 nm, which means the EDL capacitance can be two orders of magnitude larger than the commonly used 300 nm SiO_2/Si capacitance.
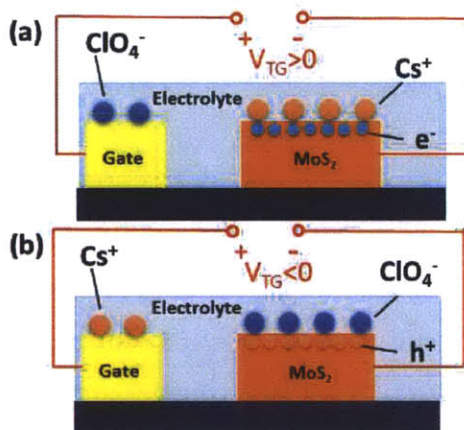
Figure 4-4 Schematics of the ion migrations and electric double layer formations when the gate voltage is (a) positive (electrons are accumulated in the MoS_2 channel, and Cs^+ ions are accumulated in the electrolyte near the channel) and (b) negative (holes are accumulated in the MoS_2 channel, and ClO_4^- ions are accumulated in the electrolyte near the channel).

4.2 Electrical Measurements
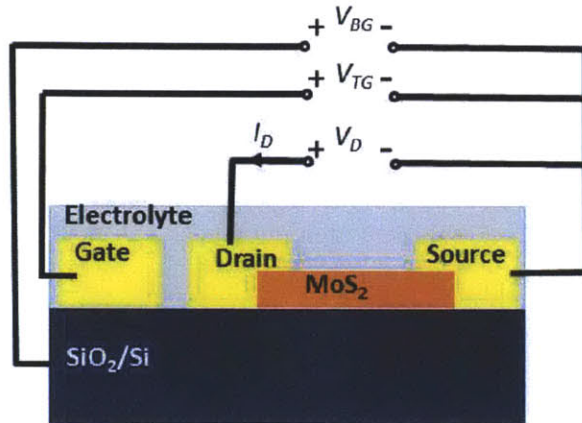
Figure 4-5 Schematics of the electrical connections.

The three-terminal devices (Figure 4-1(b) and Figure 4-2(a)) were used for electrical measurements. Figure 4-5 shows the configurations of the electrical connections in the measurements. The two electrodes connected with the MoS_2 channel, labeled source and drain, are grounded and biased with voltage V_D, respectively. Two gate voltages are applied on the device and compared with each other: the back-gate voltage (V_{BG}), applied by the Si substrate, and the top-gate voltage (V_{TG}), applied by the side gate electrode with the polymer electrolyte. Figure 4-6 and Figure 4-7 show transport measurement results for the back-gated and top-gated devices, respectively. The back-gated characteristics were made before the polymer electrolyte was deposited onto the sample. The source-drain current (I_D) of the top-gated device is much larger than that of the back-gated device. The field-effect mobility can be calculated by

$$\mu = \frac{L}{WC_GV_D}\frac{dI_D}{dV_G} \qquad (4\text{-}2)$$

where L and W are the channel length and channel width of the transistor, respectively; Here C is the gate capacitance, which is estimated to be ~10 nF for the SiO_2/Si back-gate, and ~1 µF for the electrolyte gate, respectively. The derivative in Eq. (4-2) should be the maximum slope in the transfer characteristics. From this linear fitting with maximum

slope, we can also extract the threshold voltage (V_{TH}) from the intersection between the fitted line and the x-axis. The carrier density (n) is given by

$$n = C_G(V_G - V_{TH})$$ (4-3)
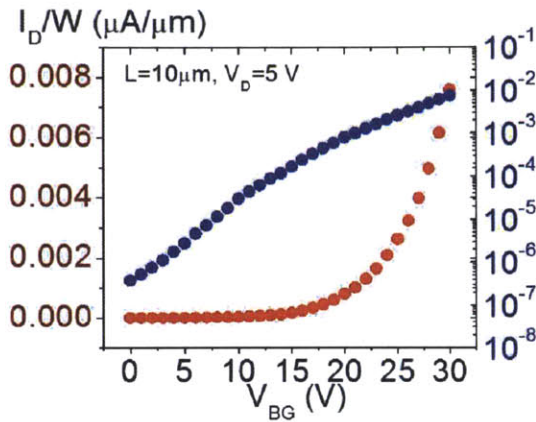
Figure 4-6 Transfer characteristics of the back-gated transistors before coating the PEO-based electrolyte. The red dots with the left axis are in linear scale, and the blue dots with the right axis are in log scale.
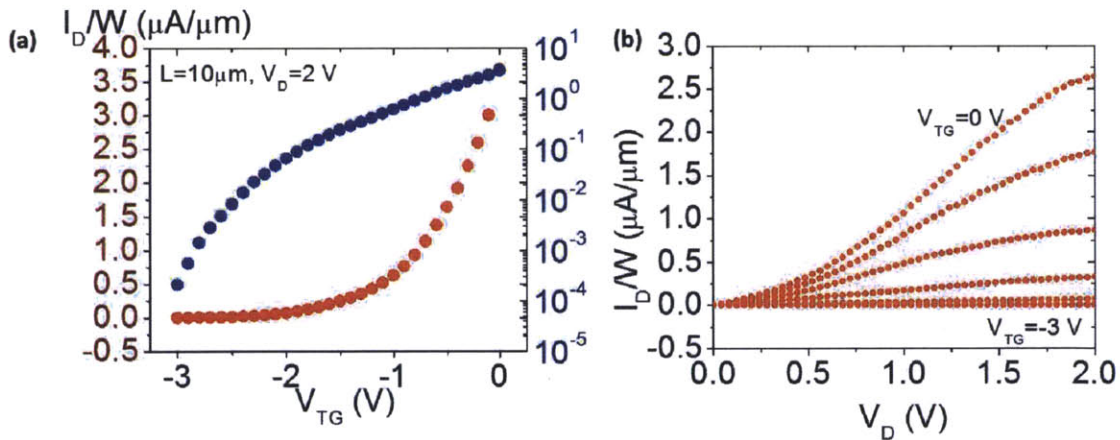
Figure 4-7 (a) Transfer and (b) output characteristics of the top-gated transistors after coating the PEO-based electrolyte. In (a), the red dots with the left axis are in linear scale, and the blue dots with the right axis are in log scale. The multiple curves in (b) are with different top-gate voltage (V_{TG}) in the range of 0 to -3 V with the interval of -0.6 V.

Table 4-1 summarizes the extracted values of the parameters in both the back-gated measurements and the top-gated measurements. V_{TH} is positive for the back-gated device

before coating the polymer electrolyte, whereas it becomes negative after the coating of the polymer electrolyte. This means there is an n-doping effect on the MoS_2 transistors when polymer electrolyte is deposited onto the channel and the mobility increases from 0.11 ± 0.08 $cm^2/V\cdot s$ to 21 ± 12 $cm^2/V\cdot s$ after depositing the polymer electrolyte. There are two possible explanations for this prominent mobility improvement: (1) the electrolyte gate is able to provide higher carrier density of the channel than does the back gate, and thus gives a larger value of the mobility; (2) the higher dielectric constant of the polymer electrolyte attenuates the populations of the optical phonons and screens the impurity charges at the interfaces, both of which may degrade the mobility by a large amount. Figure 4-8 plots the current density as the function of the carrier densities with the SiO_2/Si back-gated measurements and top-gated measurements. The relationship between the current density and the carrier density in the MoS_2 channel should follow

$$J = q(n\mu_n + p\mu_p) \approx qn\mu_n \qquad (4\text{-}4)$$

where J is the current density; n and p are the electron and hole carrier densities, respectively; μ_n and μ_p are electron and hole mobility. Because the MoS_2 we used here is n-type, the hole current can be ignored. The dashed lines in Figure 4-8 are the fitting results according to Eq. (4-4). The current density of the electrolyte-gated device is one order of magnitude higher than that of the SiO_2/Si back-gated device, even when we compare them at the same carrier density. This means that both the effect of higher carrier density and the screening effect of high-K dielectrics help to improve the mobility of MoS_2 transistors.

Table 4-1 A comparison between the 300 nm SiO_2 back gate and the PEO-based top gate MoS_2 devices.

Parameter	300 nm SiO_2 back gate	PEO-based top gate
Effective thickness	300 nm	~1 nm
Relative dielectric constant	2.9	5
Gate capacitance	11.5 nF/cm^2	~1 $\mu F/cm^2$
Max. gate voltage	50 V	5 V
Max. carrier density	3.6×10^{12} cm^{-2}	~3.2×10^{13} cm^{-2}
Mobility	0.11 ± 0.08 $cm^2/V\cdot s$	21 ± 12 $cm^2/V\cdot s$
Threshold voltage	22.5 ± 1.3 V	-2.0 ± 0.4 V
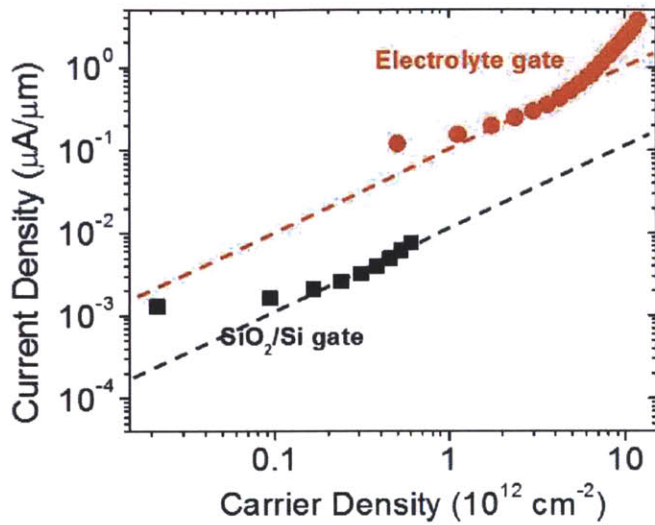
Figure 4-8 The current density of the SiO_2/Si gate device (black dots) and the polymer electrolyte gate device (red dots) as a function of the carrier density. Dashed lines are fitting results to Eq. 3-4 of the experimental points.

4.3 Optical Measurements

4.3.1 Experimental setup

Figure 4-9 shows a schematic of the experimental setup of the spectroscopy measurement with electronics. A confocal Raman spectroscopy system was used with the excitation laser of 532 nm. The devices were on a Si substrate, and wire-bonded onto a chip carrier which was mounted on a homemade electronic board. A gate voltage was applied on the source and side gate electrode by a voltage source. The optical images of the experimental setup are shown in Figure 4-10.
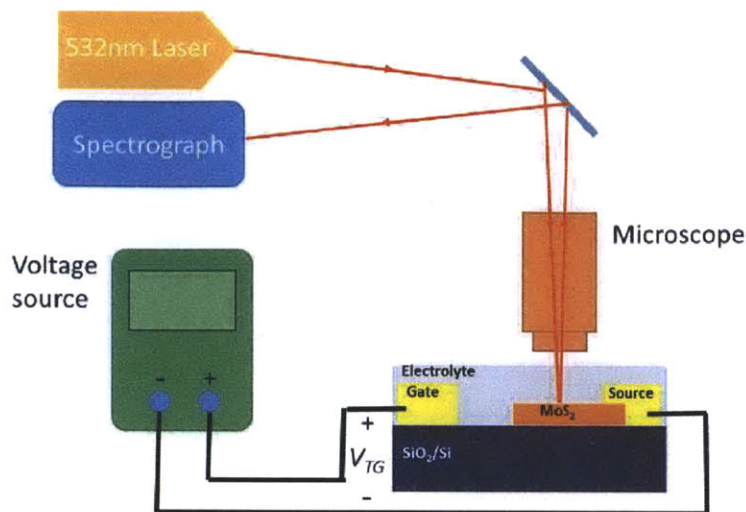
Figure 4-9 Schematic of the experimental setup.
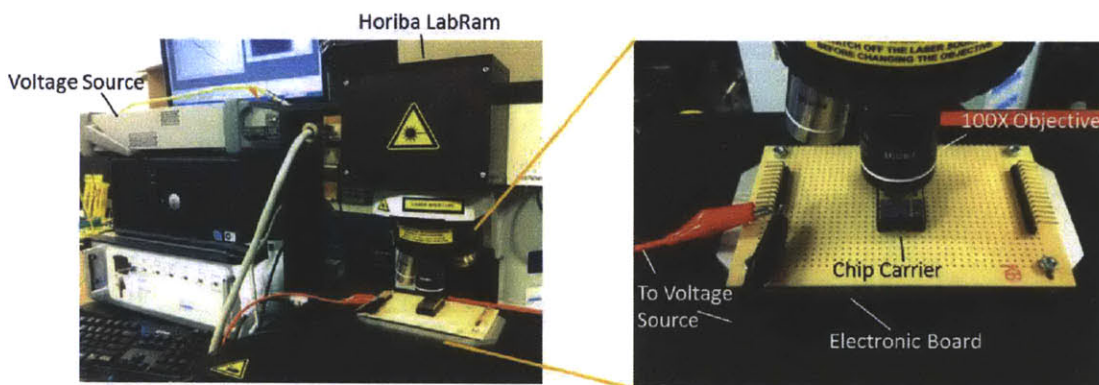
Figure 4-10 Optical images of the experimental setup corresponding to Figure 3-9.

4.3.2 Raman Spectroscopy

The Raman spectra of the monolayer MoS_2 as a function of the gate voltage applied through the polymer electrolyte are shown in Figure 4-11. As mentioned in Chapter 2, the Raman peaks located at around 385 cm^{-1} and 403 cm^{-1} correspond to the E_{2g}^1 and A_{1g} vibrational modes, respectively. The E_{2g}^1 mode is an in-plane vibrational mode with the S and Mo atoms moving in opposite directions, whereas the A_{1g} mode is an out-of-plane vibrational mode with the two S atoms in the primitive unit cell moving in opposite

56

directions, and the Mo atom remains fixed. The peak at 520 cm^{-1} is from the silicon substrate.
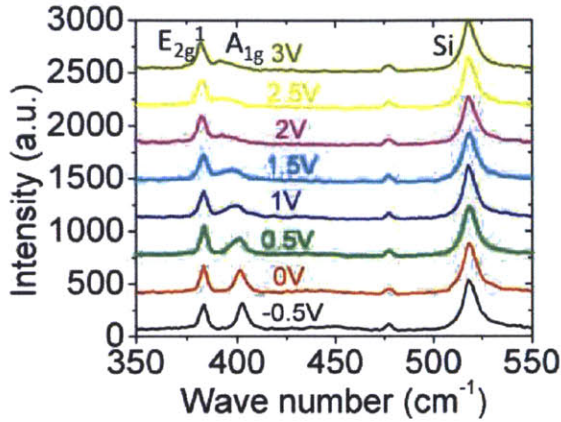
Figure 4-11 Gate-voltage dependent Raman spectra for a monolayer MoS$_2$ sample.

The Raman peaks in Figure 4-11 can be fitted with Lorentzian functions. Based on the fitting, Figure 4-12 plots the frequency positions, intensities and full widths at half maximum (FWHM) of the E$_{2g}^1$ and A$_{1g}$ peaks with respect to the applied electrolyte-gate voltage. The carrier density (tope scale) is also shown along with the gate voltage (bottom scale) on the x axis, calculated from Eq. (4-3). It is observed that at high carrier density, the A$_{1g}$ mode softens from 403 cm^{-1} to 393 cm^{-1}, and broadens from 5 cm^{-1} to 15 cm^{-1}. The intensity of the A$_{1g}$ mode is also attenuated by the high carrier density. However, the E$_{2g}^1$ mode remains almost the same. According to DFT calculations [225], the electronic states at the bottom of the conduction band near the K point correspond to the d_{z^2} orbital of Mo, and the electronic states around the valence band maximum are associated with the d_{xy} character. The symmetries of these orbitals lead to non-zero values of most of the matrix elements of the electron-phonon coupling terms for the A$_{1g}$ mode, but near-zero values for the corresponding matrix elements for the E$_{2g}^1$ mode

57

[225]. We can use either the position difference in frequency between the A_{1g} and E_{2g}^1 modes, or the intensity ratio between them to easily identify the doping concentration or Fermi level of monolayer MoS_2.
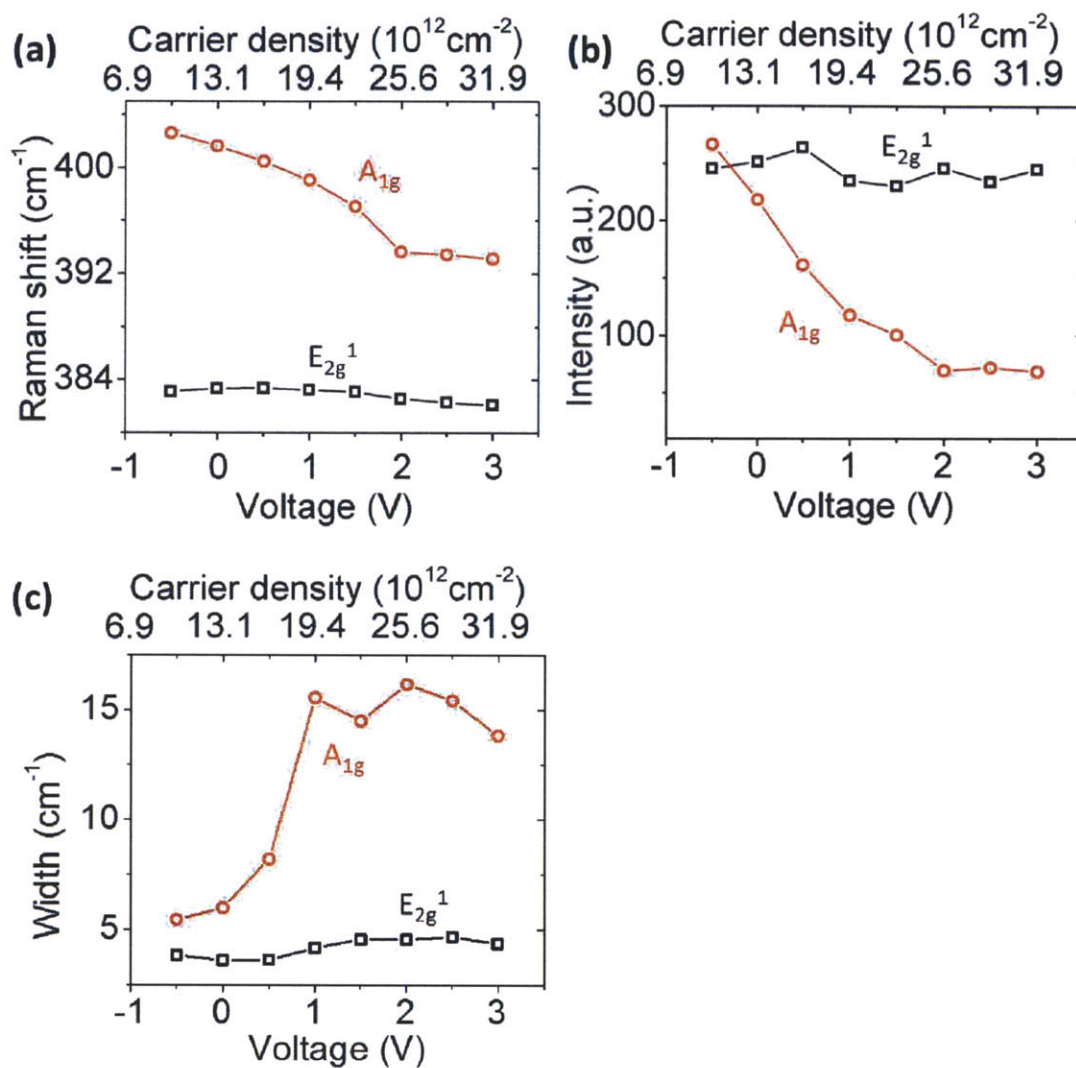
Figure 4-12 Gate-voltage dependent (a) Raman shift, (b) intensity and (c) line width of the A_{1g} and E_{2g}^1 modes in monolayer MoS_2.

4.3.3 Photoluminescence

The photoluminescence spectra with different electrolyte-gate voltages from -3.0 V to 3.0 V with an interval of 0.3 V between them are shown in Figure 4-13. As the PL signals in Figure 4-13(a) at positive gate voltage become very weak, we plot them in a separate,

panel as shown in Figure 4-13 (b). Each PL spectrum can be fitted with three Lorentzian functions, which are assigned to be A⁻ trion, A exciton and B exciton, respectively, as mentioned in Figure 3-10 of Chapter 3.
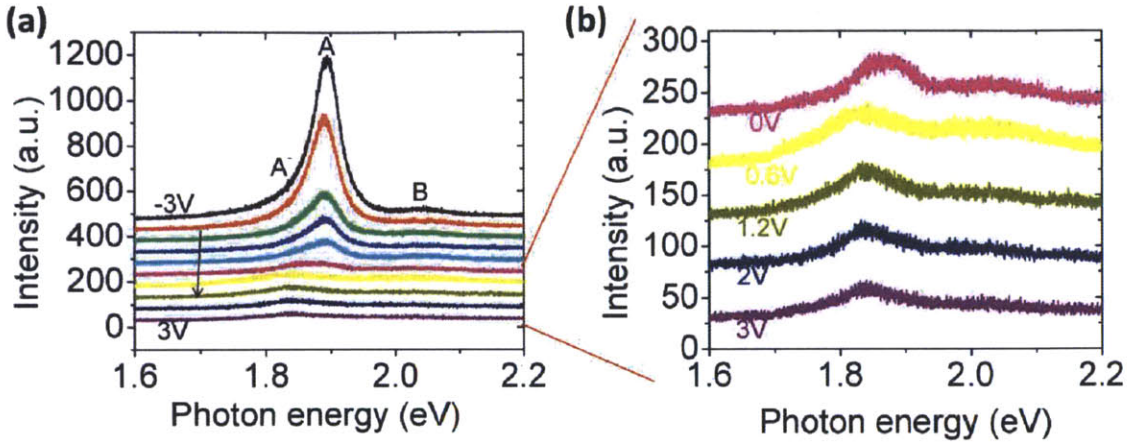
Figure 4-13 Photoluminescence spectra of monolayer MoS₂ with different gate voltages applied by the polymer electrolyte gate. Panel (b) shows zoom-in plots of the positive voltage spectra shown in panel (a).

The fitted peak energies, and peak intensities as a function of the gate voltage for the A⁻ trion and A and B excitons are shown in Figure 4-14. It is observed that the peak frequencies decrease with increasing gate voltage, by up to 300 meV. The peak intensities decay exponentially as well, with the A exciton peak decaying much faster than the A⁻ trion and the B exciton peaks.

The transition between excitons and trions can be regarded as a chemical reaction, given by

$$A + e^- \rightarrow A^- \tag{4-6}$$

According to the mass action law, the relation among the equilibrium densities of the electron (n_e), exciton A (N_A) and trion A⁻ (N_{A-}) is given by [154,226]

$$\frac{N_A n_e}{N_{A-}} = \frac{4 m_A m_e k_B T}{\pi \hbar^2 m_{A-}} \exp\left(-\frac{\varepsilon_{A-}}{k_B T}\right) \tag{4-7}$$

59

where k_BT=25.9 meV is the thermal energy at room temperature (300K), ε_{A-} is the trion binding energy, m_A=m_e+m_h is the total mass of the exciton A, m_{A-}=$2m_e$+m_h is the total mass of trion A$^-$, and m_e=$0.35m_0$ and m_h=$0.45m_0$ are, respectively, the electron and hole effective masses of monolayer MoS$_2$ near the K point in the Brillioun zone.

The PL intensity ratio of the A$^-$ trions and of the A$^-$ trions plus A excitons can be expressed by

$$\frac{I(A^-)}{I(A^-)+I(A)}=\frac{\Gamma_{A-}N_{A-}}{\Gamma_{A-}N_{A-}+\Gamma_A N_A} \tag{4-8}$$

with the radiative recombination rates Γ_{A-} and Γ_A for the A$^-$ trion and A exciton. For simplicity, we assumed these parameters are constants for the different carrier densities. Therefore, the intensity ratio can be expressed as

$$\frac{I(A^-)}{I(A^-)+I(A)}=\frac{1}{1+\dfrac{\Gamma_A N_A}{\Gamma_{A-}N_{A-}}}=\frac{1}{1+\dfrac{K}{n_e}} \tag{4-9}$$

where K is a fitting parameter. Figure 4-15 shows the fitting results based on Eq. (4-9) in comparison with the experimental data. We can see the simple mass action model can resemble the experimental results very well.
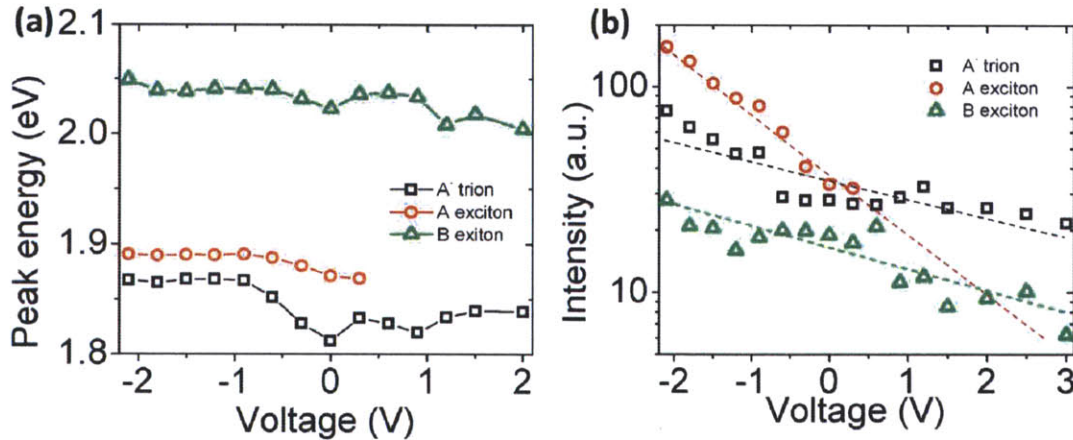
Figure 4-14 Gate-voltage dependent (a) peak frequencies and (b) intensities of the PL spectra of the monolayer MoS$_2$ at room temperature.
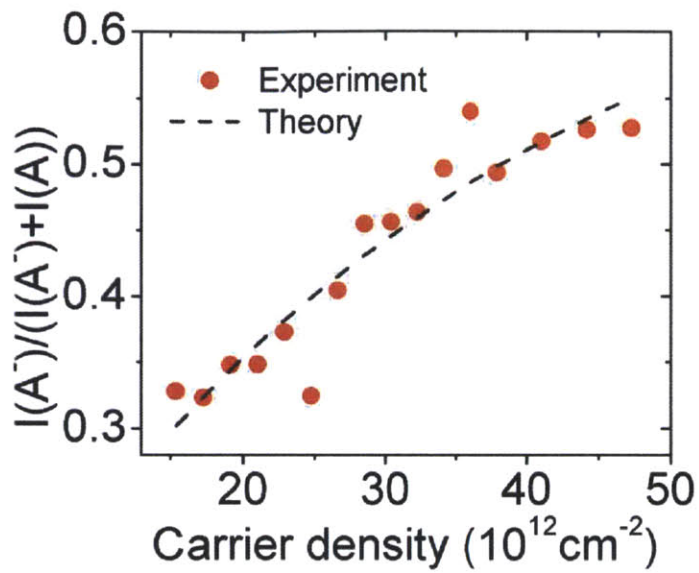
Figure 4-15 Experimental data (red dots) and fitting curve (black dashed line) of the PL intensity proportion of A⁻ trion as a function of the carrier density (see text).

Chapter 5. Optical Properties of Monolayer MoS_2 with Different Surrounding Dielectrics

Environmental dielectrics have been found to strongly influence both the electrical and optical properties of low dimensional materials, including quantum wells, carbon nanotubes, graphene, etc [227-232]. However, such study on LTMDs is still at an early stage [233-241]. Several groups have studied the mobility enhancement effect of MoS_2 field effect transistors by introducing a gate oxide with higher dielectric constants [233-235], and they have explained this enhancement as the screening of long-range Coulomb interactions induced by impurity charges. In terms of the optical properties, several groups studied the Raman and PL spectra of atomicly thin MoS_2 layers on various solid substrates [237-241], and they attributed the shift of the PL peaks to either doping or strain that is induced by the dielectric or metallic substrates. In those systems, however, the effect of dielectric screening on the exciton-related optical transitions was not considered.

In this chapter, the intrinsic influence of the dielectric constant of the environments on the exciton behaviors of monolayer MoS_2 is investigated. To prevent the doping or strain effect that may be induced by the fabrication process or the lattice mismatch between MoS_2 and the dielectrics, we use non-ionic organic solvents as the environmental dielectrics [234-236]. We here discuss the evolution of the PL spectra as a function of the external dielectric constant. Based on the experimental results, a theoretical model is developed to describe how the binding energies of excitons and trions as well as the electronic quasiparticle band gap change with the effective dielectric constant of the quantum-confined 2D system. The population ratio of excitons and trions is also analyzed with the mass action model. This effect provides a simple method to generate excitons and trions separately and selectively, which paves the way to studying the behaviors of excitons and trions independently, and for potentially realizing well-controlled excitonic interconnects [242] and high-efficiency valleytronics [158-161].

5.1 Solvent Immersion Technology

5.1.1 Device Structure and Experimental Setup

Figure 5-1 shows a schematic diagram of the device. Continuous monolayer MoS_2 was grown on 300nm SiO_2/Si substrates by chemical vapor deposition (CVD) The optical microscopic image of the MoS_2-on-SiO_2 sample is shown in Figure 5-2(a). The atomic force microscopic (AFM) image shown in Figure 5-2(b) indicates that the surface of the as-grown MoS_2 is smooth and clean, and the height profile (inset) along the dotted line in the AFM image, confirms that the MoS_2 is a monolayer, with a thickness of around 0.7 nm. For each spectroscopy measurement, the MoS_2/SiO_2/Si sample was loaded into a quartz cell filled with one of the organic solvents. The spectroscopy measurements were taken on a confocal microscopic setup with the excitation laser wavelength of 532.5nm. Since the samples were successively immersed in different solvents during the measurement, it is necessary to check the quality of the MoS_2 after each solvent-immersed measurement. In order to do this, after each spectroscopy measurement of the MoS_2 sample in one of these solvents, the sample was taken out and rinsed with acetone and isopropyl alcohol, and another measurement was carried out on the sample in air. The PL peak positions of the sample exposed to air did not change much before and after the sample was in contact with any of the solvents, as shown in Figure 5-3, indicating that neither the chemical reactions nor physical attachments changed the excitonic properties of MoS_2 when immersed in the solvents. Since the PL and Raman spectra vary with the position of the laser beam spot on the sample, we took the average of 5-10 spectra collected with different beam positions throughout the sample for each dielectric configuration.
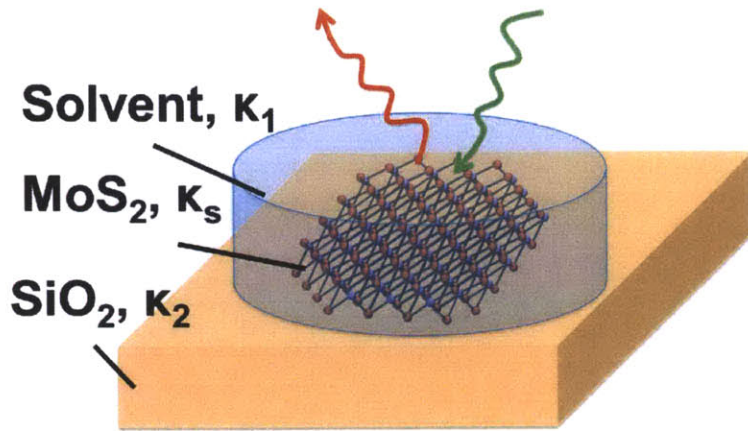
Figure 5-1 Schematic of the experimental setup. The CVD MoS₂ sample is on a SiO₂/Si substrate, and immersed in a specific organic, non-ionic solvent. The relative dielectric constants of the MoS₂, the solvent and the substrate layer are denoted by κ_s, κ_1, and κ_2, respectively.
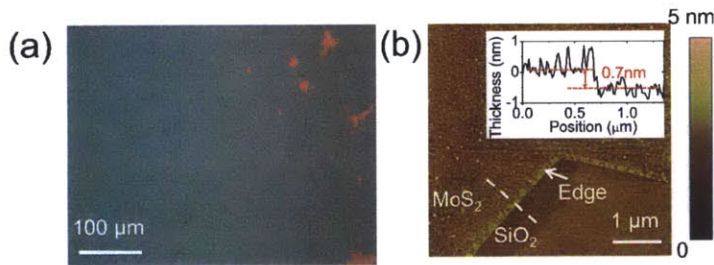
Figure 5-2 (a) Optical microscopic image of CVD MoS₂ grown on an SiO₂/Si substrate. (b) AFM image of CVD MoS₂ grown on a SiO₂/Si substrate. The inset is the height profile plotted along the white dashed line in the main figure. The step height, or the thickness of the MoS₂, is around 0.7 nm, indicating that the MoS₂ sample is monolayer.
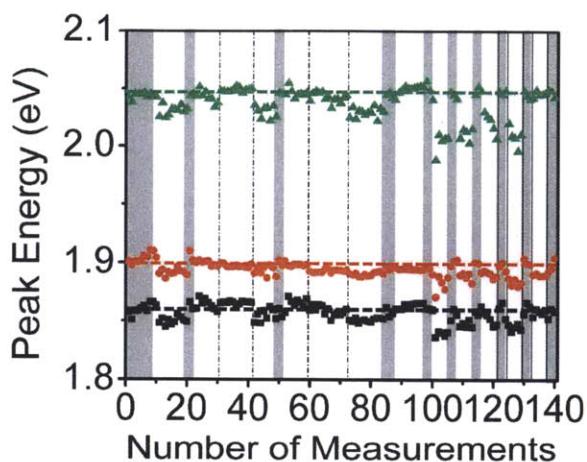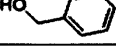
Figure 5-3 Time-sequence PL peak energies. The black, red and green dots are the peak positions of the A⁻ trion, and the A and B excitons, respectively. The gray regions are PL measurements of monolayer MoS_2 in air, and the white regions are PL measurements in specific solvents. The dotted lines indicate the average peak positions in air. The peak energies in the grey regions do not change much, which means the sample is not contaminated by exposure to previous solvents.

5.1.2 Basic properties of the solvents

In order to provide a stable, pure dielectric environment that does not affect the MoS_2 in any other aspects (doping, strain, chemical functionalization, etc.), we chose non-ionic organic solvents as the external dielectrics. The solvents include hexanes (κ_I=1.89), benzene (κ_I=2.28), toluene (κ_I=2.38), anisole (κ_I=4.33), benzyl alcohol (κ_I=13), isopropyl alcohol (κ_I=18.3), 2-butanone (κ_I=18.5), acetone (κ_I=20.7), ethanol (κ_I=24.6) and methanol (κ_I=32.6). Additional properties of these solvents can be found in Table 5-1.

Table 5-1 Basic Physical Properties of the Organic Solvents Used in the Experiment [243]

Solvent Name	Chemical Formula	Static Dielectric Constant	Refractive Index (Visible range)	High-freq. Dielectric Constant	Relative Polarity	Density (g/mL)	Boiling Point (°C)	Melting Point (°C)
Air/Vacuum	--	1	1	1	--	--	--	--
Hexanes		1.89	1.375	1.89	0.009	0.655	69	-95
Benzene		2.28	1.501	2.25	0.111	0.879	80.1	5.5
Toluene		2.38	1.497	2.24	0.099	0.867	110.6	-93
Anisole		4.33	1.516	2.30	0.198	0.996	153.7	-37.5
Benzyl Alcohol		13	1.54	2.37	0.608	1.042	205.4	-15.3
Isopropyl Alcohol		18.3	1.378	1.90	0.546	0.785	82.4	-88.5
2-Butanone		18.5	1.379	1.90	0.506	0.808	99.5	-114.7
Acetone		20.7	1.359	1.85	0.355	0.786	56.2	-94.3
Ethanol		24.6	1.361	1.85	0.654	0.789	78.5	-114.1
Methanol	HO—	32.6	1.328	1.76	0.762	0.791	64.6	-98

The Raman spectra of the solvents we used in the experiment are summarized in Figure 5-4. In the following measurements on real MoS_2 samples, we can observe the signals from the solvents as well. The signals from the signals are beyond the considerations of the topic of the thesis, and will thus be ignored.
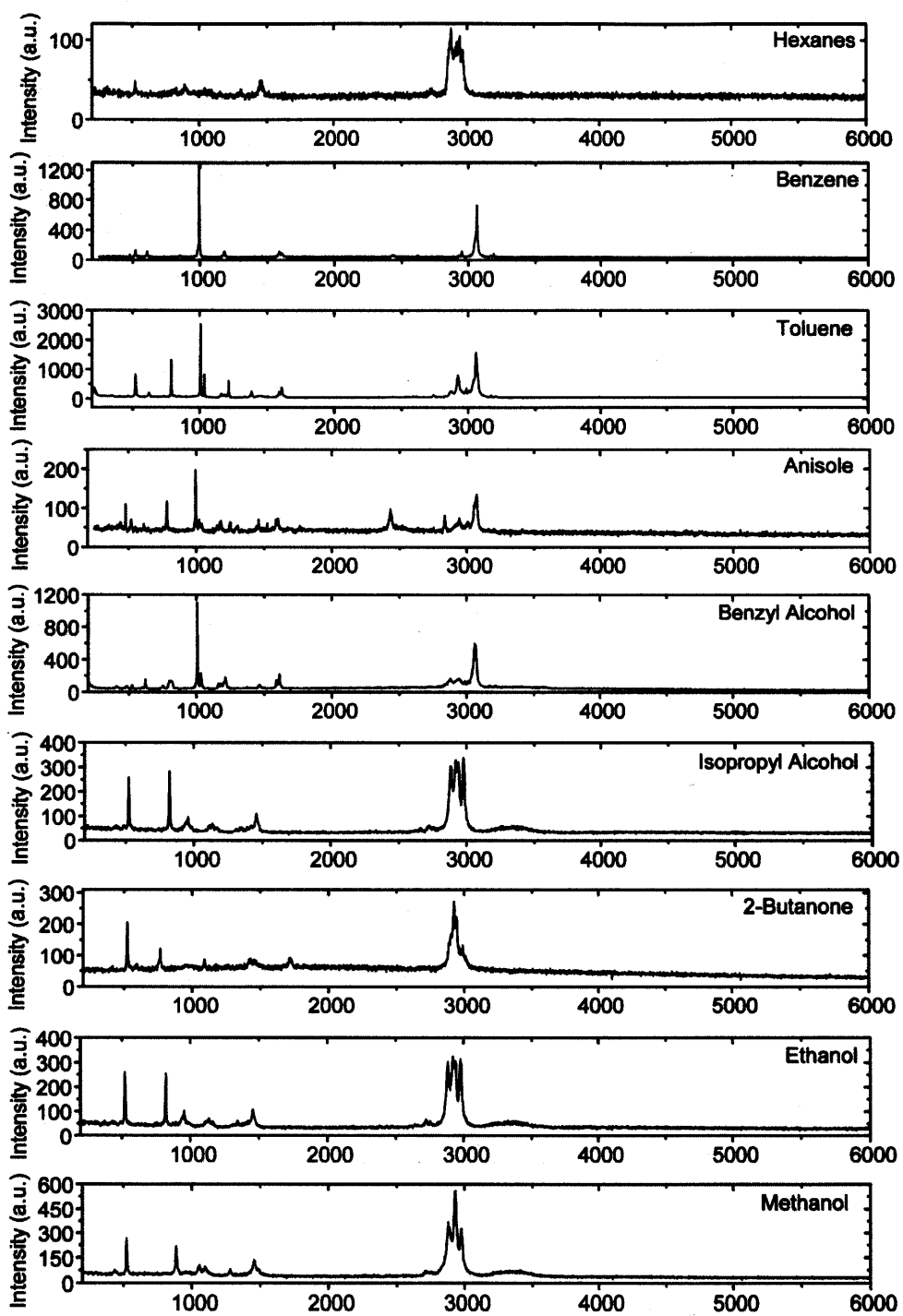
Figure 5-4 Raman spectra of the organic solvents listed in Table 5-1.

68

5.2 Optical Measurements

5.2.1 Raman spectroscopy

Figure 5-5 shows the Raman spectra of MoS_2, with the in-plane vibrational mode, E_{2g}^1, and the out-of-plane vibrational mode, A_{1g}, located at around 385 and 407 cm^{-1}, respectively. Figure 5-6 plots the Raman shifts and the intensity ratio of the E_{2g}^1 and A_{1g} peaks as a function of the solvent dielectric constant. No clear correlation can be found between the Raman spectra and the dielectric constant of the environment.
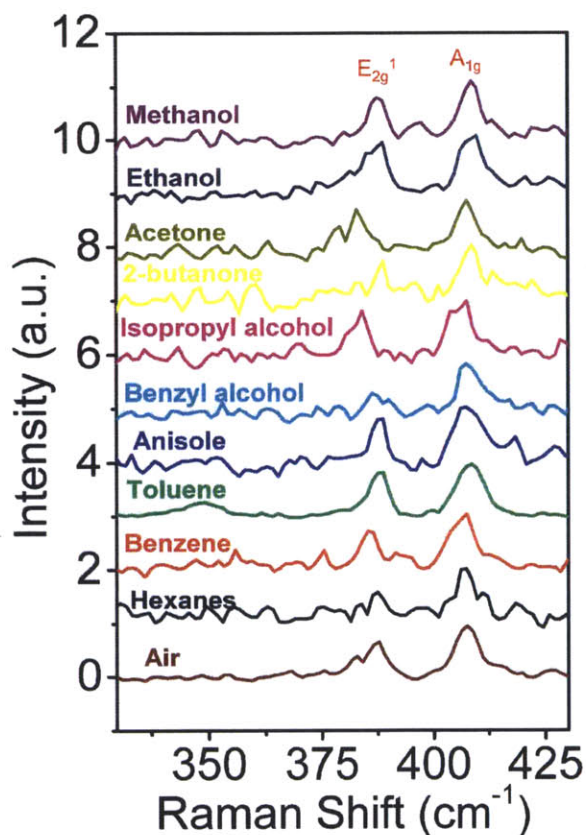
Figure 5-5 The Raman spectra of monolayer MoS_2 exposed to air or immersed in different solvents. The spectra are arranged by an ascending order (from bottom to top) according to the dielectric constant of the solvents. The wavelength of the excitation laser is 532.5 nm.
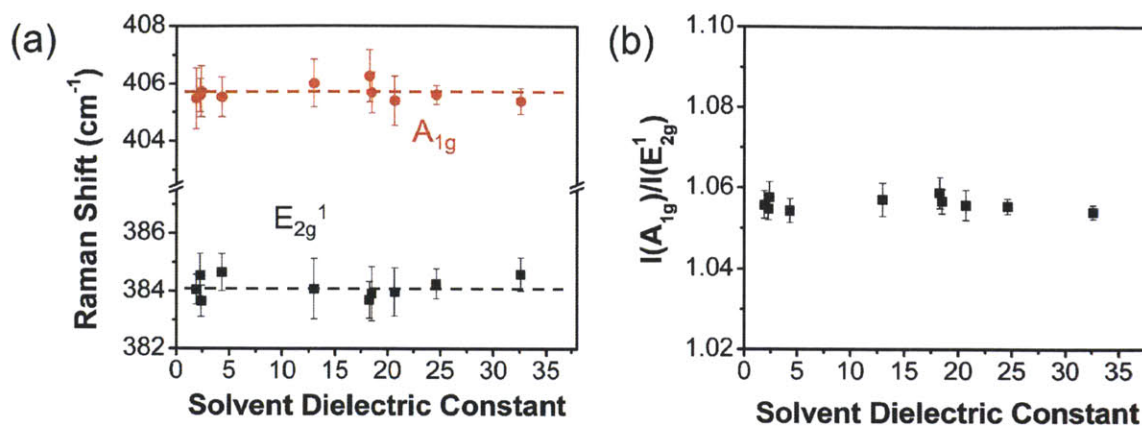
Figure 5-6 (a) Peak positions and (b) intensity ratio of the two Raman modes of monolayer MoS$_2$ as a function of the static dielectric constant of the solvents.

5.2.2 Photoluminescence

Figure 5-7 shows typical PL spectra of monolayer MoS2 with the bottom surface in contact with the SiO2/Si substrate, while the top surface is exposed to air or to different solvents. The multiple sharp peaks in Figure 5-7 are from the Raman vibrational modes of the solvent, as well as from the MoS$_2$ or the SiO$_2$/Si substrate. The assignments of these peaks are shown in Figure 5-4.
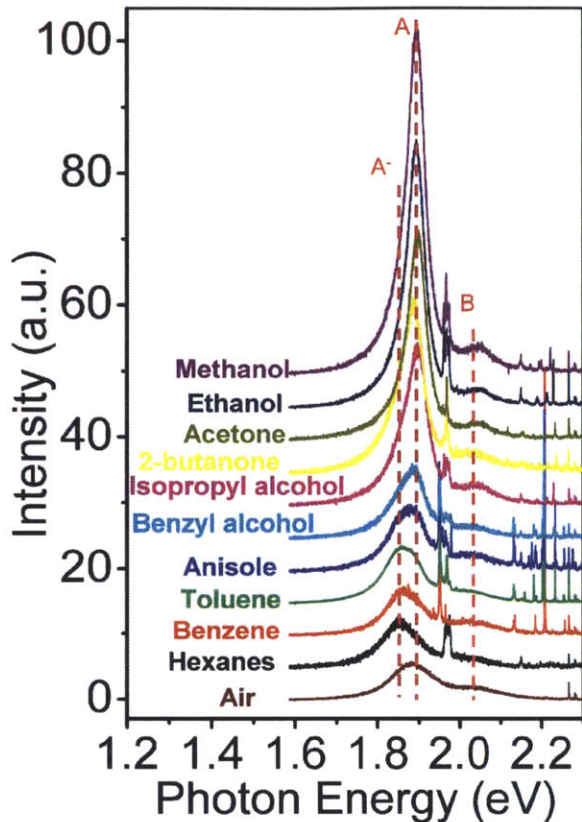
Figure 5-7 Photoluminescence of monolayer MoS_2 exposed to air or immersed in different solvents. The spectra are arranged by an ascending order (from bottom to top) according to the dielectric constant of the solvents. The red dashed lines denote roughly the peak energies of the A⁻ trion, and the A and B excitons.

In Figure 5-8, one typical PL spectrum of the measurement with each solvent was fitted with three peaks, which have been assigned to originate from the radiative combination of the A- trion (~1.85 eV), the A exciton (~1.90 eV) and the B exciton (~2.03 eV), respectively [153,226]. We notice that the intensity of the A- trion peak (black curve) is comparable with the intensity of the A exciton (red curve). The strong radiative recombination of trions in LTMD materials is consistent with the study published elsewhere [153-156]. The peak positions, accumulated intensities normalized by the A_{1g} Raman peak intensities, and full widths at half maximum (FWHM) of all three PL peaks as a function of the dielectric constant of the solvents are plotted in Figure 5-9. From

Figure 5-9(a), it is observed that the energy positions of all the three peaks increase as the dielectric constant of the solvent increases, whereas these blue shifts start to saturate when the dielectric constant exceeds 18. We note that the A⁻ trion peak shifts faster than the A exciton peak, and the energy difference between the A⁻ trion and the A exciton peaks, i.e., the trion binding energy, becomes very small in high-κ solvents. We further find that the intensities of the PL peaks are enhanced approximately exponentially as a function of the dielectric constant of the solvent, as shown in Figure 5-9(b), where the PL intensities vs. dielectric constant is plotted on a semi-log plot. The A- trion peak is enhanced by ~4 times, the A exciton peak by ~20 times, and the B exciton peak by less than 2 times. There is also a negative correlation between the peak widths and the dielectric constant of the solvent for all three peaks, according to the plots shown in Figure 5-9(c).
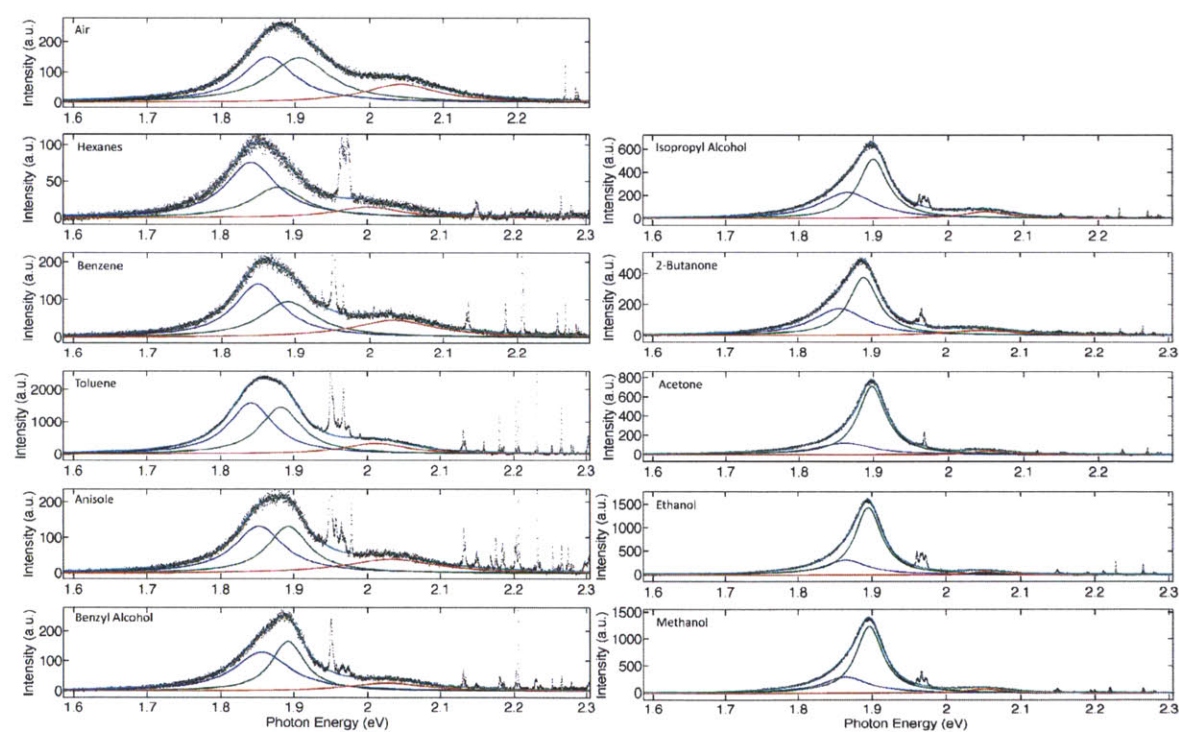
Figure 5-8 PL spectra of monolayer MoS₂ in 10 different solvents fitted with 3 Lorentzian peaks. The blue, green and red curves are the fitted Lorentzian functions of the A⁻, A and B peaks; the black curves are the summation of the Lorentzian functions. The grey dots are experimental points.
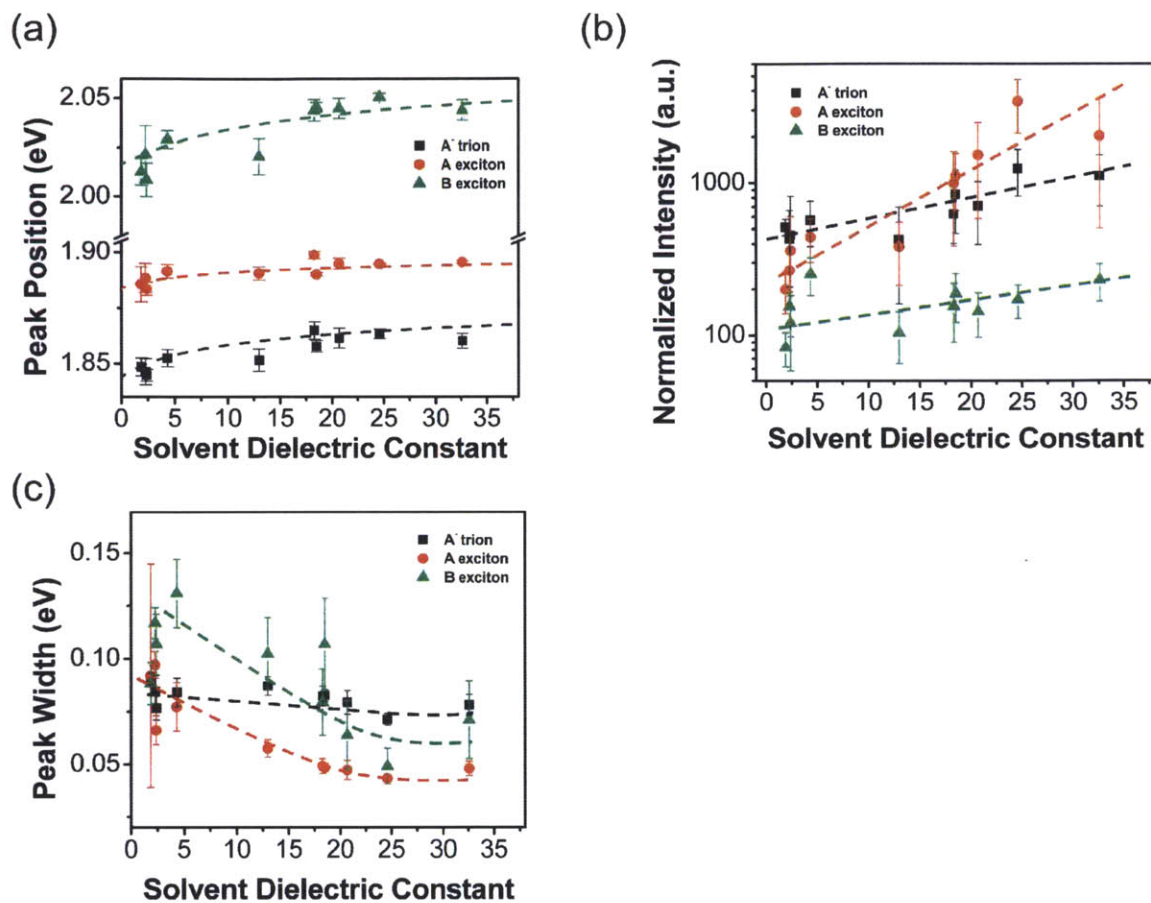
Figure 5-9 (a) The PL peak positions as a function of the solvent dielectric constant. The dots with error bars are experimental data, and the dashed curves are fitting curves from the scaling relationship (see Section 4.3). (b) Accumulated PL intensities normalized to the A_{1g} Raman peak intensities, with the dots together with their error bars showing experimental data, and the dashed lines are the guides to the eye. (c) Full width at half maximum (FWHM) of the PL peaks as a function of the solvent dielectric constant. The dots here are the mean value for all the solvents used, weighted according to their errors. The dashed curves are the guides to the eye.

5.3 The Effect of Dielectric Screening

5.3.1 Theoretical Analysis

The PL peak energy of direct-bandgap semiconductors, usually called the optical band gap, is equal to the electronic band gap calculated from the electronic dispersion relation minus the binding energy of the quasiparticles (excitons or trions) originating from the Coulomb interactions between the electrons and holes. The three PL peaks experimentally observed in monolayer MoS_2 reflect the optical transition energies of the excitons and trions, which can be expressed as

$$PL_A = E_g - \varepsilon_A \tag{5-1}$$

$$PL_B = E_g + \Delta - \varepsilon_B \tag{5-2}$$

$$PL_{A-} = E_g - \varepsilon_A - \varepsilon_{A-} \tag{5-3}$$

The binding energies of the quasiparticles reflect the Coulomb interaction between the negatively charged electrons and the positively charged holes, which can be calculated through the reduced-mass hydrogen atom model in the 2D case [147]. However, the Coulomb potential distribution is strongly screened by the environmental dielectrics. The impact of the boundary conditions on the Coulomb potential distributions due to the dielectric mismatch is equivalent to the generation of an infinite array of image charges. Consider the dielectric-sandwiched structure with the relative dielectric constants of the top, bottom and the middle layers denoted by κ_1, κ_2 and κ_s, respectively, as shown in Figure 5-10. The thickness of the middle layer is denoted by D. The origin of the x-z coordinate in Figure 5-10 (a) is located in the center of the middle layer. Assuming there is one positive charge (+q) and one negative charge (-q) fixed at (L/2,0) and (-L/2,0), respectively, the infinite arrays of image charges will be generated by the mirror surfaces of the interfaces between the different materials, as shown in Figure 5-10 (b).
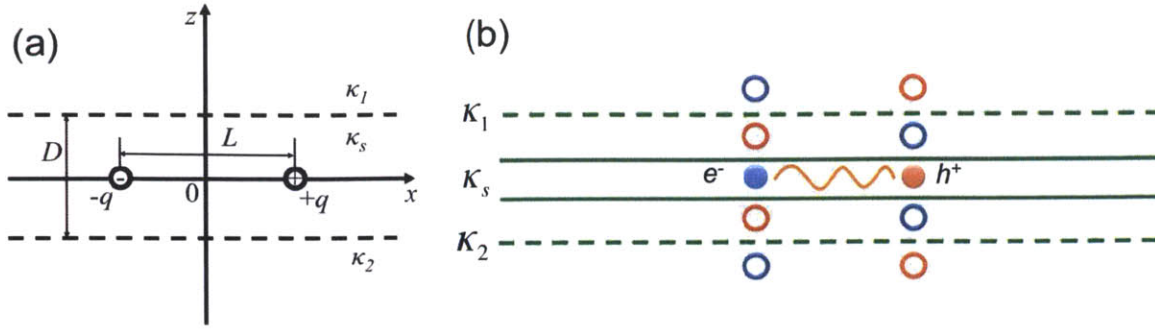
Figure 5-10 (a) Schematic diagram of the coordinates and related parameters of the Coulomb potential problem in MoS$_2$. (b) Schematic of the generation of the image charges.

If the image charges and positions are denoted by $\{q_{X,n}\}$ and $\{(x_{X,n}, z_{X,n})\}$, where X replaced by $T+$ (images charges in the top dielectrics originating from the positive charge), $T-$ (images charges in the top dielectrics originating from the negative charge), $B+$ (image charges in the bottom dielectrics originating from the positive charge) or $B-$ (image charges in the bottom dielectrics originating from the negative charge), and $n=1,2,3,...$, The net Coulomb potential originated from the two charges $+q$, $-q$ at a certain point (x, z) is given by

$$V(x,z) = \frac{1}{4\pi\varepsilon_0 \kappa_s}\left[\frac{+q_0}{\sqrt{(x-L/2)^2+z^2}}+\frac{-q_0}{\sqrt{(x+L/2)^2+z^2}}\right]+\frac{1}{4\pi\varepsilon_0 \kappa_s}\sum_{X,n}\frac{q_{X,n}}{\sqrt{(x-x_{X,n})^2+(z-z_{X,n})^2}}$$

(5-4)

where ε_0 is the vacuum permittivity, κ_s is the relative dielectric constant of the middle layer, and $\pm q_0$ are the effective charges located at $(\pm L/2, 0)$. The image charges and positions are summarized below.

i) When $|z|<D/2$,

$$q_0 = q$$

$$q_{B+,2n} = -q_{B-,2n} = q(\zeta_1\zeta_2)^n$$

$$q_{B+,2n-1} = -q_{B-,2n-1} = q(\zeta_1\zeta_2)^{n-1}\zeta_1$$

$$q_{T+,2n} = -q_{T-,2n} = q(\zeta_1\zeta_2)^n$$

$$q_{T+,2n-1} = -q_{T-,2n-1} = q(\zeta_1\zeta_2)^{n-1}\zeta_2$$

$$z_{B+,n} = z_{B-,n} = -nD$$

$$z_{T+,n} = z_{T-,n} = +nD$$

where $\zeta_1 = (\kappa_s - \kappa_1)/(\kappa_s + \kappa_1)$ and $\zeta_2 = (\kappa_s - \kappa_2)/(\kappa_s + \kappa_2)$.

ii) When $z < -D/2$,

$$q_0 = q\zeta_1'$$

$$q_{T+,2n} = -q_{T-,2n} = q(\zeta_1\zeta_2)^n\zeta_1'$$

$$q_{T+,2n-1} = -q_{T-,2n-1} = q(\zeta_1\zeta_2)^{n-1}\zeta_1'\zeta_2$$

$$q_{B+,n} = q_{B-,n} = 0$$

$$z_{T+,n} = z_{T-,n} = +nD$$

where $\zeta_1' = 2\kappa_1/(\kappa_s + \kappa_1)$.

iii) When $z > D/2$,

$$q_0 = q\zeta_2'$$

$$q_{B+,2n} = -q_{B-,2n} = q(\zeta_1\zeta_2)^n\zeta_2'$$

$$q_{B+,2n-1} = -q_{B-,2n-1} = q(\zeta_1\zeta_2)^{n-1}\zeta_2'\zeta_1$$

$$q_{T+,n} = q_{T-,n} = 0$$

$$z_{B+,n} = z_{B-,n} = +nD$$

where $\zeta_2' = 2\kappa_2/(\kappa_s + \kappa_2)$.

Figure 5-11 and Figure 5-12 summarize the net Coulomb potential distributions of the electron-hole pair in the dielectric-sandwiched structure with different dielectric constant configurations. The net potential of the image charges diminishes the total potential if the environmental dielectric constants κ_1 and κ_2 are larger than the MoS$_2$ dielectric constant κ_s, and strengthens the total potential if κ_1 and κ_2 are smaller.
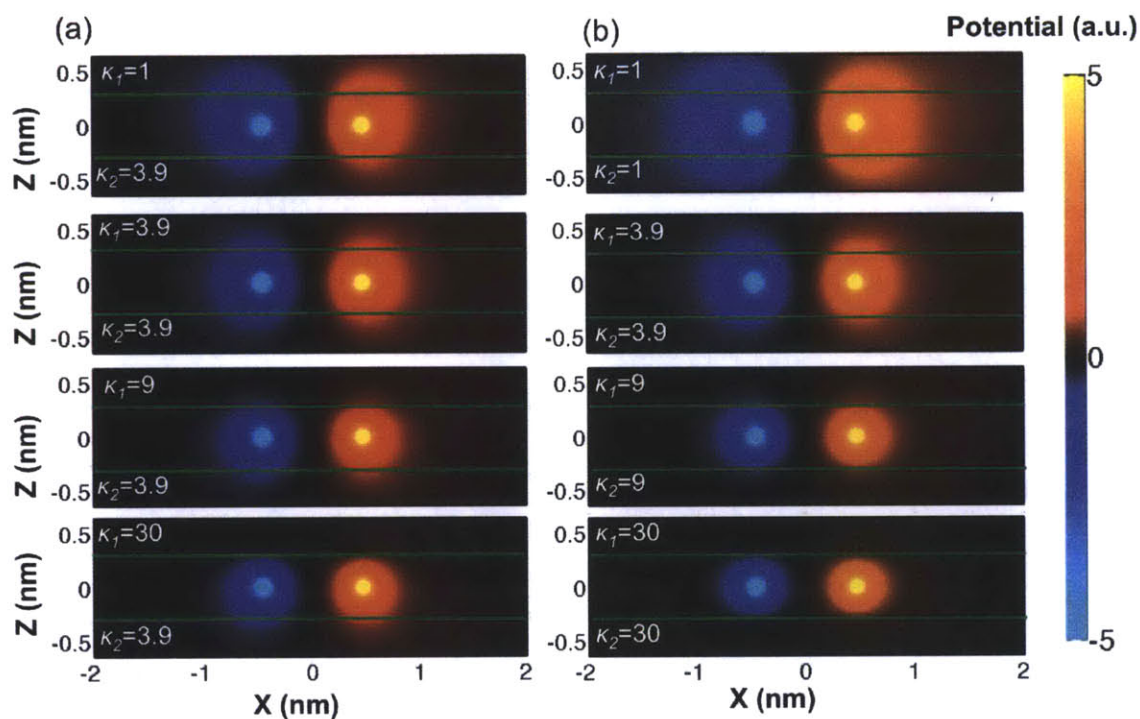
Figure 5-11 Coulomb potential distribution of the dielectric-sandwiched structure. (a) The asymmetric case, in which the bottom layer is fixed (SiO$_2$). (b) The symmetric case, in which both layers can be adjusted freely.
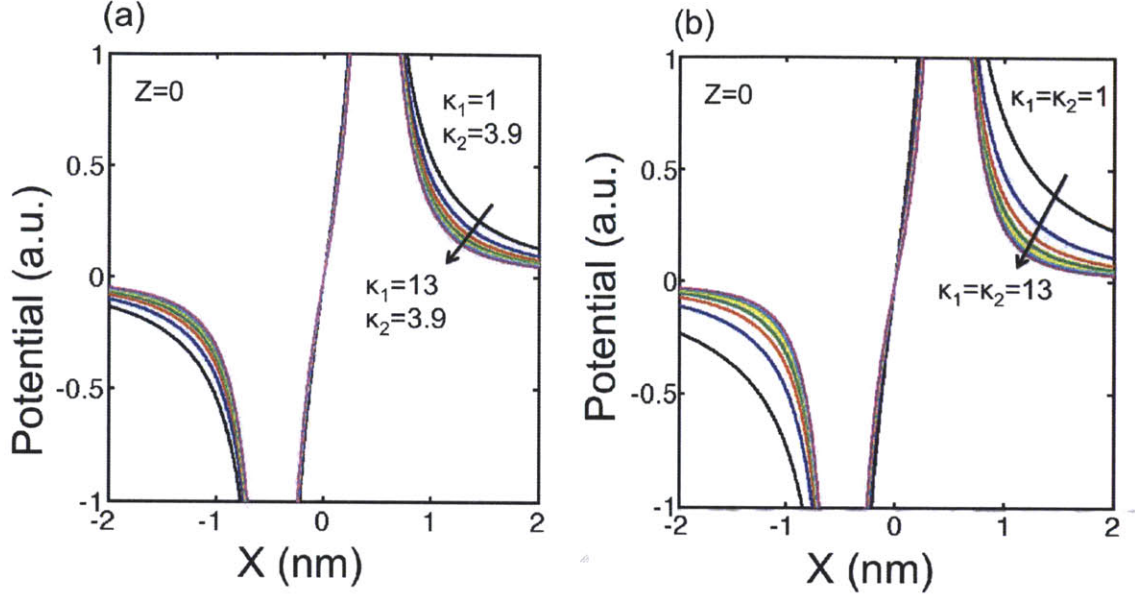
Figure 5-12 The Coulomb potential distribution at the $z=0$ line.

The dielectric-screened Coulomb potential for the electron and hole separated by a distance L can be expressed in the form of

$$V_{2D}(L) = \frac{e^2}{\varepsilon_0 \kappa_{eff} L_0} f_1\left(\frac{L}{L_0}\right) \tag{5-5}$$

where ε_0 and e are the vacuum permittivity and the electron charge, $\kappa_{eff}=(\kappa_1+\kappa_2)/2$ is the effective relative dielectric constant, and L_0 is the screening length. Here $f(L/L_0)$ is a dimensionless function. In particular, the 2D Coulomb potential can be simplified to [150]

$$V_{2D}(L) = \frac{\pi e^2}{\varepsilon_0 (\kappa_1 + \kappa_2) L_0} \left[H_0\left(\frac{L}{L_0}\right) - Y_0\left(\frac{L}{L_0}\right) \right] \tag{5-6}$$

where H_0 and Y_0 are respectively the Struve function and the Bessel function of the second kind [150].

Based on the effective-mass approximation, the exciton binding energy is given by

$$E(L) = \frac{\hbar^2}{2\mu L^2} - \frac{e^2}{\varepsilon_0 \kappa_{eff} L_0} f_1\left(\frac{L}{L_0}\right) \tag{5-7}$$

in which the first term is the kinetic energy, and μ is the reduced effective mass of the electron-hole pair. The second term is the simplified dielectric-screened Columb potential given by Eq. (5-5). The expression for the binding energy can be rewritten as

$$E(L) = \frac{\hbar^2}{\mu L^2} \left[\frac{1}{2} - \frac{e^2}{\hbar^2 \varepsilon_0} \frac{\mu L}{\kappa_{eff}} \frac{L}{L_0} f_1(\frac{L}{L_0}) \right] = \frac{\hbar^2}{\mu L^2} f_2(\frac{L}{L_0}, \frac{\mu L}{\kappa_{eff}})$$ (5-8)

The binding energy E_b in real systems is the minimum of $E(L)$ where L/L_0 is equal to a specific constant (k). Therefore,

$$E_b = \min_L \{E(L)\} = \frac{\hbar^2}{\mu L^2} f_2(\frac{L}{L_0}, \frac{\mu L}{\kappa_{eff}})\bigg|_{\frac{L}{L_0}=k} = \frac{\hbar^2}{\mu(kL_0)^2} f_3(\frac{\mu k L_0}{\kappa_{eff}})$$ (5-9)

We assume that the f_3 function is a power law function of the variable $\mu L/\kappa_{eff}$, that is,

$$E_b \approx \frac{\hbar^2}{\mu(kL_0)^2} (\frac{\mu k L_0}{\kappa_{eff}})^\alpha \propto (kL_0)^{\alpha-2} \mu^{\alpha-1} (\kappa_{eff})^{-\alpha}$$ (5-10)

where α is a scaling factor.

In the case of monolayer MoS_2, the exciton binding energy ε_X can be expressed as

$$\varepsilon_X = \varepsilon_{X0}(\kappa_{eff})^{-\alpha_X}$$ (5-11)

where ε_{X0} is the exciton binding energy in vacuum, and α_X is an empirical scaling factor. Here X stands for the A, B or A$^-$ excitations. We assume that the A and B excitons should exhibit similar behaviors, since the only difference between the A and B excitons is that the holes come from the two separated valence bands [88,89]. Therefore, the fitting parameters of A and B should be close to each other, that is, $\alpha_A \approx \alpha_B$ and $\varepsilon_{A0} \approx \varepsilon_{B0}$. According to Berghäuser et al. [144], the binding energies of the A and B excitons are 860 and 870 meV in vacuum, and 455 and 465 meV, with one surface in direct contact with SiO_2, respectively, which is consistent with our assumption. These values were used as fixed parameters in our fitting. The binding energy of the A$^-$ trion (ε_{A^-}) should follow the same power law, except that the scaling factor α_{A^-} may have a distinct value. On the other hand, the electron-electron interaction, or the electron self-energy should also be influenced by dielectric screening, in a similar way as the electron-hole interaction. This electron self-

energy adds a renormalization term to the electronic band gap, which has been reported to be prominent in low-dimensional systems, especially in LTMDs [144-152]. As a result, the quasiparticle electronic band gap E_{gX} can be given by

$$E_{gX} = E_{SPX} + E_{BGRX} = E_{SPX} + \frac{E_{BGRX0}}{(\kappa_{eff})^{\beta_X}} \tag{5-12}$$

where E_{SPX} and E_{BGRX} are the electronic band gap from the single-particle model, and the electron self-energy band gap renormalization term, respectively, while X stands for A or B, indicating different subbands. Following a similar scaling relationship, E_{BGRX} can be further expressed by the renormalization term in vacuum, denoted as E_{BGRX0}, divided by the power function of κ_{eff} with the scaling parameter β_X. Note that $E_g = E_{gA}$, and $\Delta = E_{gB} - E_{gA}$. Therefore, the PL peak energies of the A exciton, the B exciton and the A⁻ trion are given by

$$PL_A = E_g - \frac{\varepsilon_{A0}}{(\kappa_{eff})^{\alpha_A}} = E_{SPA} + \frac{E_{BGRA0}}{(\kappa_{eff})^{\beta_A}} - \frac{\varepsilon_{A0}}{(\kappa_{eff})^{\alpha_A}} \tag{5-13}$$

$$PL_B = E_g + \Delta - \frac{\varepsilon_{B0}}{(\kappa_{eff})^{\alpha_B}} = E_{SPB} + \frac{E_{BGRB0}}{(\kappa_{eff})^{\beta_B}} - \frac{\varepsilon_{B0}}{(\kappa_{eff})^{\alpha_B}} \tag{5-14}$$

$$PL_{A-} = E_g - \frac{\varepsilon_{A0}}{(\kappa_{eff})^{\alpha_A}} - \frac{\varepsilon_{A-,0}}{(\kappa_{eff})^{\alpha_{A-}}} = E_{SPA} + \frac{E_{BGRA0}}{(\kappa_{eff})^{\beta_A}} - \frac{\varepsilon_{A0}}{(\kappa_{eff})^{\alpha_A}} - \frac{\varepsilon_{A-,0}}{(\kappa_{eff})^{\alpha_{A-}}} \tag{5-15}$$

5.3.2 Parameter Extraction and Explanation of the Experiment

Figure 5-9(a) shows in dashed lines the PL peak energies as a function of the dielectric constant of the solvents fitted by the Eqs. (5-3)-(5-5). The fitting results match the experimental data very well. Figure 5-13(a) plots the electronic band gap, single-particle band gap, the A exciton and A⁻ trion PL peak positions, and Figure 5-13 (b) plots the relative binding energies of the A and B excitons and of the A⁻ trion as a function of the effective dielectric constant. Both the electronic band gap and the exciton binding energies are relatively large when MoS_2 is in vacuum, and decrease rapidly with the effective dielectric constant. The PL peak positions, or optical band gaps of the excitonic quasiparticles are the differences between those energies; thus the large changes cancel out

mostly, leading to small changes of the PL peak positions as a function of the dielectric constant. In an extreme case, if the effective dielectric approaches infinity, both the electron self-energy renormalization and the excitonic binding energies are infinitesimal, and the optical band gaps are close to the single-particle band gap. The binding energies of the A, B exciton and A⁻ trion with both surfaces in vacuum are extracted to be 859, 870 and 44 meV, respectively. The electronic band gap of monolayer MoS_2 in vacuum is around 2.73 eV. Figure 5-13(a) also summarizes the reported values from different calculation methods in the literature, which are also shown in Table 2-2. Density functional theory (DFT) calculations provide the band structure without considering the electron-electron interactions. The calculated band gap from the DFT method, ranging from 1.6 to 2.1 eV, should be equal to E_{SP} (~1.90 eV) according to our model. The many-body perturbation GW theory includes the effect of the electron-electron interaction, with the calculated band gap of 2.4-2.8 eV. The excitonic effect can be considered by using the Mott-Wannier theory or solving the Bethe-Salpeter equation (BSE), which gives the binding energy of 500-1100 meV, and the optical band gap of 1.74-2.0 eV, respectively. The estimated values based on our model are in good agreement with these calculations. The valence band splitting at the K point is estimated to be 172 meV, very close to theoretical anticipations [144-151] and previous PL and absorption measurements [88,89]. Figure 5-14 shows the dependence of the valence band splitting on the effective dielectric constant. The scaling factors in our fittings are $\alpha_A=0.7\pm0.2$, $\alpha_B=0.7\pm0.2$, $\alpha_{A-}=0.16\pm0.06$, $\beta_A=0.7\pm0.2$ and $\beta_B=0.8\pm0.2$.
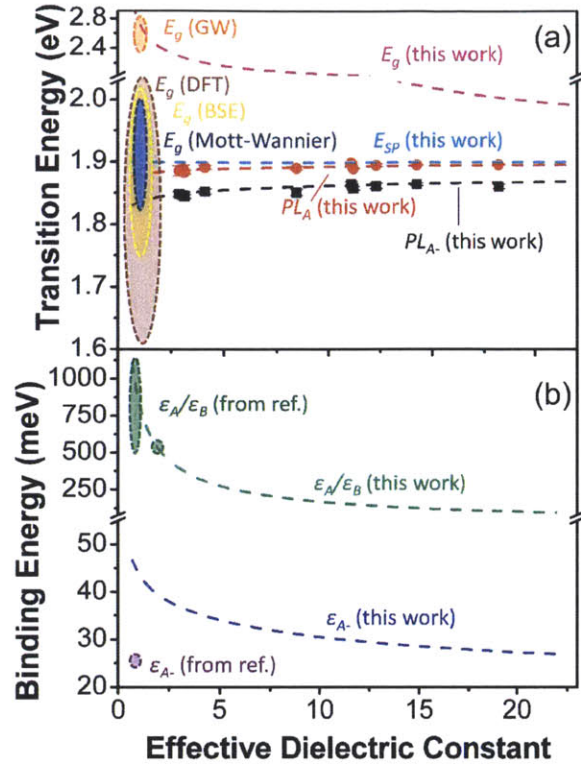
Figure 5-13 (a) Dependence of the PL peak energies of the A exciton (*PL_A*, red) and A⁻ trion (*PL_A-*, black), the electronic band gap (*E_g*, magenta), the band gap based on the single-particle picture (*E_SP*, cyan) on the effective dielectric constant. The dots with error bars are experimental data, and the dotted lines are the fitting results from the binding energy scaling relationship. (b) Dependence of the binding energies of the A/B exciton (green) and A⁻ trion (blue) on the effective dielectric constant. The shaded areas with different colors are the calculated results by other groups [144-152].
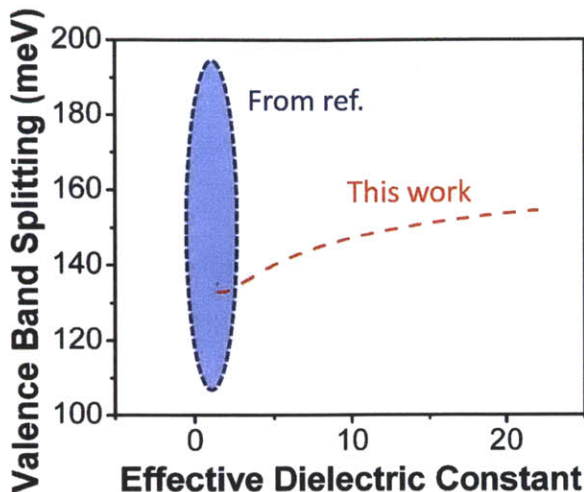
Figure 5-14 The valence band splitting (red dashed line) exracted from the experimental work in this paper as a function of the effective dielectric constant in comparison with the calculated results from the literature [144-152] (blue shaded area).

From Figure 5-9(b), we observed that the peak intensities of the A, B excitons and A⁻ trions increase exponentially with the solvent dielectric constant. It is also noted that the peak widths decrease with the solvent dielectric constant, according to Figure 5-9(c). Given that the PL peak width is inversely proportional to the lifetime of the quasiparticles, we can infer that the lifetimes of the excitons and trions in monolayer MoS_2 become larger when immersed in high-κ dielectric environments. As we can see in Figure 5-11, the Coulomb potential becomes more confined within the middle layer if the dielectric constants of the top and bottom layers are higher. This may help to reduce the scattering between the excitons (trions) and the charged impurities at the MoS_2/dielectrics interface [233-235], and thus prolong the lifetime of the excitons (trions). As a result, the quantum efficiency of the excitonic recombination process becomes larger when MoS_2 is in high-κ environments. This explains the enhancement of the PL intensities of MoS_2 by high-κ dielectrics. However, the non-radiative recombination rate of the excitons is still so high that the lifetime of excitons in monolayer MoS_2 is only about 80 ps, according to Shi et al [244]. Because of this, the excitons and trions may have very low mobility and, consequently, a very slow response to the electric field change. This explains why there is no clear correlation between the PL spectra and the high-frequency dielectric constant of

the solvents as shown in Figure 5-15. Here the high-frequency dielectric constant is defined as the square of the refractive index of the solvent in the visible range.
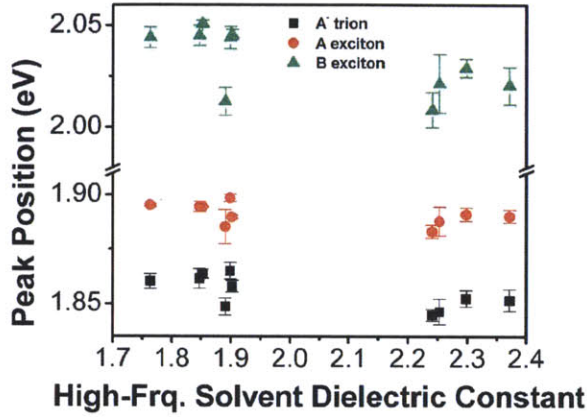
Figure 5-15 PL peak energies as a function of the high-frequency dielectric constant of the solvents. The high-frequency dielectric constants are obtained by the square of the refractive indices of the solvents in the visible range.

The intensity ratio of trions and excitons can be tuned by the environmental dielectric constant as well. As shown in Figure 5-16(a), the A^-/A intensity ratio decreases from 2.5 to 0.4 as the effective dielectric constant varies from 3 to 20 (or the solvent dielectric constant consequently varies from 1.89 to 32.6). From the mass action model (see Chapter 4 for more details), the trion/exciton intensity ratio can be expressed as

$$\frac{I(A^-)}{I(A)} = \frac{\Gamma_{A-}N_{A-}}{\Gamma_A N_A} \propto \frac{\Gamma_{A-}}{\Gamma_A}\frac{1}{n_e}\exp(\frac{\varepsilon_{A-}}{k_B T}) \tag{5-16}$$

where Γ_{A-} and Γ_A are the radiative recombination rates, and N_{A-} and N_A are, respectively, the density of A^- and A; n_e is the electron density; and $k_B T$=25.9 meV is the thermal energy at room temperature (300K). The radiative recombination should be influenced by the environmental dielectrics as well, similar to other low-dimensional systems [230]; thus the ratio of the A^-/A radiative recombination rate (inverse of the radiative lifetime) is assumed to follow a power law function of the effective dielectric constant; that is, $\Gamma_{A-}/\Gamma_A \propto (\kappa_{eff})^\delta$. Therefore, the A^-/A intensity ratio is given by

$$\frac{I(A^-)}{I(A)} = K(\kappa_{eff})^\delta \exp(\frac{\varepsilon_{A-}}{k_B T})\qquad\qquad(5\text{-}17)$$

with the fitting parameters K and δ. Figure 5-16(b) shows the fitting results compared with the experimental data. The fitting parameter δ=-0.7 and K=$(\Gamma_{A-}/\Gamma_A)_{\kappa eff=1} 4 m_A m_e k_B T/(\pi \hbar^2 m_{A-} n_e)$=0.958. Here the ratio of the intrinsic radiative recombination rate $(\Gamma_{A-}/\Gamma_A)_{\kappa eff=1}$ is around 0.1[226]. This model gives an estimation of the electron density of $\sim 10^{12}$ cm^{-2}, which is in good agreement with the values reported by others [226,233]. From the mass action model, we can expect that the A$^-$/A intensity ratio can be as high as 5.5 if both sides of MoS$_2$ are exposed to vacuum ($\kappa_1=\kappa_2=1$), or as low as 0.10 if MoS$_2$ are exposed to an ultrahigh-κ dielectric (for example, $\kappa_1=\kappa_2=100$), as shown in Figure 5-16(b).
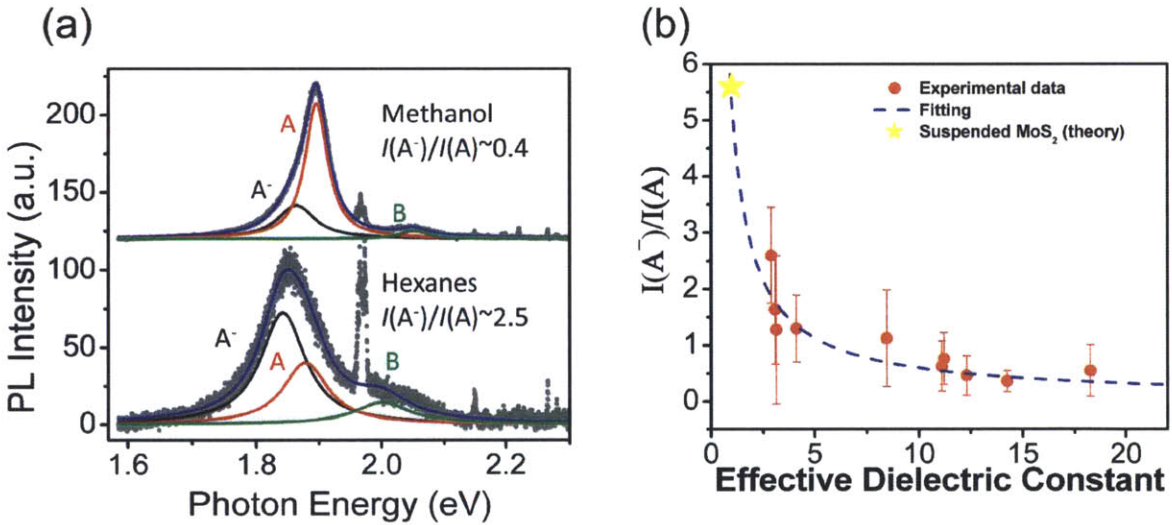
Figure 5-16 (a) PL spectra of monolayer MoS$_2$ immersed in methanol and hexanes, respectively. Grey dots are experimental data, and the black, red and green lines are the fitting curves of the peaks of the A$^-$ trion, A exciton and B exciton, respectively, with the blue line the summation of the three fitting curves. (b) Dependence of the A$^-$/A intensity ratio on the effective dielectric constant. The red dots with error bars are experimental data, and the blue dashed line represents the fitting results from the mass action model. The yellow star is the estimated intensity ratio of suspended MoS$_2$ with both surfaces in vacuum according to our model.

5.4 Analysis of Other Effects

5.4.1 The Effect of Doping and Strain Induced by the Solvents

From Raman spectroscopy measurements, if the solvents induce any strain [245] or doping [225] effects in the MoS_2, the E_{2g}^1 and A_{1g} Raman vibrational modes should shift. However, none of these were observed in our data, as shown in Figure 5-6(a). There is no clear dependence of the intensities and widths of the Raman modes on the type of solvents as well. Therefore, we can neglect any doping or strain induced by these solvents.

5.4.2 Raman and PL Spectra in Ambient and in Vacuum

Figure 5-7 also shows the PL spectrum of MoS_2 when exposed to ambient. The three PL peaks of MoS_2 are located at 1.85, 1.89 and 2.03 eV, respectively; yet the dielectric constant of air is 1, and from the trend generalized from Figure 5-9(a) and (b), the PL peaks of monolayer MoS_2 in air should have the lowest peak energies, and the weakest peak intensities. To understand this unexpected observation, PL and Raman spectra were taken on MoS_2 in vacuum, and a comparison was made with those taken in air. The PL and Raman spectra of monolayer MoS_2 in vacuum (less than 10^{-4} torr) are distinct from those in air, as shown in Figure 5-17. More specifically, the PL peaks of monolayer MoS_2 measured in vacuum are located at around 1.77, 1.83 and 1.95 eV, respectively, and the peak intensities are much smaller than those measured in air. These observations are in accordance with the trend obtained from the solvent-based PL data. This difference of the peaks in air and in vacuum may be attributed to the carrier depletion effects induced by the p-type doping of MoS_2 by the water and other high-electronegativity molecules present in air and absorbed by the anion vacancy defects [246], which helps to enhance the quantum yield of the PL process when MoS_2 samples are surrounded by air. The intensity ratio of the A_{1g} and E_{2g}^1 Raman modes is also smaller when MoS_2 is in vacuum than in air, as shown in the inset of Figure 5-17. This trend is a further indication of the

existence of the p-doping effect, as has been observed in electrochemically gated MoS_2 [225].
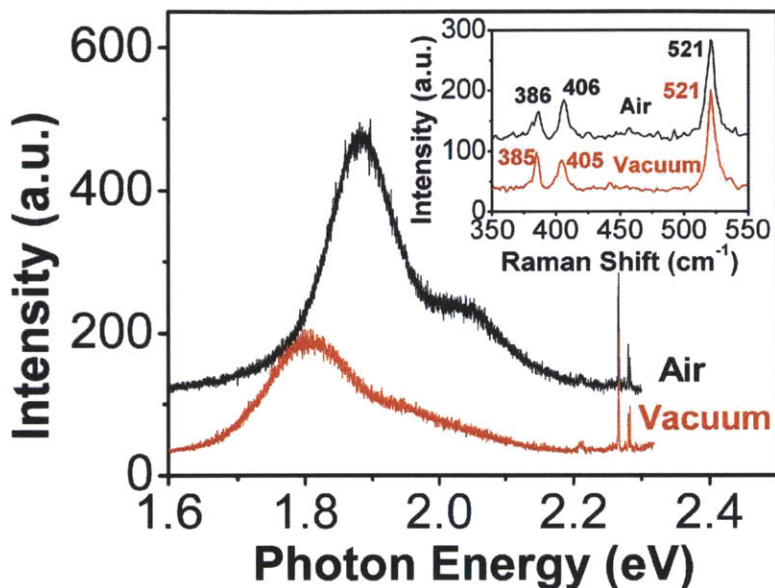
Figure 5-17 PL and (inset) Raman spectra of monolayer MoS_2 in air (black) and in vacuum (red).

5.2.3 The Effect of Interference

And finally, the interference effect on the incident and excited light introduced by the Solvent/MoS_2/SiO_2/Si structure was examined. According to Li et al. [247], an interference enhancement factor should be considered in the total PL intensity if the dielectric configuration changes. However, this enhancement factor only varies by less than 20% throughout our measurements when different solvents are used as the external dielectrics, and these small changes are far below the enhancement (>10 times) observed in the experiment (Figure 5-7). Therefore, the interference effect should make negligible contributions to the change of the PL intensities.

Chapter 6. Conclusion and Future Work

6.1 Conclusion

In this thesis, the optical properties, such as Raman scattering, photoluminescence and absorption on 2-dimensional transition metal dichalcogenides are systematically studied. The lattice structure, phonon and electron dispersions of bulk and monolayer TMDs are introduced. The lattice symmetries and vibrational modes are summarized. The Raman spectra of monolayer and bulk MoS_2, WS_2, $MoSe_2$ and WSe_2 with different wavelengths of the excitation laser are assigned with the individual and combined vibrational modes. The PL and absorption spectra are shown using general fitting methods for such spectra, and the origins of the peaks are investigated, which introduces the concept of excitons and trions. Later on, monolayer MoS_2 is taken as an example to study two environmental effects – electrical doping and dielectric screening – on the many-body interactions in quantum confined systems. The electrical doping is induced by the polymer electrolyte gating technology, with the capacity of changing the carrier density in MoS_2 from 10^{11} cm^{-2} to 10^{13} cm^{-2}. The field effect mobility is enhanced by more than one order of magnitude, the A_{1g} Raman mode softens and broadens, and the exciton and trion peaks red-shift and decay exponentially with the increase of the carrier density. The external dielectric constant is tuned by the immersion of the monolayer MoS_2 into different non-ionic organic solvent with a wide range of static dielectric constants from 2 to 33. Despite no clear correlation between the Raman spectroscopy results and the external dielectric constants was found, the PL peaks corresponding to both the excitons and trions are shifted and enhanced with the dielectric environments. The change of the PL in monolayer MoS_2 can be explained by the effect of dielectric screening. A scaling relationship is developed, providing an estimation of some of the band structure parameters and excitonic binding energies. The population ratio of trions and excitons was found to be tuned by the external dielectric constant, which provide a simple approach to separating and controlling the excitons and trions in 2D TMDs.

6.2 Future Work

Due to their uniqueness and diversity, transition metal dichalcogenides and other two-dimensional materials are of far-reaching importance in scientific research, and have

various potential applications that may have an impact on industries based on the practice of various aspects of electrical engineering. The nature of direct band gap and controllable valley polarization gives 2D TMDs promising opportunities in novel optoelectronics applications. The study of this thesis provides a comprehensive understanding of control of the interface between the 2D TMDs and multiple environmental effects, which is fundamental in any scientific study or engineering utilization of these materials. Future work of this topic includes:

(1) The influence of real solid substrates or dielectrics on the electronic and optical properties of 2D TMDs. When atomic-thick TMDs are in contact with other materials such as supporting substrates, metal contacts, gate dielectrics, heterojunctions, etc., there may be multiple effects on the TMDs, such as doping, strain, dielectric screening, and so on. By combining together the conclusions of the separate studies on the electrical doping and dielectric screening, we will try to understand what is happening at the interfaces between 2D TMDs and other materials in real devices.

(2) Optical properties of other 2D materials. The recently rediscovered 2D material – black phosphorus or "phosphorene" is a direct band gap semiconductor with the band gap ranging from 0.3 eV to 1.5 eV depending on the thickness of the material. This material is also anisotropic within the horizontal plane. We will continue our investigation on this new material and extend our knowledge of many-body effects in 2D semiconductors in this new system.

(3) 2D materials hybrid structures and potential applications. We expect that the photon-electron interactions are very strong in these direct band gap materials, and the applications of these materials include photodetectors, light-emitting devices, etc. Heterostructures including these 2D layered materials are significant in such applications in order to either separate the photo-generated carriers efficiently or reach a population inversion condition. We will try to study the hybrid structures of 2D TMDs and other 2D materials, and search for the best candidates for fast-response, broadband photodetecting or high-efficiency light-emission.

References

[1]   R. E. Peierls, "Quelques proprietes typiques des corpses solides," Ann. I. H. Poincare, vol. 5, pp. 177–222, 1935.

[2]   L. D. Landau, "Zur Theorie der phasenumwandlungen II," Phys. Z. Sowjetunion, vol. 11, pp. 26–35, 1937.

[3]   L. D. Landau and E. M. Lifshitz, "Statistical Physics, Part I," 1980.

[4]   N. D. Mermin, "Crystalline order in two dimensions," Phys. Rev., vol. 176, pp. 250–254, 1968.

[5]   K. S. Novoselov, "Two-dimensional atomic crystals," Proc. Natl Acad. Sci. USA, vol. 102, pp. 10451–10453, 2005.

[6]   K. S. Novoselov, "Electric field effect in atomically thin carbon films," Science, vol. 306, pp. 666–669, 2004.

[7]   K. S. Novoselov, "Two-dimensional gas of massless Dirac fermions in graphene," Nature, vol. 438, pp. 197–200, 2005.

[8]   A. K. Geim and K. S. Novoselov, "The rise of graphene," Nat Mater, vol. 6, no. 3, pp. 183–191, Mar. 2007.

[9]   A. H. Castro Neto, F. Guinea, N. M. R. Peres, K. S. Novoselov, and A. K. Geim, "The electronic properties of graphene," Rev. Mod. Phys., vol. 81, no. 1, pp. 109–162, Jan. 2009.

[10]   Y. Zhang, J. W. Tan, H. L. Stormer, and P. Kim, "Experimental observation of the quantum Hall effect and Berry's phase in graphene," Nature, vol. 438, pp. 201–204, 2005.

[11]   D. A. Abanin, I. Skachko, X. Du, E. Y. Andrei, and L. S. Levitov, "Fractional quantum Hall effect in suspended graphene: Transport coefficients and electron interaction strength," Phys. Rev. B, vol. 81, no. 11, p. 115410, Mar. 2010.

[12]   X. Du, I. Skachko, A. Barker, and E. Y. Andrei, "Approaching ballistic transport in suspended graphene," Nat Nano, vol. 3, no. 8, pp. 491–495, Aug. 2008.

[13]   E. H. Hwang, S. Adam, and S. Das Sarma, "Carrier Transport in Two-Dimensional Graphene Layers," Phys. Rev. Lett., vol. 98, no. 18, p. 186806, May 2007.

[14]   K. I. Bolotin, K. J. Sikes, Z. Jiang, M. Klima, G. Fudenberg, J. Hone, P. Kim, and H. L. Stormer, "Ultrahigh electron mobility in suspended graphene," Solid State Communications, vol. 146, no. 9–10, pp. 351–355, Jun. 2008.

[15]   J.-H. Chen, C. Jang, S. Xiao, M. Ishigami, and M. S. Fuhrer, "Intrinsic and extrinsic performance limits of graphene devices on SiO2," Nat Nano, vol. 3, no. 4, pp. 206–209, Apr. 2008.

[16]   E. H. Hwang and S. Das Sarma, "Acoustic phonon scattering limited carrier mobility in two-dimensional extrinsic graphene," Phys. Rev. B, vol. 77, no. 11, p. 115449, Mar. 2008.

[17]   L. A. Ponomarenko, R. Yang, T. M. Mohiuddin, M. I. Katsnelson, K. S. Novoselov, S. V. Morozov, A. A. Zhukov, F. Schedin, E. W. Hill, and A. K. Geim, "Effect of a High-κ Environment on Charge Carrier Mobility in Graphene," Phys. Rev. Lett., vol. 102, no. 20, p. 206603, May 2009.

[18]   W. Gannett, W. Regan, K. Watanabe, T. Taniguchi, M. F. Crommie, and A. Zettl, "Boron nitride substrates for high mobility chemical vapor deposited graphene," Applied Physics Letters, vol. 98, no. 24, p. -, 2011.

[19]   L. Wang, I. Meric, P. Y. Huang, Q. Gao, Y. Gao, H. Tran, T. Taniguchi, K. Watanabe, L. M. Campos, D. A. Muller, J. Guo, P. Kim, J. Hone, K. L. Shepard, and C. R. Dean, "One-Dimensional Electrical Contact to a Two-Dimensional Material," Science, vol. 342, no. 6158, pp. 614–617, 2013.

[20]   K. F. Mak, M. Y. Sfeir, Y. Wu, C. H. Lui, J. A. Misewich, and T. F. Heinz, "Measurement of the Optical Conductivity of Graphene," Phys. Rev. Lett., vol. 101, no. 19, p. 196405, Nov. 2008.

[21]   R. R. Nair, P. Blake, A. N. Grigorenko, K. S. Novoselov, T. J. Booth, T. Stauber, N. M. R. Peres, and A. K. Geim, "Fine Structure Constant Defines Visual Transparency of Graphene," Science, vol. 320, no. 5881, p. 1308, 2008.

[22]   S. Bae, H. Kim, Y. Lee, X. Xu, J.-S. Park, Y. Zheng, J. Balakrishnan, T. Lei, H. Ri Kim, Y. I. Song, Y.-J. Kim, K. S. Kim, B. Ozyilmaz, J.-H. Ahn, B. H. Hong, and S. Iijima, "Roll-to-roll production of 30-inch graphene films for transparent electrodes," Nat Nano, vol. 5, no. 8, pp. 574–578, Aug. 2010.

[23]   I. W. Frank, D. M. Tanenbaum, A. M. van der Zande, and P. L. McEuen, "Mechanical properties of suspended graphene sheets," Journal of Vacuum Science & Technology B, vol. 25, no. 6, pp. 2558–2561, 2007.

[24]   C. Lee, X. Wei, J. W. Kysar, and J. Hone, "Measurement of the Elastic Properties and Intrinsic Strength of Monolayer Graphene," Science, vol. 321, no. 5887, pp. 385–388, 2008.

[25]   K. S. Kim, Y. Zhao, H. Jang, S. Y. Lee, J. M. Kim, K..S. Kim, J.-H. Ahn, P. Kim, J.-Y. Choi, and B. H. Hong, "Large-scale pattern growth of graphene films for stretchable transparent electrodes," Nature, vol. 457, no. 7230, pp. 706–710, Feb. 2009.

[26]   F. Schwierz, "Graphene transistors," Nat Nano, vol. 5, no. 7, pp. 487–496, Jul. 2010.

[27]   Y.-M. Lin, K. A. Jenkins, A. Valdes-Garcia, J. P. Small, D. B. Farmer, and P. Avouris, "Operation of Graphene Transistors at Gigahertz Frequencies," Nano Lett., vol. 9, no. 1, pp. 422–426, Dec. 2008.

[28]   L. Liao, Y.-C. Lin, M. Bao, R. Cheng, J. Bai, Y. Liu, Y. Qu, K. L. Wang, Y. Huang, and X. Duan, "High-speed graphene transistors with a self-aligned nanowire gate," Nature, vol. 467, no. 7313, pp. 305–308, Sep. 2010.

[29]   Y.-M. Lin, A. Valdes-Garcia, S.-J. Han, D. B. Farmer, I. Meric, Y. Sun, Y. Wu, C. Dimitrakopoulos, A. Grill, P. Avouris, and K. A. Jenkins, "Wafer-Scale Graphene Integrated Circuit," Science, vol. 332, no. 6035, pp. 1294–1297, 2011.

[30]   G. Liu, W. Stillman, S. Rumyantsev, Q. Shao, M. Shur, and A. A. Balandin, "Low-frequency electronic noise in the double-gate single-layer graphene transistors," Applied Physics Letters, vol. 95, no. 3, p. -, 2009.

[31]   Y.-M. Lin, H.-Y. Chiu, K. . Jenkins, D. B. Farmer, P. Avouris, and A. Valdes-Garcia, "Dual-Gate Graphene FETs With f_T of 50 GHz," Electron Device Letters, IEEE, vol. 31, no. 1, pp. 68–70, Jan. 2010.

[32]   R. Cheng, J. Bai, L. Liao, H. Zhou, Y. Chen, L. Liu, Y.-C. Lin, S. Jiang, Y. Huang, and X. Duan, "High-frequency self-aligned graphene transistors with transferred gate stacks," Proceedings of the National Academy of Sciences, vol. 109, no. 29, pp. 11588–11592, 2012.

[33]   Y.-M. Lin, C. Dimitrakopoulos, K. A. Jenkins, D. B. Farmer, H.-Y. Chiu, A. Grill, and P. Avouris, "100-GHz Transistors from Wafer-Scale Epitaxial Graphene," Science, vol. 327, no. 5966, p. 662, 2010.

[34]   H. Wang, A. Hsu, K. K. Kim, J. Kong, and T. Palacios, "Gigahertz ambipolar frequency multiplier based on CVD graphene," in Electron Devices Meeting (IEDM), 2010 IEEE International, 2010, pp. 23.6.1–23.6.4.

[35]   T. Palacios, A. Hsu, and H. Wang, "Applications of graphene devices in RF communications," Communications Magazine, IEEE, vol. 48, no. 6, pp. 122–128, Jun. 2010.

[36]   H. Wang, A. Hsu, J. Wu, J. Kong, and T. Palacios, "Graphene-Based Ambipolar RF Mixers," Electron Device Letters, IEEE, vol. 31, no. 9, pp. 906–908, Sep. 2010.

[37]   J.-S. Moon, D. Curtis, M. Hu, D. Wong, C. McGuire, P. M. Campbell, G. Jernigan, J. L. Tedesco, B. VanMil, R. Myers-Ward, C. Eddy, and D. K. Gaskill, "Epitaxial-Graphene RF Field-Effect Transistors on Si-Face 6H-SiC Substrates," Electron Device Letters, IEEE, vol. 30, no. 6, pp. 650–652, Jun. 2009.

[38]   Y. Q. Wu, D. B. Farmer, A. Valdes-Garcia, W. J. Zhu, K. A. Jenkins, C. Dimitrakopoulos, P. Avouris, and Y.-M. Lin, "Record high RF performance for epitaxial graphene transistors," in Electron Devices Meeting (IEDM), 2011 IEEE International, 2011, pp. 23.8.1–23.8.3.

[39]   K. S. Novoselov, V. I. Fal[prime]ko, L. Colombo, P. R. Gellert, M. G. Schwab, and K. Kim, "A roadmap for graphene," Nature, vol. 490, no. 7419, pp. 192–200, Oct. 2012.

[40]   F. Bonaccorso, Z. Sun, T. Hasan, and A. C. Ferrari, "Graphene photonics and optoelectronics," Nat Photon, vol. 4, no. 9, pp. 611–622, Sep. 2010.

[41]   F. Wang, Y. Zhang, C. Tian, C. Girit, A. Zettl, M. Crommie, and Y. R. Shen, "Gate-Variable Optical Transitions in Graphene," Science, vol. 320, no. 5873, pp. 206–209, 2008.

[42]   M. Liu, X. Yin, E. Ulin-Avila, B. Geng, T. Zentgraf, L. Ju, F. Wang, and X. Zhang, "A graphene-based broadband optical modulator," Nature, vol. 474, no. 7349, pp. 64–67, Jun. 2011.

[43]   T. Mueller, F. Xia, and P. Avouris, "Graphene photodetectors for high-speed optical communications," Nat Photon, vol. 4, no. 5, pp. 297–301, May 2010.

[44]   J. Chen, M. Badioli, P. Alonso-Gonzalez, S. Thongrattanasiri, F. Huth, J. Osmond, M. Spasenovic, A. Centeno, A. Pesquera, P. Godignon, A. Zurutuza Elorza, N. Camara, F. J. G. de Abajo, R. Hillenbrand, and F. H. L. Koppens, "Optical nano-imaging of gate-tunable graphene plasmons," Nature, vol. 487, no. 7405, pp. 77–81, Jul. 2012.

[45]   F. Xia, T. Mueller, Y. Lin, A. Valdes-Garcia, and P. Avouris, "Ultrafast graphene photodetector," Nat Nano, vol. 4, no. 12, pp. 839–843, Dec. 2009.

[46]   B. Y. Zhang, T. Liu, B. Meng, X. Li, G. Liang, X. Hu, and Q. J. Wang, "Broadband high photoresponse from pure monolayer graphene photodetector," Nat Commun, vol. 4, p. 1811, May 2013.

[47]   M. Liu, X. Yin, and X. Zhang, "Double-Layer Graphene Optical Modulator," Nano Lett., vol. 12, no. 3, pp. 1482–1485, Feb. 2012.

[48]   X. Gan, R.-J. Shiue, Y. Gao, I. Meric, T. F. Heinz, K. Shepard, J. Hone, S. Assefa, and D. Englund, "Chip-integrated ultrafast graphene photodetector with high responsivity," Nat Photon, vol. 7, no. 11, pp. 883–887, Nov. 2013.

[49]   A. Pospischil, M. Humer, M. M. Furchi, D. Bachmann, R. Guider, T. Fromherz, and T. Mueller, "CMOS-compatible graphene photodetector covering all optical communication bands," Nat Photon, vol. 7, no. 11, pp. 892–896, Nov. 2013.

[50]   L. Ju, B. Geng, J. Horng, C. Girit, M. Martin, Z. Hao, H. A. Bechtel, X. Liang, A. Zettl, Y. R. Shen, and F. Wang, "Graphene plasmonics for tunable terahertz metamaterials," Nat Nano, vol. 6, no. 10, pp. 630–634, Oct. 2011.

[51]   F. H. L. Koppens, D. E. Chang, and F. J. García de Abajo, "Graphene Plasmonics: A Platform for Strong Light–Matter Interactions," Nano Lett., vol. 11, no. 8, pp. 3370–3377, Jul. 2011.

[52]   A. N. Grigorenko, M. Polini, and K. S. Novoselov, "Graphene plasmonics," Nat Photon, vol. 6, no. 11, pp. 749–758, Nov. 2012.

[53]   H. Yan, X. Li, B. Chandra, G. Tulevski, Y. Wu, M. Freitag, W. Zhu, P. Avouris, and F. Xia, "Tunable infrared plasmonic devices using graphene/insulator stacks," Nat Nano, vol. 7, no. 5, pp. 330–334, May 2012.

[54]   Z. Fei, A. S. Rodin, G. O. Andreev, W. Bao, A. S. McLeod, M. Wagner, L. M. Zhang, Z. Zhao, M. Thiemens, G. Dominguez, M. M. Fogler, A. H. C. Neto, C. N. Lau, F. Keilmann, and D. N. Basov, "Gate-tuning of graphene plasmons revealed by infrared nano-imaging," Nature, vol. 487, no. 7405, pp. 82–85, Jul. 2012.

[55]   Q. Bao and K. P. Loh, "Graphene Photonics, Plasmonics, and Broadband Optoelectronic Devices," ACS Nano, vol. 6, no. 5, pp. 3677–3694, Apr. 2012.

[56]   S. A. Maier, "Graphene plasmonics: All eyes on flatland," Nat Phys, vol. 8, no. 8, pp. 581–582, Aug. 2012.

[57]   X. Wang, L. Zhi, and K. Müllen, "Transparent, Conductive Graphene Electrodes for Dye-Sensitized Solar Cells," Nano Lett., vol. 8, no. 1, pp. 323–327, Dec. 2007.

[58]   X. Miao, S. Tongay, M. K. Petterson, K. Berke, A. G. Rinzler, B. R. Appleton, and A. F. Hebard, "High Efficiency Graphene Solar Cells by Chemical Doping," Nano Lett., vol. 12, no. 6, pp. 2745–2750, May 2012.

[59]   X. Li, H. Zhu, K. Wang, A. Cao, J. Wei, C. Li, Y. Jia, Z. Li, X. Li, and D. Wu, "Graphene-On-Silicon Schottky Junction Solar Cells," Advanced Materials, vol. 22, no. 25, pp. 2743–2748, 2010.

[60]   T. Feng, D. Xie, Y. Lin, H. Zhao, Y. Chen, H. Tian, T. Ren, X. Li, Z. Li, K. Wang, D. Wu, and H. Zhu, "Efficiency enhancement of graphene/silicon-pillar-array solar cells by HNO3 and PEDOT-PSS," Nanoscale, vol. 4, no. 6, pp. 2130–2133, 2012.

[61]   T. Feng, D. Xie, Y. Lin, Y. Zang, T. Ren, R. Song, H. Zhao, H. Tian, X. Li, H. Zhu, and L. Liu, "Graphene based Schottky junction solar cells on patterned silicon-pillar-array substrate," Applied Physics Letters, vol. 99, no. 23, p. -, 2011.

[62]   Y. Lin, X. Li, D. Xie, T. Feng, Y. Chen, R. Song, H. Tian, T. Ren, M. Zhong, K. Wang, and H. Zhu, "Graphene/semiconductor heterojunction solar cells with modulated antireflection and graphene work function," Energy Environ. Sci., vol. 6, no. 1, pp. 108–115, 2013.

[63]   C. X. Guo and C. M. Li, "A self-assembled hierarchical nanostructure comprising carbon spheres and graphene nanosheets for enhanced supercapacitor performance," Energy Environ. Sci., vol. 4, no. 11, pp. 4504–4507, 2011.

[64]   C. Liu, Z. Yu, D. Neff, A. Zhamu, and B. Z. Jang, "Graphene-Based Supercapacitor with an Ultrahigh Energy Density," Nano Lett., vol. 10, no. 12, pp. 4863–4868, Nov. 2010.

[65]   Y. Wang, Z. Shi, Y. Huang, Y. Ma, C. Wang, M. Chen, and Y. Chen, "Supercapacitor Devices Based on Graphene Materials," J. Phys. Chem. C, vol. 113, no. 30, pp. 13103–13107, Jul. 2009.

[66]   Y. Zhu, S. Murali, M. D. Stoller, K. J. Ganesh, W. Cai, P. J. Ferreira, A. Pirkle, R. M. Wallace, K. A. Cychosz, M. Thommes, D. Su, E. A. Stach, and R. S. Ruoff, "Carbon-Based Supercapacitors Produced by Activation of Graphene," Science, vol. 332, no. 6037, pp. 1537–1541, 2011.

[67]   J. S. Bunch, A. M. van der Zande, S. S. Verbridge, I. W. Frank, D. M. Tanenbaum, J. M. Parpia, H. G. Craighead, and P. L. McEuen, "Electromechanical Resonators from Graphene Sheets," Science, vol. 315, no. 5811, pp. 490–493, 2007.

[68]   EichlerA., MoserJ., ChasteJ., ZdrojekM., Wilson-RaeI., and BachtoldA., "Nonlinear damping in mechanical resonators made from carbon nanotubes and graphene," Nat Nano, vol. 6, no. 6, pp. 339–342, Jun. 2011.

[69]   C. Chen, S. Rosenblatt, K. I. Bolotin, W. Kalb, P. Kim, I. Kymissis, H. L. Stormer, T. F. Heinz, and J. Hone, "Performance of monolayer graphene nanomechanical resonators with electrical readout," Nat Nano, vol. 4, no. 12, pp. 861–867, Dec. 2009.

[70]   X. Xie, L. Qu, C. Zhou, Y. Li, J. Zhu, H. Bai, G. Shi, and L. Dai, "An Asymmetrically Surface-Modified Graphene Film Electrochemical Actuator," ACS Nano, vol. 4, no. 10, pp. 6050–6054, Sep. 2010.

[71]   S. Park, J. An, J. W. Suk, and R. S. Ruoff, "Graphene-Based Actuators," Small, vol. 6, no. 2, pp. 210–212, 2010.

[72]   H. J. Yoon, D. H. Jun, J. H. Yang, Z. Zhou, S. S. Yang, and M. M.-C. Cheng, "Carbon dioxide gas sensor using a graphene sheet," Sensors and Actuators B: Chemical, vol. 157, no. 1, pp. 310–313, Sep. 2011.

[73]   W. Li, X. Geng, Y. Guo, J. Rong, Y. Gong, L. Wu, X. Zhang, P. Li, J. Xu, G. Cheng, M. Sun, and L. Liu, "Reduced Graphene Oxide Electrically Contacted Graphene Sensor for Highly Sensitive Nitric Oxide Detection," ACS Nano, vol. 5, no. 9, pp. 6955–6961, Aug. 2011.

[74]   W. Wu, Z. Liu, L. A. Jauregui, Q. Yu, R. Pillai, H. Cao, J. Bao, Y. P. Chen, and S.-S. Pei, "Wafer-scale synthesis of graphene by chemical vapor deposition and its application in hydrogen sensing," Sensors and Actuators B: Chemical, vol. 150, no. 1, pp. 296–300, Sep. 2010.

[75]   P. K. Ang, W. Chen, A. T. S. Wee, and K. P. Loh, "Solution-Gated Epitaxial Graphene as pH Sensor," J. Am. Chem. Soc., vol. 130, no. 44, pp. 14392–14393, Oct. 2008.

[76]   X. Kang, J. Wang, H. Wu, J. Liu, I. A. Aksay, and Y. Lin, "A graphene-based electrochemical sensor for sensitive detection of paracetamol," Talanta, vol. 81, no. 3, pp. 754–759, May 2010.

[77]   Y. Dan, Y. Lu, N. J. Kybert, Z. Luo, and A. T. C. Johnson, "Intrinsic Response of Graphene Vapor Sensors," Nano Lett., vol. 9, no. 4, pp. 1472–1475, Mar. 2009.

[78]   M. Pumera, A. Ambrosi, A. Bonanni, E. L. K. Chng, and H. L. Poh, "Graphene for electrochemical sensing and biosensing," TrAC Trends in Analytical Chemistry, vol. 29, no. 9, pp. 954–965, Oct. 2010.

[79]   J. Luo, S. Jiang, H. Zhang, J. Jiang, and X. Liu, "A novel non-enzymatic glucose sensor based on Cu nanoparticle modified graphene sheets electrode," Analytica Chimica Acta, vol. 709, no. 0, pp. 47–53, Jan. 2012.

[80]   B. Mailly-Giacchetti, A. Hsu, H. Wang, V. Vinciguerra, F. Pappalardo, L. Occhipinti, E. Guidetti, S. Coffa, J. Kong, and T. Palacios, "pH sensing properties of graphene solution-gated field-effect transistors," Journal of Applied Physics, vol. 114, no. 8, p. -, 2013.

[81]   T. Ohta, A. Bostwick, T. Seyller, K. Horn, and E. Rotenberg, "Controlling the Electronic Structure of Bilayer Graphene," Science, vol. 313, no. 5789, pp. 951–954, 2006.

[82]   Y. Zhang, T.-T. Tang, C. Girit, Z. Hao, M. C. Martin, A. Zettl, M. F. Crommie, Y. R. Shen, and F. Wang, "Direct observation of a widely tunable bandgap in bilayer graphene," Nature, vol. 459, no. 7248, pp. 820–823, Jun. 2009.

[83]   E. V. Castro, K. S. Novoselov, S. V. Morozov, N. M. R. Peres, J. M. B. L. dos Santos, J. Nilsson, F. Guinea, A. K. Geim, and A. H. C. Neto, "Biased Bilayer Graphene:

Semiconductor with a Gap Tunable by the Electric Field Effect," Phys. Rev. Lett., vol. 99, no. 21, p. 216802, Nov. 2007.

[84] J. B. Oostinga, H. B. Heersche, X. Liu, A. F. Morpurgo, and L. M. K. Vandersypen, "Gate-induced insulating state in bilayer graphene devices," Nat Mater, vol. 7, no. 2, pp. 151–157, Feb. 2008.

[85] X. Li, X. Wang, L. Zhang, S. Lee, and H. Dai, "Chemically Derived, Ultrasmooth Graphene Nanoribbon Semiconductors," Science, vol. 319, no. 5867, pp. 1229–1232, 2008.

[86] X. Wang, Y. Ouyang, X. Li, H. Wang, J. Guo, and H. Dai, "Room-Temperature All-Semiconducting Sub-10-nm Graphene Nanoribbon Field-Effect Transistors," Phys. Rev. Lett., vol. 100, no. 20, p. 206803, May 2008.

[87] Q. Yan, B. Huang, J. Yu, F. Zheng, J. Zang, J. Wu, B.-L. Gu, F. Liu, and W. Duan, "Intrinsic Current−Voltage Characteristics of Graphene Nanoribbon Transistors and Effect of Edge Doping," Nano Lett., vol. 7, no. 6, pp. 1469–1473, Apr. 2007.

[88] K. F. Mak, C. Lee, J. Hone, J. Shan, and T. F. Heinz, "Atomically Thin MoS2: A New Direct-Gap Semiconductor," Phys. Rev. Lett., vol. 105, no. 13, p. 136805, Sep. 2010.

[89] G. Eda, H. Yamaguchi, D. Voiry, T. Fujita, M. Chen, and M. Chhowalla, "Photoluminescence from Chemically Exfoliated MoS2," Nano Lett., vol. 11, no. 12, pp. 5111–5116, Oct. 2011.

[90] RadisavljevicB., RadenovicA., BrivioJ., GiacomettiV., and KisA., "Single-layer MoS2 transistors," Nat Nano, vol. 6, no. 3, pp. 147–150, Mar. 2011.

[91] Y. Yoon, K. Ganapathi, and S. Salahuddin, "How Good Can Monolayer MoS2 Transistors Be?," Nano Lett., vol. 11, no. 9, pp. 3768–3773, Jul. 2011.

[92] L. Liu, S. Bala Kumar, Y. Ouyang, and J. Guo, "Performance Limits of Monolayer Transition Metal Dichalcogenide Transistors," Electron Devices, IEEE Transactions on, vol. 58, no. 9, pp. 3042–3047, Sep. 2011.

[93] H. Liu, A. T. Neal, and P. D. Ye, "Channel Length Scaling of MoS2 MOSFETs," ACS Nano, vol. 6, no. 10, pp. 8563–8569, Sep. 2012.

[94] G.-H. Lee, Y.-J. Yu, X. Cui, N. Petrone, C.-H. Lee, M. S. Choi, D.-Y. Lee, C. Lee, W. J. Yoo, K. Watanabe, T. Taniguchi, C. Nuckolls, P. Kim, and J. Hone, "Flexible

and Transparent MoS2 Field-Effect Transistors on Hexagonal Boron Nitride-Graphene Heterostructures," ACS Nano, vol. 7, no. 9, pp. 7931–7936, Aug. 2013.

[95]   D. Lembke and A. Kis, "Breakdown of High-Performance Monolayer MoS2 Transistors," ACS Nano, vol. 6, no. 11, pp. 10070–10075, Oct. 2012.

[96]   A. Dankert, L. Langouche, M. V. Kamalakar, and S. P. Dash, "High-Performance Molybdenum Disulfide Field-Effect Transistors with Spin Tunnel Contacts," ACS Nano, vol. 8, no. 1, pp. 476–482, Dec. 2013.

[97]   S. Das, H.-Y. Chen, A. V. Penumatcha, and J. Appenzeller, "High Performance Multilayer MoS2 Transistors with Scandium Contacts," Nano Lett., vol. 13, no. 1, pp. 100–105, Dec. 2012.

[98]   S. Ghatak, A. N. Pal, and A. Ghosh, "Nature of Electronic States in Atomically Thin MoS2 Field-Effect Transistors," ACS Nano, vol. 5, no. 10, pp. 7707–7712, Sep. 2011.

[99]   S. Kim, A. Konar, W.-S. Hwang, J. H. Lee, J. Lee, J. Yang, C. Jung, H. Kim, J.-B. Yoo, J.-Y. Choi, Y. W. Jin, S. Y. Lee, D. Jena, W. Choi, and K. Kim, "High-mobility and low-power thin-film transistors based on multilayer MoS2 crystals," Nat Commun, vol. 3, p. 1011, Aug. 2012.

[100]   J. Pu, Y. Yomogida, K.-K. Liu, L.-J. Li, Y. Iwasa, and T. Takenobu, "Highly Flexible MoS2 Thin-Film Transistors with Ion Gel Dielectrics," Nano Lett., vol. 12, no. 8, pp. 4013–4017, Jul. 2012.

[101]   X. Zou, J. Wang, C.-H. Chiu, Y. Wu, X. Xiao, C. Jiang, W.-W. Wu, L. Mai, T. Chen, J. Li, J. C. Ho, and L. Liao, "Interface Engineering for High-Performance Top-Gated MoS2 Field-Effect Transistors," Advanced Materials, p. n/a–n/a, 2014.

[102]   J. Yoon, W. Park, G.-Y. Bae, Y. Kim, H. S. Jang, Y. Hyun, S. K. Lim, Y. H. Kahng, W.-K. Hong, B. H. Lee, and H. C. Ko, "Highly Flexible and Transparent Multilayer MoS2 Transistors with Graphene Electrodes," Small, vol. 9, no. 19, pp. 3295–3300, 2013.

[103]   B. Radisavljevic, M. B. Whitwick, and A. Kis, "Integrated Circuits and Logic Operations Based on Single-Layer MoS2," ACS Nano, vol. 5, no. 12, pp. 9934–9938, Nov. 2011.

[104]   H. Wang, L. Yu, Y.-H. Lee, Y. Shi, A. Hsu, M. L. Chin, L.-J. Li, M. Dubey, J. Kong, and T. Palacios, "Integrated Circuits Based on Bilayer MoS2 Transistors," Nano Lett., vol. 12, no. 9, pp. 4674–4680, Aug. 2012.

[105]   L. Yu, Y.-H. Lee, X. Ling, E. J. G. Santos, Y. C. Shin, Y. Lin, M. Dubey, E. Kaxiras, J. Kong, H. Wang, and T. Palacios, "Graphene/MoS2 Hybrid Technology for Large-Scale Two-Dimensional Electronics," Nano Lett., vol. 14, no. 6, pp. 3055–3063, May 2014.

[106]   H. Liu, M. Si, S. Najmaei, A. T. Neal, Y. Du, P. M. Ajayan, J. Lou, and P. D. Ye, "Statistical Study of Deep Submicron Dual-Gated Field-Effect Transistors on Monolayer Chemical Vapor Deposition Molybdenum Disulfide Films," Nano Lett., vol. 13, no. 6, pp. 2640–2646, May 2013.

[107]   W. Zhu, T. Low, Y.-H. Lee, H. Wang, D. B. Farmer, J. Kong, F. Xia, and P. Avouris, "Electronic transport and device prospects of monolayer molybdenum disulphide grown by chemical vapour deposition," Nat Commun, vol. 5, Jan. 2014.

[108]   S. Najmaei, M. Amani, M. L. Chin, Z. Liu, A. G. Birdwell, T. P. O'Regan, P. M. Ajayan, M. Dubey, and J. Lou, "Electrical Transport Properties of Polycrystalline Monolayer Molybdenum Disulfide," ACS Nano, vol. 8, no. 8, pp. 7930–7937, Jul. 2014.

[109]   T. Roy, M. Tosun, J. S. Kang, A. B. Sachid, S. B. Desai, M. Hettick, C. C. Hu, and A. Javey, "Field-Effect Transistors Built from All Two-Dimensional Material Components," ACS Nano, vol. 8, no. 6, pp. 6259–6264, Apr. 2014.

[110]   W. Choi, M. Y. Cho, A. Konar, J. H. Lee, G.-B. Cha, S. C. Hong, S. Kim, J. Kim, D. Jena, J. Joo, and S. Kim, "High-Detectivity Multilayer MoS2 Phototransistors with Spectral Response from Ultraviolet to Infrared," Advanced Materials, vol. 24, no. 43, pp. 5832–5836, 2012.

[111]   Z. Yin, H. Li, H. Li, L. Jiang, Y. Shi, Y. Sun, G. Lu, Q. Zhang, X. Chen, and H. Zhang, "Single-Layer MoS2 Phototransistors," ACS Nano, vol. 6, no. 1, pp. 74–80, Dec. 2011.

[112]   H. S. Lee, S.-W. Min, Y.-G. Chang, M. K. Park, T. Nam, H. Kim, J. H. Kim, S. Ryu, and S. Im, "MoS2 Nanosheet Phototransistors with Thickness-Modulated Optical Energy Gap," Nano Lett., vol. 12, no. 7, pp. 3695–3700, Jun. 2012.

[113] O. Lopez-Sanchez, D. Lembke, M. Kayci, A. Radenovic, and A. Kis, "Ultrasensitive photodetectors based on monolayer MoS2," Nat Nano, vol. 8, no. 7, pp. 497–501, Jul. 2013.

[114] W. Choi, M. Y. Cho, A. Konar, J. H. Lee, G.-B. Cha, S. C. Hong, S. Kim, J. Kim, D. Jena, J. Joo, and S. Kim, "High-Detectivity Multilayer MoS2 Phototransistors with Spectral Response from Ultraviolet to Infrared," Advanced Materials, vol. 24, no. 43, pp. 5832–5836, 2012.

[115] M. Buscema, M. Barkelid, V. Zwiller, H. S. J. van der Zant, G. A. Steele, and A. Castellanos-Gomez, "Large and Tunable Photothermoelectric Effect in Single-Layer MoS2," Nano Lett., vol. 13, no. 2, pp. 358–363, Jan. 2013.

[116] W. Zhang, J.-K. Huang, C.-H. Chen, Y.-H. Chang, Y.-J. Cheng, and L.-J. Li, "High-Gain Phototransistors Based on a CVD MoS2 Monolayer," Advanced Materials, vol. 25, no. 25, pp. 3456–3461, 2013.

[117] K. Roy, M. Padmanabhan, S. Goswami, T. P. Sai, G. Ramalingam, S. Raghavan, and A. Ghosh, "Graphene-MoS2 hybrid structures for multifunctional photoresponsive memory devices," Nat Nano, vol. 8, no. 11, pp. 826–830, Nov. 2013.

[118] W. Zhang, C.-P. Chuu, J.-K. Huang, C.-H. Chen, M.-L. Tsai, Y.-H. Chang, C.-T. Liang, Y.-Z. Chen, Y.-L. Chueh, J.-H. He, M.-Y. Chou, and L.-J. Li, "Ultrahigh-Gain Photodetectors Based on Atomically Thin Graphene-MoS2 Heterostructures," Sci. Rep., vol. 4, Jan. 2014.

[119] N. Perea-López, A. L. Elías, A. Berkdemir, A. Castro-Beltran, H. R. Gutiérrez, S. Feng, R. Lv, T. Hayashi, F. López-Urías, S. Ghosh, B. Muchharla, S. Talapatra, H. Terrones, and M. Terrones, "Photosensor Device Based on Few-Layered WS2 Films," Advanced Functional Materials, vol. 23, no. 44, pp. 5511–5517, 2013.

[120] R. S. Sundaram, M. Engel, A. Lombardo, R. Krupke, A. C. Ferrari, P. Avouris, and M. Steiner, "Electroluminescence in Single Layer MoS2," Nano Lett., vol. 13, no. 4, pp. 1416–1421, Mar. 2013.

[121] R. Cheng, D. Li, H. Zhou, C. Wnag, A. yin, S. Jiang, Y. Liu, Y. Huang, and X. Duan, "Electroluminescence and photocurrent generation from atomically sharp WSe2/MoS2 heterojunction p-n diodes," arXiv:1403.3447 [cond-mat.mes-hall], Mar 2014.

[122]   C.-H. Lee, G.-H. Lee, A. M. van der Zande, W. Chen, Y. Li, M. Han, X. Cui, G. Arefe, C. Nuckolls, T. F. Heinz, J. Guo, J. Hone, and P. Kim, "Atomically thin p–n junctions with van der Waals heterointerfaces," Nat Nano, vol. advance online publication, Aug. 2014.

[123]   M. M. Furchi, A. Pospischil, F. Libisch, J. Burgdörfer, and T. Mueller, "Photovoltaic Effect in an Electrically Tunable van der Waals Heterojunction," Nano Lett., vol. 14, no. 8, pp. 4785–4791, Jul. 2014.

[124]   O. Lopez-Sanchez, E. Alarcon Llado, V. Koman, A. Fontcuberta i Morral, A. Radenovic, and A. Kis, "Light Generation and Harvesting in a van der Waals Heterostructure," ACS Nano, vol. 8, no. 3, pp. 3042–3048, Mar. 2014.

[125]   P. Rivera, J. R. Schaibley, A. M. Jones, J. S. Ross, S. Wu, G. Aivazian, P. Klement, N. J. Ghimire, J. Yan, D. G. Mandrus, W. Yao, and X. Xu, "Observation of long-lived interlayer excitons in monolayer MoSe2-WSe2 heterostructures," arXiv:1403.4985 [cond-mat.mes-hall], Mar. 2014.

[126]   B. W. H. Baugher, H. O. H. Churchill, Y. Yang, and P. Jarillo-Herrero, "Optoelectronic devices based on electrically tunable p-n diodes in a monolayer dichalcogenide," Nat Nano, vol. 9, no. 4, pp. 262–267, Apr. 2014.

[127]   A. Pospischil, M. M. Furchi, and T. Mueller, "Solar-energy conversion and light emission in an atomic monolayer p-n diode," Nat Nano, vol. 9, no. 4, pp. 257–261, Apr. 2014.

[128]   J. S. Ross, P. Klement, A. M. Jones, N. J. Ghimire, J. Yan, MandrusD. G., T. Taniguchi, K. Watanabe, K. Kitamura, W. Yao, D. H. Cobden, and X. Xu, "Electrically tunable excitonic light-emitting diodes based on monolayer WSe2 p-n junctions," Nat Nano, vol. 9, no. 4, pp. 268–272, Apr. 2014.

[129]   Y. J. Zhang, T. Oka, R. Suzuki, J. T. Ye, and Y. Iwasa, "Electrically Switchable Chiral Light-Emitting Transistor," Science, vol. 344, no. 6185, pp. 725–728, 2014.

[130]   M.-L. Tsai, S.-H. Su, J.-K. Chang, D.-S. Tsai, C.-H. Chen, C.-I. Wu, L.-J. Li, L.-J. Chen, and J.-H. He, "Monolayer MoS2 Heterojunction Solar Cells," ACS Nano, vol. 8, no. 8, pp. 8317–8322, Jul. 2014.

[131]   D. Jariwala, V. K. Sangwan, C.-C. Wu, P. L. Prabhumirashi, M. L. Geier, T. J. Marks, L. J. Lauhon, and M. C. Hersam, "Gate-tunable carbon nanotube–MoS2

heterojunction p-n diode," Proceedings of the National Academy of Sciences, vol. 110, no. 45, pp. 18076–18080, 2013.

[132]   S. Wu, C. Huang, G. Aivazian, J. S. Ross, D. H. Cobden, and X. Xu, "Vapor–Solid Growth of High Optical Quality MoS2 Monolayers with Near-Unity Valley Polarization," ACS Nano, vol. 7, no. 3, pp. 2768–2772, Feb. 2013.

[133]   Y.-H. Lee, X.-Q. Zhang, W. Zhang, M.-T. Chang, C.-T. Lin, K.-D. Chang, Y.-C. Yu, J. T.-W. Wang, C.-S. Chang, L.-J. Li, and T.-W. Lin, "Synthesis of Large-Area MoS2 Atomic Layers with Chemical Vapor Deposition," Advanced Materials, vol. 24, no. 17, pp. 2320–2325, 2012.

[134]   Y.-H. Lee, L. Yu, H. Wang, W. Fang, X. Ling, Y. Shi, C.-T. Lin, J.-K. Huang, M.-T. Chang, C.-S. Chang, M. Dresselhaus, T. Palacios, L.-J. Li, and J. Kong, "Synthesis and Transfer of Single-Layer Transition Metal Disulfides on Diverse Surfaces," Nano Lett., vol. 13, no. 4, pp. 1852–1857, Mar. 2013.

[135]   Y. Shi, W. Zhou, A.-Y. Lu, W. Fang, Y.-H. Lee, A. L. Hsu, S. M. Kim, K. K. Kim, H. Y. Yang, L.-J. Li, J.-C. Idrobo, and J. Kong, "van der Waals Epitaxy of MoS2 Layers Using Graphene As Growth Templates," Nano Lett., vol. 12, no. 6, pp. 2784–2791, May 2012.

[136]   X. Wang, H. Feng, Y. Wu, and L. Jiao, "Controlled Synthesis of Highly Crystalline MoS2 Flakes by Chemical Vapor Deposition," J. Am. Chem. Soc., vol. 135, no. 14, pp. 5304–5307, Mar. 2013.

[137]   X. Ling, Y.-H. Lee, Y. Lin, W. Fang, L. Yu, M. S. Dresselhaus, and J. Kong, "Role of the Seeding Promoter in MoS2 Growth by Chemical Vapor Deposition," Nano Lett., vol. 14, no. 2, pp. 464–472, Jan. 2014.

[138]   Y. Zhan, Z. Liu, S. Najmaei, P. M. Ajayan, and J. Lou, "Large-Area Vapor-Phase Growth and Characterization of MoS2 Atomic Layers on a SiO2 Substrate," Small, vol. 8, no. 7, pp. 966–971, 2012.

[139]   Y. Yu, C. Li, Y. Liu, L. Su, Y. Zhang, and L. Cao, "Controlled Scalable Synthesis of Uniform, High-Quality Monolayer and Few-layer MoS2 Films," Sci. Rep., vol. 3, May 2013.

[140] X. Wang, Y. Gong, G. Shi, W. L. Chow, K. Keyshar, G. Ye, R. Vajtai, J. Lou, Z. Liu, E. Ringe, B. K. Tay, and P. M. Ajayan, "Chemical Vapor Deposition Growth of Crystalline Monolayer MoSe2," ACS Nano, vol. 8, no. 5, pp. 5125–5131, Mar. 2014.

[141] M. Okada, T. Sawazaki, K. Watanabe, T. Taniguch, H. Hibino, H. Shinohara, and R. Kitaura, "Direct Chemical Vapor Deposition Growth of WS2 Atomic Layers on Hexagonal Boron Nitride," ACS Nano, vol. 8, no. 8, pp. 8273–8277, Aug. 2014.

[142] J.-K. Huang, J. Pu, C.-L. Hsu, M.-H. Chiu, Z.-Y. Juang, Y.-H. Chang, W.-H. Chang, Y. Iwasa, T. Takenobu, and L.-J. Li, "Large-Area Synthesis of Highly Crystalline WSe2 Monolayers and Device Applications," ACS Nano, vol. 8, no. 1, pp. 923–930, Dec. 2013.

[143] C. Lee, H. Yan, L. E. Brus, T. F. Heinz, J. Hone, and S. Ryu, "Anomalous Lattice Vibrations of Single- and Few-Layer MoS2," ACS Nano, vol. 4, no. 5, pp. 2695–2700, Apr. 2010.

[144] G. Berghäuser and E. Malic, "Analytical approach to excitonic properties of MoS2," Phys. Rev. B, vol. 89, no. 12, p. 125309, Mar. 2014.

[145] A. Ramasubramaniam, "Large excitonic effects in monolayers of molybdenum and tungsten dichalcogenides," Phys. Rev. B, vol. 86, no. 11, p. 115409, Sep. 2012.

[146] F. Hüser, T. Olsen, and K. S. Thygesen, "How dielectric screening in two-dimensional crystals affects the convergence of excited-state calculations: Monolayer MoS2," Phys. Rev. B, vol. 88, no. 24, p. 245309, Dec. 2013.

[147] T. Cheiwchanchamnangij and W. R. L. Lambrecht, "Quasiparticle band structure calculation of monolayer, bilayer, and bulk MoS2," Phys. Rev. B, vol. 85, no. 20, p. 205302, May 2012.

[148] D. Y. Qiu, F. H. da Jornada, and S. G. Louie, "Optical Spectrum of MoS2: Many-Body Effects and Diversity of Exciton States," Phys. Rev. Lett., vol. 111, no. 21, p. 216805, Nov. 2013.

[149] A. Molina-Sánchez, D. Sangalli, K. Hummer, A. Marini, and L. Wirtz, "Effect of spin-orbit interaction on the optical spectra of single-layer, double-layer, and bulk MoS2," Phys. Rev. B, vol. 88, no. 4, p. 045412, Jul. 2013.

[150]   T. C. Berkelbach, M. S. Hybertsen, and D. R. Reichman, "Theory of neutral and charged excitons in monolayer transition metal dichalcogenides," Phys. Rev. B, vol. 88, no. 4, p. 045318, Jul. 2013.

[151]   H.-P. Komsa and A. V. Krasheninnikov, "Effects of confinement and environment on the electronic structure and exciton binding energy of MoS2 from first principles," Phys. Rev. B, vol. 86, no. 24, p. 241201, Dec. 2012.

[152]   J. Feng, X. Qian, C.-W. Huang, and J. Li, "Strain-engineered artificial atom as a broad-spectrum solar energy funnel," Nat Photon, vol. 6, no. 12, pp. 866–872, Dec. 2012.

[153]   K. F. Mak, K. He, C. Lee, G. H. Lee, J. Hone, T. F. Heinz, and J. Shan, "Tightly bound trions in monolayer MoS2," Nat Mater, vol. 12, no. 3, pp. 207–211, Mar. 2013.

[154]   J. S. Ross, S. Wu, H. Yu, N. J. Ghimire, A. M. Jones, G. Aivazian, J. Yan, D. G. Mandrus, D. Xiao, W. Yao, and X. Xu, "Electrical control of neutral and charged excitons in a monolayer semiconductor," Nat Commun, vol. 4, p. 1474, Feb. 2013.

[155]   K. He, N. Kumar, L. Zhao, Z. Wang, K. F. Mak, H. Zhao, and J. Shan, "Tightly Bound Excitons in Monolayer WSe2," Phys. Rev. Lett., vol. 113, no. 2, p. 026803, Jul. 2014.

[156]   A. Chernikov, T. C. Berkelbach, H. M. Hill, A. Rigosi, Y. Li, O. B. Aslan, D. R. Reichman, M. S. Hybertsen, and T. F. Heinz, "Exciton Binding Energy and Nonhydrogenic Rydberg Series in Monolayer WS2," Phys. Rev. Lett., vol. 113, no. 7, p. 076802, Aug. 2014.

[157]   E. J. Sie, Y.-H. Lee, A. J. Frenzel, J. Kong, and N. Gedik, "Biexciton formation in monolayer MoS2 observed by transient absorption spectroscopy," arXiv:1312.2918 [cond-mat.mes-hall], Dec. 2013.

[158]   K. F. Mak, K. He, J. Shan, and T. F. Heinz, "Control of valley polarization in monolayer MoS2 by optical helicity," Nat Nano, vol. 7, no. 8, pp. 494–498, Aug. 2012.

[159]   H. Zeng, J. Dai, W. Yao, D. Xiao, and X. Cui, "Valley polarization in MoS2 monolayers by optical pumping," Nat Nano, vol. 7, no. 8, pp. 490–493, Aug. 2012.

[160]   T. Cao, G. Wang, W. Han, H. Ye, C. Zhu, J. Shi, Q. Niu, P. Tan, E. Wang, B. Liu, and J. Feng, "Valley-selective circular dichroism of monolayer molybdenum disulphide," Nat Commun, vol. 3, p. 887, Jun. 2012.

[161] S. Wu, J. S. Ross, G.-B. Liu, G. Aivazian, A. Jones, Z. Fei, W. Zhu, D. Xiao, W. Yao, D. Cobden, and X. Xu, "Electrical tuning of valley magnetic moment through symmetry control in bilayer MoS2," Nat Phys, vol. 9, no. 3, pp. 149–153, Mar. 2013.

[162] K. F. Mak, K. L. McGill, J. Park, and P. L. McEuen, "The valley Hall effect in MoS2 transistors," Science, vol. 344, no. 6191, pp. 1489–1492, 2014.

[163] F. K. Perkins, A. L. Friedman, E. Cobas, P. M. Campbell, G. G. Jernigan, and B. T. Jonker, "Chemical Vapor Sensing with Monolayer MoS2," Nano Lett., vol. 13, no. 2, pp. 668–673, Jan. 2013.

[164] D. J. Late, Y.-K. Huang, B. Liu, J. Acharya, S. N. Shirodkar, J. Luo, A. Yan, D. Charles, U. V. Waghmare, V. P. Dravid, and C. N. R. Rao, "Sensing Behavior of Atomically Thin-Layered MoS2 Transistors," ACS Nano, vol. 7, no. 6, pp. 4879–4891, May 2013.

[165] H. Li, Z. Yin, Q. He, H. Li, X. Huang, G. Lu, D. W. H. Fam, A. I. Y. Tok, Q. Zhang, and H. Zhang, "Fabrication of Single- and Multilayer MoS2 Film-Based Field-Effect Transistors for Sensing NO at Room Temperature," Small, vol. 8, no. 1, pp. 63–67, 2012.

[166] Q. He, Z. Zeng, Z. Yin, H. Li, S. Wu, X. Huang, and H. Zhang, "Fabrication of Flexible MoS2 Thin-Film Transistor Arrays for Practical Gas-Sensing Applications," Small, vol. 8, no. 19, pp. 2994–2999, 2012.

[167] C. Zhu, Z. Zeng, H. Li, F. Li, C. Fan, and H. Zhang, "Single-Layer MoS2-Based Nanoprobes for Homogeneous Detection of Biomolecules," J. Am. Chem. Soc., vol. 135, no. 16, pp. 5998–6001, Apr. 2013.

[168] S. Stankovich, D. A. Dikin, G. H. B. Dommett, K. M. Kohlhaas, E. J. Zimney, E. A. Stach, R. D. Piner, S. T. Nguyen, and R. S. Ruoff, "Graphene-based composite materials," Nature, vol. 442, no. 7100, pp. 282–286, Jul. 2006.

[169] P. Vogt, P. De Padova, C. Quaresima, J. Avila, E. Frantzeskakis, M. C. Asensio, A. Resta, B. Ealet, and G. Le Lay, "Silicene: Compelling Experimental Evidence for Graphenelike Two-Dimensional Silicon," Phys. Rev. Lett., vol. 108, no. 15, p. 155501, Apr. 2012.

[170] B. Lalmi, H. Oughaddou, H. Enriquez, A. Kara, S. Vizzini, B. Ealet, and B. Aufray, "Epitaxial growth of a silicene sheet," Applied Physics Letters, vol. 97, no. 22, p. -, 2010.

[171] C.-C. Liu, W. Feng, and Y. Yao, "Quantum Spin Hall Effect in Silicene and Two-Dimensional Germanium," Phys. Rev. Lett., vol. 107, no. 7, p. 076802, Aug. 2011.

[172] A. Fleurence, R. Friedlein, T. Ozaki, H. Kawai, Y. Wang, and Y. Yamada-Takamura, "Experimental Evidence for Epitaxial Silicene on Diboride Thin Films," Phys. Rev. Lett., vol. 108, no. 24, p. 245501, Jun. 2012.

[173] Z. Ni, Q. Liu, K. Tang, J. Zheng, J. Zhou, R. Qin, Z. Gao, D. Yu, and J. Lu, "Tunable Bandgap in Silicene and Germanene," Nano Lett., vol. 12, no. 1, pp. 113–118, Nov. 2011.

[174] M. Houssa, E. Scalise, K. Sankaran, G. Pourtois, V. V. Afanas'ev, and A. Stesmans, "Electronic properties of hydrogenated silicene and germanene," Applied Physics Letters, vol. 98, no. 22, p. -, 2011.

[175] A. O' Hare, F. V. Kusmartsev, and K. I. Kugel, "A Stable "Flat" Form of Two-Dimensional Crystals: Could Graphene, Silicene, Germanene Be Minigap Semiconductors?," Nano Lett., vol. 12, no. 2, pp. 1045-1052, Jan. 2012.

[176] V. Nicolosi, M. Chhowalla, M. G. Kanatzidis, M. S. Strano, and J. N. Coleman, "Liquid Exfoliation of Layered Materials," Science, vol. 340, no. 6139, 2013.

[177] J. Qiao, X. Kong, Z.-X. Hu, F. Yang, and W. Ji, "High-mobility transport anisotropy and linear dichroism in few-layer black phosphorus," Nat Commun, vol. 5, Jul. 2014.

[178] L. Li, Y. Yu, G. J. Ye, Q. Ge, X. Ou, H. Wu, D. Feng, X. H. Chen, and Y. Zhang, "Black phosphorus field-effect transistors," Nat Nano, vol. 9, no. 5, pp. 372–377, May 2014.

[179] A. S. Rodin, A. Carvalho, and A. H. Castro Neto, "Strain-Induced Gap Modification in Black Phosphorus," Phys. Rev. Lett., vol. 112, no. 17, p. 176801, May 2014.

[180] S. P. Koenig, R. A. Doganov, H. Schmidt, A. H. Castro Neto, and B. Özyilmaz, "Electric field effect in ultrathin black phosphorus," Applied Physics Letters, vol. 104, no. 10, p. -, 2014.

[181] V. Tran, R. Soklaski, Y. Liang, and L. Yang, "Layer-controlled band gap and anisotropic excitons in few-layer black phosphorus," Phys. Rev. B, vol. 89, no. 23, p. 235319, Jun. 2014.

[182] F. Xia, H. Wang, and Y. Jia, "Rediscovering black phosphorus as an anisotropic layered material for optoelectronics and electronics," Nat Commun, vol. 5, Jul. 2014.

[183] J. Y. Kwak, J. Hwang, B. Calderon, H. Alsalman, N. Munoz, B. Schutter, and M. G. Spencer, "Electrical Characteristics of Multilayer MoS2 FET's with MoS2/Graphene Heterojunction Contacts," Nano Lett., vol. 14, no. 8, pp. 4511–4516, Jun. 2014.

[184] C.-J. Shih, Q. H. Wang, Y. Son, Z. Jin, D. Blankschtein, and M. S. Strano, "Tuning On–Off Current Ratio and Field-Effect Mobility in a MoS2–Graphene Heterostructure via Schottky Barrier Modulation," ACS Nano, vol. 8, no. 6, pp. 5790–5798, May 2014.

[185] DeanC. R., YoungA. F., MericI., LeeC., WangL., SorgenfreiS., WatanabeK., TaniguchiT., KimP., ShepardK. L., and HoneJ., "Boron nitride substrates for high-quality graphene electronics," Nat Nano, vol. 5, no. 10, pp. 722–726, Oct. 2010.

[186] Z. Liu, L. Song, S. Zhao, J. Huang, L. Ma, J. Zhang, J. Lou, and P. M. Ajayan, "Direct Growth of Graphene/Hexagonal Boron Nitride Stacked Layers," Nano Lett., vol. 11, no. 5, pp. 2032–2037, Apr. 2011.

[187] M. P. Levendorf, C.-J. Kim, L. Brown, P. Y. Huang, R. W. Havener, D. A. Muller, and J. Park, "Graphene and boron nitride lateral heterostructures for atomically thin circuitry," Nature, vol. 488, no. 7413, pp. 627–632, Aug. 2012.

[188] Z. Liu, L. Ma, G. Shi, W. Zhou, Y. Gong, S. Lei, X. Yang, J. Zhang, J. Yu, K. P. Hackenberg, A. Babakhani, J.-C. Idrobo, R. Vajtai, J. Lou, and P. M. Ajayan, "In-plane heterostructures of graphene and hexagonal boron nitride with controlled domain sizes," Nat Nano, vol. 8, no. 2, pp. 119–124, Feb. 2013.

[189] M. Chhowalla, H. S. Shin, G. Eda, L.-J. Li, K. P. Loh, and H. Zhang, "The chemistry of two-dimensional layered transition metal dichalcogenide nanosheets," Nat. Chem., vol. 5, no. 4, pp. 263–275, Apr. 2013

[190] Q. H. Wang, K. Kalantar-Zadeh, A. Kis, J. N. Coleman, and M. S. Strano, "Electronics and optoelectronics of two-dimensional transition metal dichalcogenides," Nat. Nano., vol. 7, no. 11, pp. 699–712, Nov. 2012

[191]   J. A. Wilson, and A. D. Yoffe, " The transition metal dichalcogenides discussion and interpretation of the observed optical, electrical and structural properties," Advances in Physics, vol. 18, no. 73, pp. 193–335, 1969

[192]   W. Jin, P.-C. Yeh, N. Zaki, D. Zhang, J. T. Sadowski, A. Al-Mahboob, A. M. van der Zande, D. A. Chenet, J. I. Dadap, I. P. Herman, P. Sutter, J. Hone, and R. M. Osgood, "Direct Measurement of the Thickness-Dependent Electronic Band Structure of MoS2 Using Angle-Resolved Photoemission Spectroscopy," Phys. Rev. Lett., vol. 111, no. 10, p. 106801, Sep. 2013.

[193]   Y. Zhang, T.-R. Chang, B. Zhou, Y.-T. Cui, H. Yan, Z. Liu, F. Schmitt, J. Lee, R. Moore, Y. Chen, H. Lin, H.-T. Jeng, S.-K. Mo, Z. Hussain, A. Bansil, and Z.-X. Shen, "Direct observation of the transition from indirect to direct bandgap in atomically thin epitaxial MoSe2," Nat Nano, vol. 9, no. 2, pp. 111–115, Feb. 2014.

[194]   C.-P. Lu, G. Li, J. Mao, L.-M. Wang, and E. Y. Andrei, "Bandgap, Mid-Gap States, and Gating Effects in MoS2," Nano Lett., vol. 14, no. 8, pp. 4628–4633, Jul. 2014.

[195]   J. Dai, E. Calleja, J. Alldredge, X. Zhu, L. Li, W. Lu, Y. Sun, T. Wolf, H. Berger, and K. McElroy, "Microscopic evidence for strong periodic lattice distortion in two-dimensional charge-density wave systems," Phys. Rev. B, vol. 89, no. 16, p. 165140, Apr. 2014.

[196]   M. M. Ugeda, A. J. Bradley, S.-F. Shi, F. H. da Jornada, Y. Zhang, D. Y. Qiu, S.-K. Mo, Z. Hussain, Z.-X. Shen, F. Wang, S. G. Louie, and M. F. Crommie, "Observation of giant bandgap renormalization and excitonic effects in an monolayer transition metal dichalcogenide semiconductor," arXiv:1404.2331 [cond-mat.mes-hall], Apr. 2014.

[197]   H. Wang, L. Yu, Y. Lee, W. Fang, A. Hsu, P. Herring, M. Chin, M. Dubey, L. Li, J. Kong, and T. Palacios, "Large-scale 2D electronics based on single-layer MoS2 grown by chemical vapor deposition," in Electron Devices Meeting (IEDM), 2012 IEEE International, 2012, pp. 4.6.1–4.6.4.

[198]   A. Allain and A. Kis, "Electron and Hole Mobilities in Single-Layer WSe2," ACS Nano, vol. 8, no. 7, pp. 7180–7185, Jun. 2014.

[199]   H.-J. Chuang, X. Tan, N. J. Ghimire, M. M. Perera, B. Chamlagain, M. M.-C. Cheng, J. Yan, D. Mandrus, D. Tománek, and Z. Zhou, "High Mobility WSe2 p- and n-

Type Field-Effect Transistors Contacted by Highly Doped Graphene for Low-Resistance Contacts," Nano Lett., vol. 14, no. 6, pp. 3594–3601, May 2014.

[200]   M. Tosun, S. Chuang, H. Fang, A. B. Sachid, M. Hettick, Y. Lin, Y. Zeng, and A. Javey, "High-Gain Inverters Based on WSe2 Complementary Field-Effect Transistors," ACS Nano, vol. 8, no. 5, pp. 4948–4953, Mar. 2014.

[201]   B. Chamlagain, Q. Li, N. J. Ghimire, H.-J. Chuang, M. M. Perera, H. Tu, Y. Xu, M. Pan, D. Xaio, J. Yan, D. Mandrus, and Z. Zhou, "Mobility Improvement and Temperature Dependence in MoSe2 Field-Effect Transistors on Parylene-C Substrate," ACS Nano, vol. 8, no. 5, pp. 5079–5088, Apr. 2014.

[202]   J. L. Verble and T. J. Wieting, "Lattice Mode Degeneracy in MoS2 and Other Layer Compounds," Phys. Rev. Lett., vol. 25, no. 6, pp. 362–365, Aug. 1970.

[203]   Y. Zhao, X. Luo, H. Li, J. Zhang, P. T. Araujo, C. K. Gan, J. Wu, H. Zhang, S. Y. Quek, M. S. Dresselhaus, and Q. Xiong, "Interlayer Breathing and Shear Modes in Few-Trilayer MoS2 and WSe2," Nano Lett., vol. 13, no. 3, pp. 1007–1015, Feb. 2013.

[204]   H. Zeng, B. Zhu, K. Liu, J. Fan, X. Cui, and Q. M. Zhang, "Low-frequency Raman modes and electronic excitations in atomically thin MoS2 films," Phys. Rev. B, vol. 86, no. 24, p. 241301, Dec. 2012.

[205]   A. Molina-Sánchez and L. Wirtz, "Phonons in single-layer and few-layer MoS2 and WS2," Phys. Rev. B, vol. 84, no. 15, p. 155413, Oct. 2011.

[206]   C. Lee, H. Yan, L. E. Brus, T. F. Heinz, J. Hone, and S. Ryu, "Anomalous Lattice Vibrations of Single- and Few-Layer MoS2," ACS Nano, vol. 4, no. 5, pp. 2695–2700, Apr. 2010.

[207]   H. Li, Q. Zhang, C. C. R. Yap, B. K. Tay, T. H. T. Edwin, A. Olivier, and D. Baillargeat, "From Bulk to Monolayer MoS2: Evolution of Raman Scattering," Advanced Functional Materials, vol. 22, no. 7, pp. 1385–1390, 2012.

[208]   W. Zhao, Z. Ghorannevis, K. K. Amara, J. R. Pang, M. Toh, X. Zhang, C. Kloc, P. H. Tan, and G. Eda, "Lattice dynamics in mono- and few-layer sheets of WS2 and WSe2," Nanoscale, vol. 5, no. 20, pp. 9677–9683, 2013.

[209]   P. Tonndorf, R. Schmidt, P. Böttger, X. Zhang, J. Börner, A. Liebig, M. Albrecht, C. Kloc, O. Gordan, D. R. T. Zahn, S. M. de Vasconcellos, and R. Bratschitsch,

"Photoluminescence emission and Raman response of monolayer MoS2, MoSe2, and WSe2," Opt. Express, vol. 21, no. 4, pp. 4908–4916, Feb. 2013.

[210] Constantin Carabatos-Nédelec and DavidC Smith, "Raman Spectroscopy Applied to Crystals," in Handbook of Raman Spectroscopy, 0 vols., CRC Press, 2001.

[211] A. Berkdemir, H. R. Gutierrez, A. R. Botello-Mendez, N. Perea-Lopez, A. L. Elias, C.-I. Chia, B. Wang, V. H. Crespi, F. Lopez-Urias, J.-C. Charlier, H. Terrones, and M. Terrones, "Identification of individual and few layers of WS2 using Raman Spectroscopy," Sci. Rep., vol. 3, Apr. 2013.

[212] S. Larentis, B. Fallahazad, and E. Tutuc, "Field-effect transistors and intrinsic mobility in ultra-thin MoSe2 layers," Applied Physics Letters, vol. 101, no. 22, p. -, 2012.

[213] M. Zhang, J. Wu, Y. Zhu, D. O. Dumcenco, J. Hong, N. Mao, S. Deng, Y. Chen, Y. Yang, C. Jin, S. H. Chaki, Y.-S. Huang, J. Zhang, and L. Xie, "Two-Dimensional Molybdenum Tungsten Diselenide Alloys: Photoluminescence, Raman Scattering, and Electrical Transport," ACS Nano, vol. 8, no. 7, pp. 7130–7137, Jun. 2014.

[214] X. Luo, Y. Zhao, J. Zhang, M. Toh, C. Kloc, Q. Xiong, and S. Y. Quek, "Effects of lower symmetry and dimensionality on Raman spectra in two-dimensional WSe2," Phys. Rev. B, vol. 88, no. 19, p. 195313, Nov. 2013.

[215] H. R. Gutiérrez, N. Perea-López, A. L. Elías, A. Berkdemir, B. Wang, R. Lv, F. López-Urías, V. H. Crespi, H. Terrones, and M. Terrones, "Extraordinary Room-Temperature Photoluminescence in Triangular WS2 Monolayers," Nano Lett., vol. 13, no. 8, pp. 3447–3454, Nov. 2012.

[216] W. Zhao, Z. Ghorannevis, L. Chu, M. Toh, C. Kloc, P.-H. Tan, and G. Eda, "Evolution of Electronic Structure in Atomically Thin Sheets of WS2 and WSe2," ACS Nano, vol. 7, no. 1, pp. 791–797, Dec. 2012.

[217] D. Y. Qiu, F. H. da Jornada, and S. G. Louie, "Optical Spectrum of MoS2: Many-Body Effects and Diversity of Exciton States," Phys. Rev. Lett., vol. 111, no. 21, p. 216805, Nov. 2013.

[218] A. Pachoud and M. Jaiswal and P. K. Ang and K. P. Loh and B. Özyilmaz, "Graphene transport at high carrier densities using a polymer electrolyte gate," EPL (Europhysics Letters), vol. 92, no. 2, p. 27001, 2010.

[219] A. Sagar, K. Balasubramanian, M. Burghard, K. Kern, and R. Sordan, "Polymer-electrolyte gated graphene transistors for analog and digital phase detection," Applied Physics Letters, vol. 99, no. 4, p. -, 2011.

[220] Y. Ohno, K. Maehashi, Y. Yamashiro, and K. Matsumoto, "Electrolyte-Gated Graphene Field-Effect Transistors for Detecting pH and Protein Adsorption," Nano Lett., vol. 9, no. 9, pp. 3318–3322, Jul. 2009.

[221] DasA., PisanaS., ChakrabortyB., PiscanecS., SahaS. K., WaghmareU. V., NovoselovK. S., KrishnamurthyH. R., GeimA. K., FerrariA. C., and SoodA. K., "Monitoring dopants by Raman scattering in an electrochemically top-gated graphene transistor," Nat Nano, vol. 3, no. 4, pp. 210–215, Apr. 2008.

[222] K. F. Mak, C. H. Lui, J. Shan, and T. F. Heinz, "Observation of an Electric-Field-Induced Band Gap in Bilayer Graphene by Infrared Spectroscopy," Phys. Rev. Lett., vol. 102, no. 25, p. 256405, Jun. 2009.

[223] D. K. Efetov and P. Kim, "Controlling Electron-Phonon Interactions in Graphene at Ultrahigh Carrier Densities," Phys. Rev. Lett., vol. 105, no. 25, p. 256805, Dec. 2010.

[224] M. J. Panzer and C. D. Frisbie, "Polymer Electrolyte-Gated Organic Field-Effect Transistors: Low-Voltage, High-Current Switches for Organic Electronics and Testbeds for Probing Electrical Transport at High Charge Carrier Density," J. Am. Chem. Soc., vol. 129, no. 20, pp. 6599–6607, May 2007.

[225] B. Chakraborty, A. Bera, D. V. S. Muthu, S. Bhowmick, U. V. Waghmare, and A. K. Sood, "Symmetry-dependent phonon renormalization in monolayer MoS2 transistor," Phys. Rev. B, vol. 85, no. 16, p. 161403, Apr. 2012.

[226] S. Mouri, Y. Miyauchi, and K. Matsuda, "Tunable Photoluminescence of Monolayer MoS2 via Chemical Doping," Nano Lett., vol. 13, no. 12, pp. 5944–5948, Nov. 2013.

[227] V. Perebeinos, J. Tersoff, and P. Avouris, "Scaling of Excitons in Carbon Nanotubes," Phys. Rev. Lett., vol. 92, no. 25, p. 257402, Jun. 2004.

[228] A. G. Walsh, A. Nickolas Vamivakas, Y. Yin, S. B. Cronin, M. Selim Ünlü, B. B. Goldberg, and A. K. Swan, "Scaling of exciton binding energy with external dielectric function in carbon nanotubes," Physica E: Low-dimensional Systems and Nanostructures, vol. 40, no. 7, pp. 2375–2379, May 2008.

[229] M. Kumagai and T. Takagahara, "Excitonic and nonlinear-optical properties of dielectric quantum-well structures," Phys. Rev. B, vol. 40, no. 18, pp. 12359–12381, Dec. 1989.

[230] L. V. Kulik, V. D. Kulakovskii, M. Bayer, A. Forchel, N. A. Gippius, and S. G. Tikhodeev, "Dielectric enhancement of excitons in near-surface quantum wells," Phys. Rev. B, vol. 54, no. 4, pp. R2335–R2338, Jul. 1996.

[231] A. K. M. Newaz, Y. S. Puzyrev, B. Wang, S. T. Pantelides, and K. I. Bolotin, "Probing charge scattering mechanisms in suspended graphene by varying its dielectric environment," Nat Commun, vol. 3, p. 734, Mar. 2012.

[232] F. Chen, J. Xia, D. K. Ferry, and N. Tao, "Dielectric Screening Enhanced Performance in Graphene FET," Nano Lett., vol. 9, no. 7, pp. 2571–2574, Jun. 2009.

[233] B. Radisavljevic and A. Kis, "Mobility engineering and a metal–insulator transition in monolayer MoS2," Nat Mater, vol. 12, no. 9, pp. 815–820, Sep. 2013.

[234] S.-L. Li, K. Wakabayashi, Y. Xu, S. Nakaharai, K. Komatsu, W.-W. Li, Y.-F. Lin, A. Aparecido-Ferreira, and K. Tsukagoshi, "Thickness-Dependent Interfacial Coulomb Scattering in Atomically Thin Field-Effect Transistors," Nano Lett., vol. 13, no. 8, pp. 3546–3552, Jul. 2013.

[235] N. Ma and D. Jena, "Charge Scattering and Mobility in Atomically Thin Semiconductors," Phys. Rev. X, vol. 4, no. 1, p. 011043, Mar. 2014.

[236] N. Mao, Y. Chen, D. Liu, J. Zhang, and L. Xie, "Solvatochromic Effect on the Photoluminescence of MoS2 Monolayers," Small, vol. 9, no. 8, pp. 1312–1315, 2013.

[237] R. Yan, S. Bertolazzi, J. Brivio, T. Fang, A. Konar, A. G. Birdwell, N. V. Nguyen, A. Kis, D. Jena, and H. G. Xing, "Raman and photoluminescence study of dielectric and thermal effects on atomically thin MoS2," arXiv:1211.4136 [cond-mat.mtrl-sci], Nov. 2012.

[238] M. Buscema, G. Steele, H. J. van der Zant, and A. Castellanos-Gomez, "The effect of the substrate on the Raman and photoluminescence emission of single-layer MoS2," Nano Research, vol. 7, no. 4, pp. 1–11, 2014.

[239] D. Sercombe, S. Schwarz, O. D. Pozo-Zamudio, F. Liu, B. J. Robinson, E. A. Chekhovich, I. I. Tartakovskii, O. Kolosov, and A. I. Tartakovskii, "Optical investigation

of the natural electron doping in thin MoS2 films deposited on dielectric substrates," Sci. Rep., vol. 3, Dec. 2013.

[240]   N. Scheuschner, O. Ochedowski, A.-M. Kaulitz, R. Gillen, M. Schleberger, and J. Maultzsch, "Photoluminescence of freestanding single- and few-layer MoS2," Phys. Rev. B, vol. 89, no. 12, p. 125406, Mar. 2014.

[241]   G. Plechinger, F.-X. Schrettenbrunner, J. Eroms, D. Weiss, C. Schüller, and T. Korn, "Low-temperature photoluminescence of oxide-covered single-layer MoS2," physica status solidi (RRL) – Rapid Research Letters, vol. 6, no. 3, pp. 126–128, 2012.

[242]   M. Baldo and V. Stojanovic, "Optical switching: Excitonic interconnects," Nat Photon, vol. 3, no. 10, pp. 558–560, Oct. 2009.

[243]   http://www.hbcpnetbase.com/

[244]   H. Shi, R. Yan, S. Bertolazzi, J. Brivio, B. Gao, A. Kis, D. Jena, H. G. Xing, and L. Huang, "Exciton Dynamics in Suspended Monolayer and Few-Layer MoS2 2D Crystals," ACS Nano, vol. 7, no. 2, pp. 1072–1080, Dec. 2012.

[245]   C. Rice, R. J. Young, R. Zan, U. Bangert, D. Wolverson, T. Georgiou, R. Jalil, and K. S. Novoselov, "Raman-scattering measurements and first-principles calculations of strain-induced phonon shifts in monolayer MoS2," Phys. Rev. B, vol. 87, no. 8, p. 081307, Feb. 2013.

[246]   S. Tongay, J. Suh, C. Ataca, W. Fan, A. Luce, J. S. Kang, J. Liu, C. Ko, R. Raghunathanan, J. Zhou, F. Ogletree, J. Li, J. C. Grossman, and J. Wu, "Defects activated photoluminescence in two-dimensional semiconductors: interplay between bound, charged, and free excitons," Sci. Rep., vol. 3, Sep. 2013.

[247]   S.-L. Li, H. Miyazaki, H. Song, H. Kuramochi, S. Nakaharai, and K. Tsukagoshi, "Quantitative Raman Spectrum and Reliable Thickness Identification for Atomic Layers on Insulating Substrates," ACS Nano, vol. 6, no. 8, pp. 7381–7388, Jul. 2012.